

1 Visibility-derived aerosol optical depth over global land from 1980 2 1959 to 2021

3 Hongfei Hao¹, Kaicun Wang², Chuanfeng Zhao³, Guocan Wu¹, Jing Li³

4 ¹Global Change and Earth System Science, Faculty of Geographical Science, Beijing Normal
5 University, Beijing 100875, China

6 ²Institute of Carbon Neutrality, Sino French Institute of Earth System Science, College Urban and
7 Environmental Sciences, Peking University, Beijing 100871, China

8 ³Institute of Carbon Neutrality, Department of Atmospheric and Oceanic Sciences, School of
9 Physics, College Urban and Environmental Sciences, Peking University, Beijing 100871, China

10 *Corresponding Author: Kaicun Wang (kcwang@pku.edu.cn)*

11 Abstract

12 Long-term and high spatial resolution aerosol optical depth (AOD) data are essential for climate
13 change detection and attribution. Global ground-based AOD observations are sparsely distributed,
14 and satellite AOD retrievals have a low temporal frequency, as well low accuracy before 2000 over
15 land. In this study, AOD at 550nm is derived from hourly-visibility observations collected at more
16 than 5000 meteorological stations over global land from 1980-1959 to 2021. The AOD retrievals
17 (550nm) of the Moderate Resolution Imaging Spectroradiometer (MODIS) onboard the Aqua Earth
18 observation satellite are used to train the machine learning model, and the ERA5 reanalysis
19 boundary layer height is used to convert the surface visibility to AOD. Comparisons with
20 independent datasets (AERONET ground-based observations) shows that the predicted AOD has a
21 correlation coefficients of 0.55 with AERONET ground observations at daily time-scale. The
22 correlation coefficients are higher at monthly and annual scales, which are 0.61 for the monthly and
23 0.65 for the annual, respectively. The evaluation result shows consistent predictive ability prior to
24 2000, with a correlation coefficient of 0.54, 0.66 and 0.66 at daily, monthly, and annual scales,
25 respectively. Due to a small number and sparse visibility stations prior to 1980, the global/regional
26 analysis in this study is from 1980 to 2021. From 1980 to 2021, ~~t~~The visibility-derived AOD at
27 station scale is gridded into a 0.5° grid by ordinary kriging interpolation. The mean visibility-
28 derived AOD over the global land (-60°N-85°N), the Northern Hemisphere, and the Southern
29 Hemisphere are 0.17761, 0.1758, and 0.1753, with a trend of -0.00296/10a, -0.00180030/10a, and -
30 0.00590021/10a from 1980 to 2021. For theThe regional scale, the-mean (trends) of AOD are 0.145
31 181 (-0.009641/10a), 0.139-163 (-0.00264/10a), 0.131-146 (-0.001709/10a), 0.153-165 (-
32 0.00274/10a), 0.1982 (-0.0100075/10a), 0.275-281 (-0.00080062/10a), 0.177-182 (-0.00196/10a),
33 0.13327 (-0.00840028/10a), 0.177-222 (-0.00073/10a), 0.222-244 (-0.00090/10a), 0.232-241
34 (0.01300-0071/10a), and 0.255-254 (0.00960119/10a) in Eastern Europe, Western Europe, Western
35 North America, Eastern North America, Central South America, Western Africa, Southern Africa,
36 Australia, Southeast Asia, Northeast Asia, Eastern China, and India, respectively. However, the
37 trends are decreasing significantly in Eastern China (-0.0572/10a) and Northeast Asia (-0.0213/10a)

38 ~~after 2014 and the lager increasing trend is found after 2005 in India (0.0446/10a).~~ The visibility-
39 derived ~~daily~~ AOD ~~dataset~~ at ~~5032~~ stations ~~and grid scales~~ over global land from ~~1980-1959~~ to 2021
40 are available at National Tibetan Plateau / Third Pole Environment Data Center
41 (<https://doi.org/10.11888/Atmos.tpdc.300822>) (Hao et al., 2023).

42 How to cite. Hao, H., Wang, K., C. Zhao, Wu, G., J. Li (2023). Visibility-derived aerosol optical
43 depth over global land (~~1980-1959~~-2021). National Tibetan Plateau / Third Pole Environment Data
44 Center. <https://doi.org/10.11888/Atmos.tpdc.300822>.

45 1 Introduction

46 Atmospheric aerosols are composed of solid and liquid particles suspended in the atmosphere.
47 Aerosol particles are directly emitted into the atmosphere or formed through gas-particle
48 transformation (Calvo et al., 2013), with diverse shapes and sizes (Fan et al., 2021), optical
49 properties, and components (Liao et al., 2015; Zhang et al., 2020; Li et al., 2022). Most atmospheric
50 aerosols are concentrated in the troposphere, especially in the boundary layer (Liu et al., 2022), with
51 a high concentration near emission sources (Kulmala et al., 2004) , and a small portion are
52 distributed in the stratosphere. Atmospheric aerosols severely impact the atmospheric environment
53 and human health. They deteriorate air quality, reduce visibility, and cause other environmental
54 issues (Wang et al., 2012; Boers et al., 2015). They impair human health or other organisms'
55 conditions by increasing cardiovascular and respiratory disease incidence and mortality rates (Chafe
56 et al., 2014; Yang et al., 2022). The Global Burden of Disease shows that global exposure to ambient
57 PM_{2.5} (particulate matter suspended in air with an aerodynamic diameter of less than 2.5
58 micrometers) resulted in 0.37 million deaths and 9.9 million disability-adjusted life years (Chafe et
59 al., 2014).

60 Aerosols are inextricably linked to climate change. Atmospheric aerosols alter the Earth's energy
61 budget and ~~then~~ affect the climate (Li et al., 2022). They cool the surface and heat the atmosphere
62 by scattering and absorbing solar radiation (Forster et al., 2007; Chen et al., 2022). Aerosols, such
63 as black carbon and brown carbon, also absorb solar radiation (Bergstrom et al., 2007), heat the
64 local atmosphere and suppress or invigorate convective activities (Ramanathan et al., 2001; Sun and
65 Zhao, 2020). Aerosols also alter the optical properties and life span of clouds (Albrecht, 1989).
66 Atmospheric aerosols strongly affect regional and global short-term and long-term climates through
67 direct and indirect effects (Meneill, 2017).

68 Tropospheric aerosols are considered as the second largest forcing factor for global climate change
69 (Li et al., 2022), and they reduce the warming due to greenhouse gases by -0.5°C (~~Ipcc~~IPCC, 2021).
70 However, aerosols are also regarded as the largest contributor to ~~quantifying the~~ uncertainty of
71 present-day climate change (~~Ipcc~~IPCC, 2021). The uncertainties are caused by the deficiencies of
72 the global descriptions of aerosol optical properties (such as scattering and absorption) and
73 microphysical properties (such as size and component), and the impact on cloud and precipitation,
74 further affecting the estimation of aerosol radiative forcing (Lee et al., 2016; Ipcc, 2021). Therefore,
75 sufficient aerosol observations are crucial. In aerosol measurements, aerosol optical depth (AOD)
76 is often used to describe its column properties, which represents the vertical integration of aerosol
77 extinction coefficients. AOD is an important physical quantity for estimating the content,
78 atmospheric pollution and climatology of aerosols (Zhang et al., 2020).

79 AOD data usually from ground-based and satellite-borne remote sensing observations. They have
80 both advantages and disadvantages. Ground-based lidar observation is an active remote sensing
81 technology. Lidar generally emits laser and receives backscattered signals to invert the extinction
82 coefficient of aerosols at different heights (Klett, 1985). By using the depolarization ratio, the type
83 of aerosol, such as fine particles or dust, can be distinguished (Bescond et al., 2013). The AOD
84 within a certain height can be calculated by integrating the extinction coefficients; however,
85 scattering signals are usually not received near the ground, leading to blind spots (Singh et al., 2019).
86 At present, there are many ground-based lidar worldwide and regional networks, which provides
87 important support of vertical changes in aerosols, such as the NASA Micro-Pulse Lidar Network
88 (MPLNET) in the early 1990s (Welton et al., 2002), the European Aerosol Research Lidar Network
89 (EARLINET) since 2000 (Bösenberg and Matthias, 2003), the Latin American Lidar Network
90 (LALINET) since 2013 (Guerrero-Rascado et al., 2016).

91 Ground-based remote sensing observations supply aerosol loading data (such as AOD), by
92 measuring the attenuation of radiation from the top of the atmosphere to the surface (Holben et al.,
93 1998). This type of observation mainly uses weather-resistant automatic sun and sky scanning
94 spectral radiometers to retrieve optical and microphysical aerosol properties (Che et al., 2014). The
95 Aerosol Robotic Network (AERONET) is a popular global network composed of NASA and
96 multiple international partners that provides high-quality and high-frequency aerosol optical and
97 microphysical properties under various geographical and environmental conditions (Holben et al.,
98 1998; Dubovik et al., 2000). The AERONET observations are extensively used to validate satellite
99 remote sensing observations and model simulations, as well as climatology study (Dubovik et al.,
100 2002b). There are many regional networks of sun photometers, such as the Maritime Aerosol
101 Network (MAN), which use a handheld sun photometer to collect data over the ocean and is merged
102 into AERONET (Smirnov et al., 2009), the China Aerosol Robot Sun Photometer Network
103 (CARSNET) (Che et al., 2009), the Canadian sub-network of AERONET (AEROCAN) (Bokoye et
104 al., 2001), Aerosol characterization via Sun photometry: Australian Network (AeroSpan)
105 (Mukkavilli et al., 2019), and the sky radiometer network (SKYNET) in Asia and Europe (Kim et
106 al., 2004; Nakajima et al., 2020). Another very valuable global network is the NOAA/ESRL
107 Federated Aerosol Network (FAN), which uses integrated nephelometers distinct from sun
108 photometers, mainly located in remote areas, providing background aerosol properties over 30 sites
109 (Andrews et al., 2019).

110 Satellite remote-sensing is a space-based method that can provide aerosol properties worldwide.
111 With the development of satellite remote sensing technology since 1970s, aerosol distributions can
112 be extracted with the advantage of sufficient real-time and global coverage from multiple satellite
113 sensors (Kaufman and Boucher, 2002; Anderson et al., 2005). The Advanced Very High Resolution
114 Radiometer (AVHRR) is the earliest sensor used for retrieving AOD over ocean (Nagaraja Rao et
115 al., 1989). The Moderate Resolution Imaging Spectroradiometer (MODIS), on board the Terra
116 (launched in 1999) and Aqua (launched in 2002) satellites is a popular sensor with 36 channels,
117 which have been used for AOD retrieval over both ocean and land based on the Dark Target and the
118 Deep Blue algorithms (Remer et al., 2005; Levy et al., 2013). The latest MODIS AOD data version
119 is the Collection 6.1, which provides global AOD over 20 years (Wei et al., 2019). There are also
120 many other satellite sensors that can be used to retrieve AOD, such as the Polarization and
121 Directionality of the Earth's Reflectances (POLDER) during 1996-1997, 2003 and 2004-2013

122 (Deuzé et al., 2000), Sea-viewing Wide Field-of-view Sensor (SeaWiFS) during 1997-2007
123 (O'reilly et al., 1998), the Multi-angle Imaging Spectroradiometer (MISR) on Terra since 1999
124 (Diner et al., 1998). The Cloud-Aerosol Lidar with Orthogonal Polarization (CALIOP) has also
125 derived aerosols in the vertical direction since 2006 (Winker et al., 2009).

126 These measurements provide important data for studying the global and regional spatiotemporal
127 variabilities and climate effect of aerosols. However, ground-based remote sensing observations
128 only provide aerosol properties with low spatial coverage. There were only about 150 ground
129 stations worldwide in 2002 and even fewer sites were available for climate analysis (Holben et al.,
130 1998; Chu et al., 2002), which limited aerosol climate research by spatial coverage (Bright and
131 Gueymard, 2019). Satellite remote sensing overcomes the limitations of spatial coverage. The
132 AVHRR has been used to retrieve AOD since 1980, but it is limited by a few channel number, low
133 spatial resolution, and insufficient validation through ground-based observations before 2000 (Hsu
134 et al., 2017). Many studies have only investigated the trends and distributions of aerosols after 2000
135 (Bösenberg and Matthias, 2003; Winker et al., 2013; Xia et al., 2016; Tian et al., 2023), because of
136 the lack of long-term and global cover AOD products, which is the bottleneck for aerosol climate
137 change detection and attributions.

138 To overcome these limitations and enrich aerosol data, alternative observation data could be utilized
139 to derive AOD. Atmospheric horizontal visibility is a suitable alternative (Wang et al., 2009; Zhang
140 et al., 2020), because it has the advantages of the long-term records with a large number of stations
141 worldwide.

142 Atmospheric visibility is a physical quantity that describes the transparency of the atmosphere
143 through manual and automatic observations, and the automatic observations of visibility usually
144 measure atmospheric extinction (scattering coefficient and transmissivity). Koschmieder (1924)
145 first proposed the relationship between the meteorological optical range and the total optical depth.
146 Elterman (1970) further established a formula between AOD and visibility by assuming an
147 exponential decrease in aerosol concentration with altitude, considering the extinction of molecules
148 and ozone to analyze air pollution, which called the Elterman model. Qiu and Lin (2001) corrected
149 the Elterman model by considering the influence of water vapor and used two water vapor pressure
150 correction coefficients to retrieve AOD of 16 stations in China in 1990. Wang et al. (2009) analyzed
151 the trend of AOD using visibility-based retrievals from 1973 to 2007 over land. Lin et al. (2014)
152 retrieved the AOD in eastern China in 2006 using visibility and aerosol vertical profiles provided
153 by GEOS-Chem. Wu et al. (2014) and Zhang et al. (2017) parameterized the constants in the
154 Elterman model and use satellite retrieved AOD to solve the parameters in the models at different
155 stations, to retrieve the long-term AOD in China.

156 Zhang et al. (2020) reviewed the methods of visibility retrieval of AOD, indicating that visibility-
157 based retrieval of AOD can compensate for the shortcomings of long-term aerosol observation data.
158 Simultaneously, various parameters, such as station altitude, consistency of visibility data, water
159 vapor and aerosol vertical profiles (scale height), were discussed with modified suggestions
160 proposed. These studies have enriched AOD data regionally. These studies have enriched aerosol
161 data in some extent. At present, there are very few studies on global visibility-retrieved AOD and to
162 analyze climatology of aerosols.

163 The two physical quantities of visibility and AOD have both connections and differences, making it

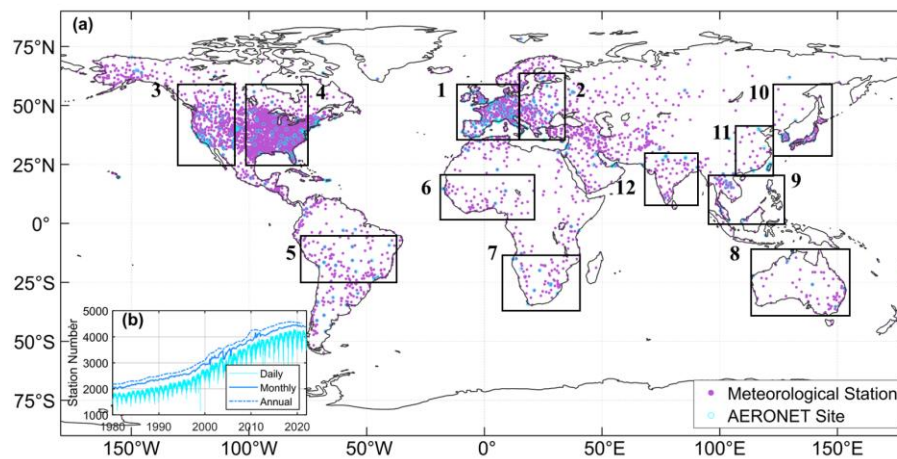
164 challenging to retrieve AOD from visibility. Visibility represents the maximum horizontal visible
165 distance near the surface, while AOD represents the total vertical attenuation of solar radiation by
166 aerosols. The visibility of automatic observation is dependent on the local horizontal atmospheric
167 extinction (Noaa et al., 1998). Visibility has not a simple linear relationship with meteorological
168 factors. The vertical structure of aerosols is the greatest challenge to obtain, as it is not a simple
169 hypothetical curve in complex terrain and circulation conditions (Zhang et al., 2020). These
170 limitations make it more complex to derive AOD. Machine learning methods can effectively address
171 complex nonlinear relationships between variables and have been widely applied in remote sensing
172 and climate research fields. Li et al. (2021) used the random forest method to predict PM_{2.5} in Iraq
173 and Kuwait based on satellite AOD during 2001-2018. Kang et al. (2022) applied LightGBM and
174 random forest to estimate AOD over East Asia, and the results showed a consistency with
175 AERONET. Dong et al. (2023) derived aerosol single scattering albedo from visibility and satellite
176 AOD over 1000 global stations. Hu et al. (2019) used a deep learning method to retrieve horizontal
177 visibility from MODIS AOD. These studies have confirmed the ability of machine learning to
178 effectively solve complex relationships among variables. ~~And p~~Previous studies are mostly
179 conducted at the regional or national scale, and few studies at the global scale. Thus, it is feasible to
180 derive AOD from atmospheric visibility over global land by using the machine learning method.

181 In this study, we propose a machine learning method to derive AOD, where satellite AOD is the
182 target value, and visibility and other related meteorological variables are the predictors. We explain
183 the ~~model's robustness of the model, and evaluate the model's predictive ability, and~~ validate the
184 model's predictions using independent ground-based AOD, satellite retrievals and reanalysis AOD,
185 and analyze the mean and trend of AOD across land and regions. ~~Two A station-scale~~ datasets of
186 long-term ~~high-resolution~~AOD ~~are is~~ generated. The Section 2 introduces the data and method. The
187 Section 3 is the evaluation and validation of the visibility-derived AOD, and the distribution and
188 trends are discussed at global and regional scales. The Section 5 presents the conclusions. This study
189 is dedicated to supporting the research of aerosols in climate change detection and attribution.

190 **2 Data and method**

191 **2.1 Study area**

192 The study area is global land. A total of 5032 meteorological stations and 395 AERONET sites are
193 selected in this study, shown in Figure 1. Twelve regions are selected for special analysis, including
194 Eastern Europe, Western Europe, Western North America, Eastern North America, Central South
195 America, Western Africa, Southern Africa, Australia, Southeast Asia, Northeast Asia, Eastern China,
196 and India ~~and the station number is 187, 494, 390, 1759, 132, 72, 78, 86, 76, 140, 26, and 51,~~
197 ~~respectively. The meteorological observations data including visibility are available since 1959.~~ The
198 time range of ~~global and regional average analysis~~the study is from 1980 to 2021, during which the
199 ~~visibility observations records of meteorological stations~~are sufficient with a uniform spatial
200 distribution. As shown in Figure 1, the daily ~~visibility~~ records have exceeded 11500 stations, and
201 monthly and annual records have exceeded 2000 during 1980-1990. After 2000, monthly records
202 have reached 3000, ~~which is the foundation of gridding AOD.~~



203

204 **Figure 1:** Study area (a) and the meteorological station number (b) ~~with-at~~ daily, monthly, and
 205 annual ~~records~~ scale. The number of meteorological stations (filled circles) is 5032. The number of
 206 AERONET sites (empty circles) is 395. The box regions of labelled with number 1-12 are Eastern
 207 Europe, Western Europe, Western North America, Eastern North America, Central South America,
 208 Western Africa, Southern Africa, Australia, Southeast Asia, Northeast Asia, Eastern China, and India.

209 **2.2 Meteorological data**

210 The ~~ground~~-hourly ground-based meteorological data from ~~1980-1959~~ to 2021 is collected from
 211 5032 ~~automated~~-meteorological stations of airports over land, which can be downloaded at
 212 <https://mesonet.agron.iastate.edu/ASOS>. Over 1000 stations belong to the Automated Surface
 213 Observing System (ASOS), and others are sourced from airport reports around the world. The
 214 visibility measurements can be divided into automatic observation and manual observation.
 215 Automatic Automated-surface-visibility observations reduce errors associated with human
 216 involvement in data collection, processing, and transmission. ~~The data can be downloaded at~~
 217 ~~<https://mesonet.agron.iastate.edu/ASOS>~~. ~~The visibility and other meteorological data is-are~~
 218 extracted from the Meteorological Terminal Aviation Routine Weather Report (METAR). The World
 219 Meteorological Organization (WMO) sets guidelines for METAR reports, including report format,
 220 encoding, observation instruments and methods ~~used~~, data accuracy, and consistency. ~~These~~
 221 ~~requirements, which~~ ensures the consistency and comparability of METAR reports globally. Some
 222 international regulations can be referenced at [https://community.wmo.int/en/implementation-areas-](https://community.wmo.int/en/implementation-areas-aeronautical-meteorology-programme)
 223 [aeronautical-meteorology-programme](https://community.wmo.int/en/implementation-areas-aeronautical-meteorology-programme). ~~Among them, over 1,000 stations belong to the Automated~~
 224 ~~Surface Observing System (ASOS), and others are sourced from airport reports around the world.~~

225 The daily average visibility is calculated using harmonic mean in equation (1). The reciprocal of
 226 visibility is proportional to the extinction coefficient (Wang et al., 2009). Experiments have found
 227 that harmonic average visibility can better detect the weather phenomena than arithmetic average
 228 visibility, when visibility decline quickly (Noaa et al., 1998). ~~The visibility is calculated using the~~
 229 ~~extinction coefficient, which is directly proportional to the reciprocal of visibility (Wang et al., 2009).~~
 230 Harmonious average visibility can capture the process of visibility decline more quickly. Therefore,
 231 daily visibility will have greater representativeness. \therefore

232
$$V = n / \left(\frac{1}{V_1} + \frac{1}{V_2} + \dots + \frac{1}{V_n} \right), \quad (1)$$

233 ~~where V is the harmonic mean visibility, n = 24 for the daily visibility, and V_1, V_2, \dots, V_n are the~~
 234 ~~individual hourly visibility.~~

235 In addition to hourly visibility (VIS), other variables closely related to aerosol properties are selected,
 236 including relative humidity (RH), dew point temperature (DT), temperature (TMP), wind speed
 237 (WS) and sea-level pressure (SLP). ~~Because air t~~Temperature affects atmospheric stability and the
 238 rate of secondary particle formation, and humidity influences the size and hygroscopic growth, and
 239 wind speed and pressure significantly impact the transport and deposition. Sky conditions (cloud
 240 amount) and hourly precipitation are also selected to remove the records of extensive cloud cover
 241 and precipitation.

242 We processed the meteorological data as follows. The records with high missing value ratio are
 243 eliminated (Husar et al., 2000). When over 80% overcast or fog, the records of sky conditions are
 244 eliminated, though such situations occur less than 1% of the time over land (Remer et al., 2008).
 245 The records with 1-hour precipitation greater than 0.1 mm are eliminated. We calculate the
 246 temperature dew point difference (dT). The low visibility records under “blowing snow” weather
 247 are eliminated at high latitude region (> 65°N), when wind speed is great than 4.5m/s (Husar et al.,
 248 2000). When the RH is greater than 90%, it is impossible to distinguish whether it is fog or haze, or
 249 both, and even precipitation. ~~Therefore, t~~The records with RH greater than or equal to 90% are
 250 eliminated. When the RH is less than 30%, the hygroscopic dilution-effect of aerosols is very low
 251 or even negligible. When RH is between 30% and 90%, the hygroscopic effect of aerosols is high,
 252 and visibility is converted to dry visibility (Yang et al., 2021c), as shown in equation (2). ~~At least 3~~
 253 ~~hourly records of meteorological variables are required when calculating the daily average (n>=3).~~

254
$$V = n / \left(\frac{1}{V_1} + \frac{1}{V_2} + \dots + \frac{1}{V_n} \right), \quad (1)$$

255 ~~where V is the harmonic mean visibility, n is the daily record number, and V_1, V_2, \dots, V_n are the~~
 256 ~~individual hourly visibility.~~

257
$$VISD = VIS / (0.26 + 0.4285 * \log(100 - RH)), \quad (2)$$

258 where VISD is the dry visibility.

259 ~~Daily average of variables is calculated by at least 3 hourly records.~~

260 **2.3 Boundary layer height-**

261 The hourly boundary layer height (BLH) data from 1980 to 2021 ~~is-are~~ available from the Fifth
 262 Generation reanalysis of the European Medium-Range Weather Forecast Center (ERA5) with a
 263 resolution of 0.25° x 0.25° (<https://cds.climate.copernicus.eu>), which is the successor of ERA-
 264 Interim and has undergone various improvements (Hersbach et al., 2020). The atmospheric
 265 boundary layer is the layer closest to the Earth’s surface and exhibits complex turbulence activities,
 266 and its height undergoes significant diurnal variation. The ~~effects-of-the~~boundary layer play a
 267 crucial role in regulating and adjusting the distribution of atmospheric aerosols, such as on aerosols
 268 ~~are mainly manifested in~~-vertical distribution, concentration changes, transport, and deposition

(Ackerman et al., 1995). ~~The characteristics and variations in the boundary layer play a crucial role in regulating and adjusting the distribution of atmospheric aerosols.~~ The boundary layer height serves as an approximate measure of the scale height for aerosols (Zhang et al., 2020).

Compared ~~to~~ to observations of 300 stations over world from 2012 to 2019, the ERA5 BLH ~~of ERA5 was is~~ underestimated by 131.96m, ~~and Compared with the underestimated MERRA-2 (166.35m), JRA-55 (351.49m), and NECP-2 (420.86m), the BLH of ERA5 was is~~ closest to the observations compared to JRA-55, and NECP-2 BLH (Guo et al., 2021). The hourly BLH ~~hourly~~ data is temporally and spatially matched with visibility and the other meteorological data before calculating the daily average.

Because the reciprocal inverse of visibility is proportional to the extinction coefficient and positively related to AOD (Wang et al., 2009), we calculated ~~the~~ the reciprocal of visibility (VISI) and the reciprocal of dry visibility (VISDI). Due to the influence of boundary layer height on the vertical distribution of particles (Zhang et al., 2020), we calculated ~~the~~ the product (VISDIB) of ~~the reciprocal of dry visibility~~ VISDI and BLH. Therefore, the Predictor (Figure 2) is composed of 11 variables (TMP, Td, dT, RH, SLP, WS, VIS, BLH, VISI, VISDI, and VISDIB).

2.4 MODIS AOD products

Satellite daily AOD is available from the Moderate Resolution Imaging Spectroradiometer (MODIS) Level 3 Collection 6.1 AOD products of the Aqua (MYD09CMA) satellite from 2002 to 2021 and Terra (MOD09CMA) satellite from 2000 to 2021 with a spatial resolution of $0.05^\circ \times 0.05^\circ$ at a wavelength of 550 nm (<https://ladsweb.modaps.eosdis.nasa.gov>). ~~MOD/MYD09 has a higher spatial resolution than MOD/MYD08 ($1^\circ \times 1^\circ$), which may result in a greater difference in AOD values and reduce the proximity ratio to match the visibility derived AOD at station scale.~~ Terra (passing ~~approximately~~ 10:30 am at local time) and Aqua (passing ~~approximately~~ 1:30 pm at local time) ~~were are~~ successfully launched in December 1999 and May 2002, respectively.

MODIS, carried on the Terra and Aqua satellites is a crucial instrument in the NASA Earth Observing System program, which is designed to observe global biophysical processes (Salomonson et al., 1987). The 2,330 km-wide swath of the orbit scan can cover the entire globe every one to two days. MODIS has 36 channels and more spectral channels than previous satellite sensors (such as AVHRR). The ~~spectrumspectral~~ spectral ~~ranges~~ from 0.41 to $15\mu\text{m}$ representing three spatial resolutions: 250 m (2 channels), 500 m (5 channels), and 1 km (29 channels). The aerosol retrievals ~~algorithms~~ use seven of these channels ($0.47\text{--}2.13\mu\text{m}$) to retrieve aerosol characteristics and uses additional wavelengths in other parts of the spectrum to identify clouds and river sediments. Therefore, it has the ability to characterize the spatial and temporal characteristics of the global aerosol field.

The MODIS aerosol product actually ~~takes uses of~~ different algorithms ~~for to deriving retrieve~~ aerosols over land and ocean. The Dark Target (DT) algorithm is applied to densely vegetated areas because the surface reflectance over dark-target areas ~~was is~~ lower in the visible channels and ~~had~~ has nearly fixed ratios with the surface reflectance in the shortwave and infrared channels (Levy et al., 2007; Levy et al., 2013). The Deep Blue (DB) algorithm ~~was is~~ originally applied to bright land surfaces (such as deserts), and later extended to cover all cloud-free and snow-free land surfaces (Hsu et al., 2006; Hsu et al., 2013). MODIS Collection 6.1 aerosol product ~~was is~~ released in 2017, incorporating significant improvements in radiometric calibration and aerosol retrieval algorithms.

The aerosol retrievals usually are evaluated by ~~T~~the expected error. For the DT algorithm, the

312 ~~expected error is $\pm(0.05 \pm 15\% \text{AOD}_{\text{AERONET}})$.~~ The coverage of retrieval products varies by
 313 season based on the DT algorithm retrievals over land. Higher spatial coverage is observed in
 314 August and September, reaching 86-88%. During December and January, due to the presence of
 315 permanent ice and snow cover in high-latitude regions of the Northern Hemisphere, the spatial
 316 coverage is 78-80%. Thus, challenges remain in retrieving AOD values in high-latitude regions (Wei
 317 et al., 2019). However, visibility observations are available in high-latitude regions, thereby partially
 318 addressing the lack in these regions. In this study, the Terra and Aqua MODIS AOD are temporally
 319 and spatially matched with the meteorological stations. Aqua MODIS AOD is used as the Target,
 320 when training the model, and Terra MODIS AOD is used in the evaluation and validation of the
 321 model results, as shown in the flowchart (Figure 2).

322 2.5 Ground-based AOD

323 Ground-based 15-minute AOD data observations are available from the Aerosol Robotic Network
 324 (AERONET) Version 3.0 Level 2.0 product at 395 sites (Figure 1), which can be downloaded from
 325 <https://aeronet.gsfc.nasa.gov>. The AERONET program is a federation of ground-based remote
 326 sensing aerosol networks established by NASA and PHOTONS, including many subnetworks (such
 327 as AeroSpan, AEROCAN, NEON, and CARSNET). The sun photometer (CE-318) measures
 328 spectral sun and sky irradiance in the 340-1020 nm spectral range. ~~When the aerosol loading is low,~~
 329 ~~the error is significant.~~ AERONET has three levels of AOD products: Level 1.0 (unscreened), Level
 330 1.5 (cloud screened), and Level 2.0 (cloud screened and quality assured). Compared to Version 2,
 331 the Version 3 Level 2.0 database has undergone further cloud screening and quality assurance, which
 332 is generated based on Level 1.5 data with pre- and post-calibration and temperature adjustment and
 333 is recommended for formal scientific research (Giles et al., 2019). AERONET provides AOD
 334 products at wavelengths of 440, 675, 870, and 1020 nm. When the aerosol loading is low, the error
 335 is significant. When the AOD at 440 nm wavelength is less than 0.2, the error is 0.01, which is
 336 equivalent to the error of the absorption band in the total optical depth (Dubovik et al., 2002a). The
 337 total uncertainty in AOD under cloud-free conditions is less than ± 0.01 , ~~for when the~~ wavelength is
 338 more than 440 nm, and ± 0.02 for when the wavelength is less than 440 nm (Holben et al., 1998).
 339 AERONET AOD is usually considered as the 'true' value. The AOD at 440nm and the Ångström
 340 index at 440-675nm are used ~~for to calculate~~ AOD at 550 nm (not provided by AERONET), as
 341 shown in equation Eq. (3).

$$342 \tau_{550} = \tau_{440} \left(\frac{550}{440}\right)^{-\alpha}, \quad (3)$$

343 where τ_{440} and τ_{550} are the AOD at a wavelength of 440nm and 550 nm, and α is the Ångström
 344 index.

345 AERONET AOD, as the 'true' value, is the daily average AOD requires at least two observations
 346 at least two times within 1 hour (± 30 minutes) of Aqua/Terra transit time (Wei et al., 2019). ~~The~~
 347 matching conditions between AERONET sites and meteorological stations are (1) a distance of less
 348 than 0.5° , and (2) at least three years of observations. Finally, a total of 395 ~~pairs sites were are~~
 349 selected matched.

350 2.6 AOD reanalysis dataset

351 The monthly AOD (550nm) dataset of Modern-Era Retrospective Analysis for Research and

352 Applications version 2 (MERRA-2) from 1980 to 2021 is a NASA reanalysis of the modern satellite
353 era produced by NASA's Global Modeling and Assimilation Office with a spatial resolution of
354 $0.5 \times 0.625^\circ$ (Gelaro et al., 2017), available at <https://disc.gsfc.nasa.gov>. MERRA-2 AOD uses an
355 analysis splitting technique to assimilate AOD data at 550 nm. The assimilated AOD observations
356 are including (1) ~~—~~AOD retrievals from AVHRR (1979-2002) over global ocean, (2) AOD
357 retrievals from MODIS on Terra (2000–present) and Aqua (2002–present) over global land and
358 ocean, (3) AOD retrievals from MISR (2000–2014) over bright and desert surfaces, and (4) direct
359 AOD measurements from the ground-based AERONET (1999–2014) (Gelaro et al., 2017). The
360 monthly MERRA-2 AOD is used to evaluate the model's predictive ability before 2000 and after
361 2000.

362 **2.7 Decision tree regression**

363 **2.7.1 Feature selection**

364 Although a multidimensional dataset can provide as much potential information as possible for
365 AOD, irrelevant and redundant variables can also introduce significant noise in the model and
366 reduce the model's accuracy and stability (Kang et al., 2021; Dong et al., 2023). Therefore, the F-
367 test is used to search for the optimal feature subset in the Predictor, aiming to eliminate irrelevant
368 or redundant features and select truly relevant features, which helps to simplify the model's input
369 and improve the model's prediction ability (Dhanya et al., 2020). The F-test is a statistical test that
370 gives an f-score $(=-\log(p))$, p represents the degree to which the null hypothesis is not rejected) by
371 calculating the ratio of variances. In this study, we calculate the ratio of variance between the
372 Predictors and Target, and the features are ranked based on ~~higher values of~~ the f-score values. A
373 ~~greater-larger~~ value of f-score means that the distances between Predictors and Target are less and the
374 relationship is closer, thus, the feature is more important. We set $p=0.05$. When the score is less than
375 $-\log(0.05)$, the variable in the Predictors is not considered.

376 **2.7.2 Data balance**

377 When ~~the weather#~~ is clear, the AOD value is small (AOD<0.5), and the variability of AOD is small
378 (~~AOD<0.5~~), and the data is concentrated near the mean value. When heavy pollution, the AOD value is
379 large (AOD>0.5). Compared to clear sky, the AOD sequence will show "abnormal" large values with
380 low frequency, which is a phenomenon of the imbalance ~~of~~ AOD data. When dealing with imbalanced
381 datasets, because of the tendency of machine learning algorithms to perform better on the majority class
382 and overlook the minority class, the model ~~can~~ may be underfit (Chuang and Huang, 2023). Data
383 augmentation techniques are commonly employed to address the issue in imbalance data, which applies
384 a series of transformations or expansions to generate new training data, thereby increasing the diversity
385 and quantity of the training data of the minority class.

386 The Adaptive Synthetic Sampling (ADASYN) is a data augmentation technique specifically designed to
387 address data imbalance problem (He et al., 2008; Mitra et al., 2023). It is an extension of the Synthetic
388 Minority Over-sampling Technique (SMOTE) algorithm (Fernández et al., 2018). The goal of ADASYN
389 is to generate synthetic sample data for the minority class to increase its representation in the dataset.
390 ADASYN, which adaptively adjusts the generation ratio of synthetic samples based on the density
391 distribution of sample data, improves the dataset balance and enhances the performance of machine
392 learning models in dealing with imbalanced data.

393 The processing of imbalanced data includes (1) AOD sequences are classified into three types based on
 394 percentile (0-1%, 2% -98%, 99%), (2) When the mean of the third type of AOD is greater than 5 times
 395 the standard bias of the second type, it is considered an imbalanced sequence. These data, with a total
 396 amount less than 5% of the sample, are imbalanced data, and (3) Then synthetic samples are generated
 397 with ~~the a 10%~~ upper limit ~~10%~~ of the original samples.

398 2.7.3 Decision tree regression model

399 The decision tree is a machine learning algorithm based on a tree-like structure used to solve
 400 classification and regression problems. We use regression tree ~~adopt the CART~~ algorithm to construct a
 401 regression ~~tree-model~~ by analyzing the mapping relationship between object attributes (Predictors) and
 402 object values (Target). The internal nodes have binary tree structures with feature values of "yes" and
 403 "no". In addition, each leaf node represents a specific output for a feature space. The advantages of the
 404 regression tree include the ability to handle continuous features and the ease of understanding the
 405 generated tree structure (Teixeira, 2004; Berk, 2008). Before training the tree model, the variables (Input)
 406 are normalized to improve model performance, and after prediction, the results are obtained by
 407 denormalization. The 10-fold cross-validation method is employed to improve the generalization ability
 408 of the model (Browne, 2000).

409 The core problems of the regression tree need to be solved are to find the optimal split variable and
 410 optimal split point. The optimal split point of Predictors is determined by the minimum MSE, which in
 411 turn determines the optimal tree structure. We set $Y = [y_1, y_2, \dots, y_N]$ as the Target. We set $X =$
 412 $[x_1, x_2, \dots, x_N]$ as the Predictors, $x_i = (x_i^1, x_i^2, \dots, x_i^n)$, $i = 1, 2, 3 \dots, N$, where n is the feature number, and
 413 N is the length of sample. We set a training dataset as $D = [(x_1, y_1), (x_2, y_2), \dots, (x_N, y_N)]$.

414 A regression tree corresponds to a split in the feature space and the output values on the split domains.
 415 Assuming that the input space has been divided into M domains $[R_1, R_2, \dots, R_M]$ and there is a fixed
 416 output value on each R_M domain, the regression tree model can be represented as follows:

$$417 f(x) = \sum_{m=1}^M c_m I(x \in R_m), m = 1, 2, \dots, M, \quad (4)$$

418 where I is the indicator function, equation Eq. (5):

$$419 I = \begin{cases} 1, & x \in R_m \\ 0, & x \notin R_m \end{cases}, \quad (5)$$

420 When the partition of the input space is determined, the square error can be used to represent the
 421 prediction error of the regression tree for the training data, and the minimizing square error is used to
 422 solve the optimal output value on each domain. The optimal value (\widehat{c}_m) on a domain is the mean of the
 423 outputs corresponding to all input, namely:

$$424 \widehat{c}_m = ave(y_i | x_i \in R_m), \quad (6)$$

425 A heuristic method is used to split the feature space in CART. After each split, all values of all features
 426 in the current set are examined individually, and the optimal one is selected as the split point based on
 427 the principle of minimum sum of the square errors. The specific step is described as follows: for the
 428 training dataset D , we recursively divide each region into two sub domains and calculate the output
 429 values of each sub domain; then, construct a binary decision tree. For example, split variable is x^j and
 430 split point is s . Then, in the domain $R_1(j, s) = [x|x^j \leq s]$ and domain $R_2(j, s) = [x|x^j > s]$, we can

431 solve the loss function $L(j, s)$ to find the optimal j and s .

$$432 \quad L(j, s) = \sum_{x_i \in R_1(j, s)} (y_i - c_1)^2 + \sum_{x_i \in R_2(j, s)} (y_i - c_2)^2, \quad (7)$$

433 When $L(j, s)$ is the smallest, x^j is the optimal split variable and s is the optimal split point for the
434 x^j .

$$435 \quad \min_{j, s} \left[\min_{c_1} \sum_{x_i \in R_1(j, s)} (y_i - c_1)^2 + \min_{c_2} \sum_{x_i \in R_2(j, s)} (y_i - c_2)^2 \right], \quad (8)$$

436 We use the optimal split variable x^j and the optimal split point s to split the feature space and calculate
437 the corresponding output value.

$$438 \quad \hat{c}_1 = \text{ave}(y_i | x_i \in R_1(j, s)), \quad \hat{c}_2 = \text{ave}(y_i | x_i \in R_2(j, s)), \quad (9)$$

439 We traverse all input variables to find the optimal split variable x^j , forming a pair (j, s) . Divide the
440 input space into two regions accordingly. Next, repeat the above process for each region until the stop
441 condition is met. The regression tree is generated.

442 Therefore, the regression tree model $f(x)$ can be represented as follows:

$$443 \quad f(x) = \sum_{m=1}^M \hat{c}_m I(x \in R_m), \quad m = 1, 2, \dots, M, \quad (10)$$

444 **2.8 Gridding method**

445 ~~Kriging is a regression algorithm to model and predict (interpolate) random processes/fields based on the~~
446 ~~covariance function, which is widely used in geo-statistics (Pebesma, 2004). Ordinary Kriging is the~~
447 ~~earliest and most extensively studied form of Kriging. It is a linear estimation system applicable to any~~
448 ~~intrinsic stationary random field that satisfies the assumption of isotropy. The two key parameters of~~
449 ~~Ordinary Kriging are the semi-variogram function and the weight factors (Goovaerts, 2000). It has been~~
450 ~~widely applied in fields, such as climatology, environmental science, and agriculture (Lapen and Hayhoe,~~
451 ~~2003; Chen et al., 2010), due to high accuracy, stability, and insensitivity to data shape and distribution.~~
452 ~~This study utilizes area-weighted ordinary kriging algorithm to estimate the unknown values of AOD at~~
453 ~~specific locations to generate gridded AOD. The longitude range is between -179.5° E and 180° E, the~~
454 ~~latitude range is between 60° N and 85° N, and the spatial resolution is $0.5^\circ * 0.5^\circ$.~~

455 ~~Kriging variance represents the spatial correlation between different points, which is calculated by the~~
456 ~~semi-variogram function (Goovaerts, 2000). Kriging variance is used to assess the spatial uncertainty of~~
457 ~~interpolation results, indicating the difference between predicted and true values. A higher kriging~~
458 ~~variance indicates fewer neighboring points and greater uncertainty, while a lower variance implies less~~
459 ~~uncertainty. To quantify the uncertainty of interpolation results, we provide the width of the confidence~~
460 ~~interval under the 95% confidence level based on kriging variance (Van Der Veer et al., 2009).~~

461 **2.8.9 Evaluation metrics**

462 Evaluation metrics, including Root Mean Squared Error (RMSE), Mean Absolute Error (MAE) and
463 Pearson Correlation Coefficient (R), are used to measure the performance and accuracy of the model ~~and~~
464 ~~gridded~~ results.

465
$$RMSE = \sqrt{\frac{1}{n} \sum_{i=1}^n (y_i - \hat{y}_i)^2}, \quad (11)$$

466
$$MAE = \frac{1}{n} \sum_{i=1}^n |y_i - \hat{y}_i|, \quad (12)$$

467
$$R = \frac{\sum_{i=1}^n (y_i - \bar{y})(\hat{y}_i - \bar{\hat{y}})}{\text{sqrt}(\sum_{i=1}^n (y_i - \bar{y})^2 \sum_{i=1}^n (\hat{y}_i - \bar{\hat{y}})^2)}, \quad (13)$$

468 where y_i and \bar{y} are the predicted value and the average of the predicted values. \hat{y}_i and $\bar{\hat{y}}$ are
 469 the target and the average of the target. $i = 1, 2, \dots, n$. n is the length of sample.

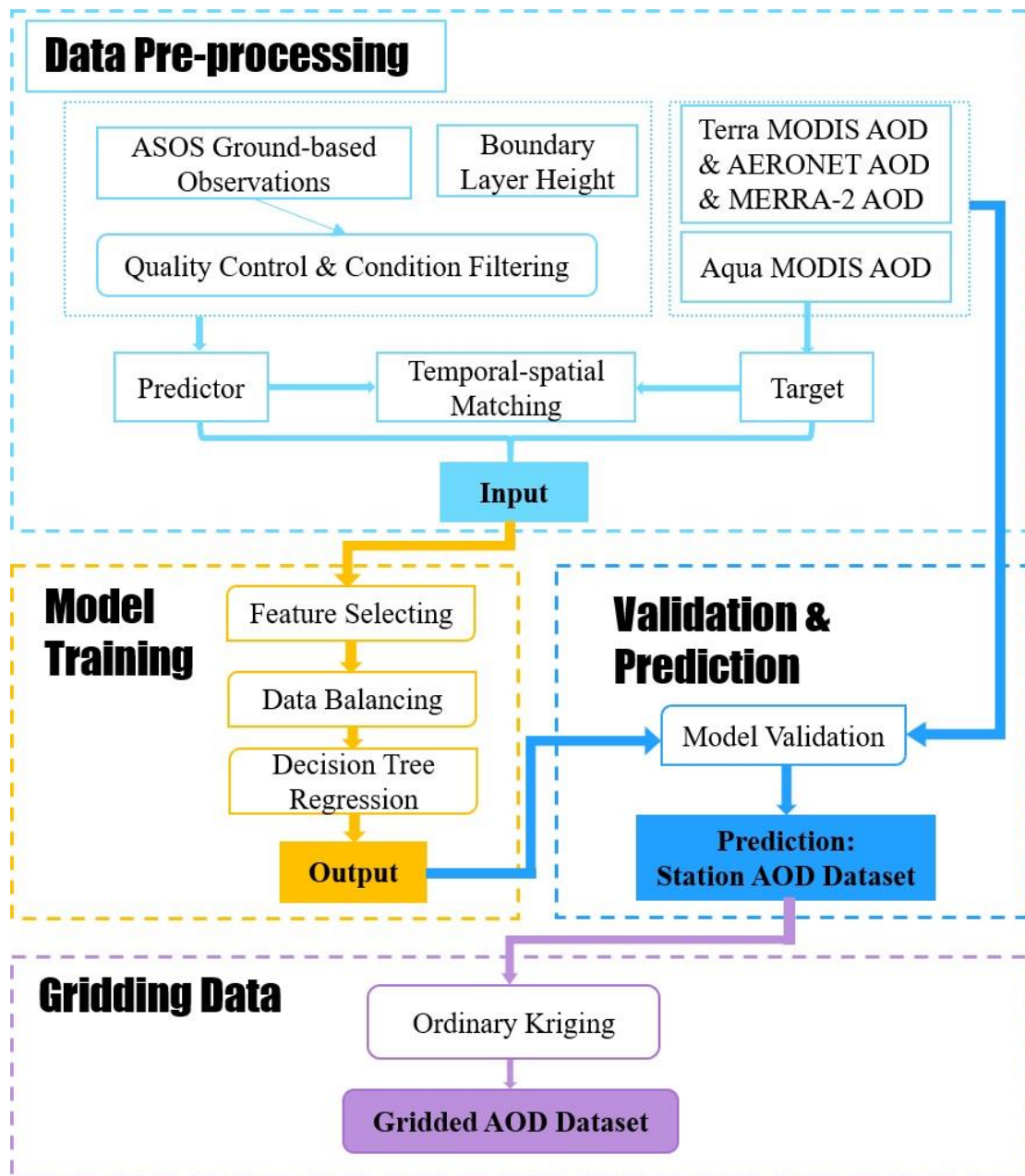
470 The expected error (EE) is used to evaluate the AOD derived from visibility.

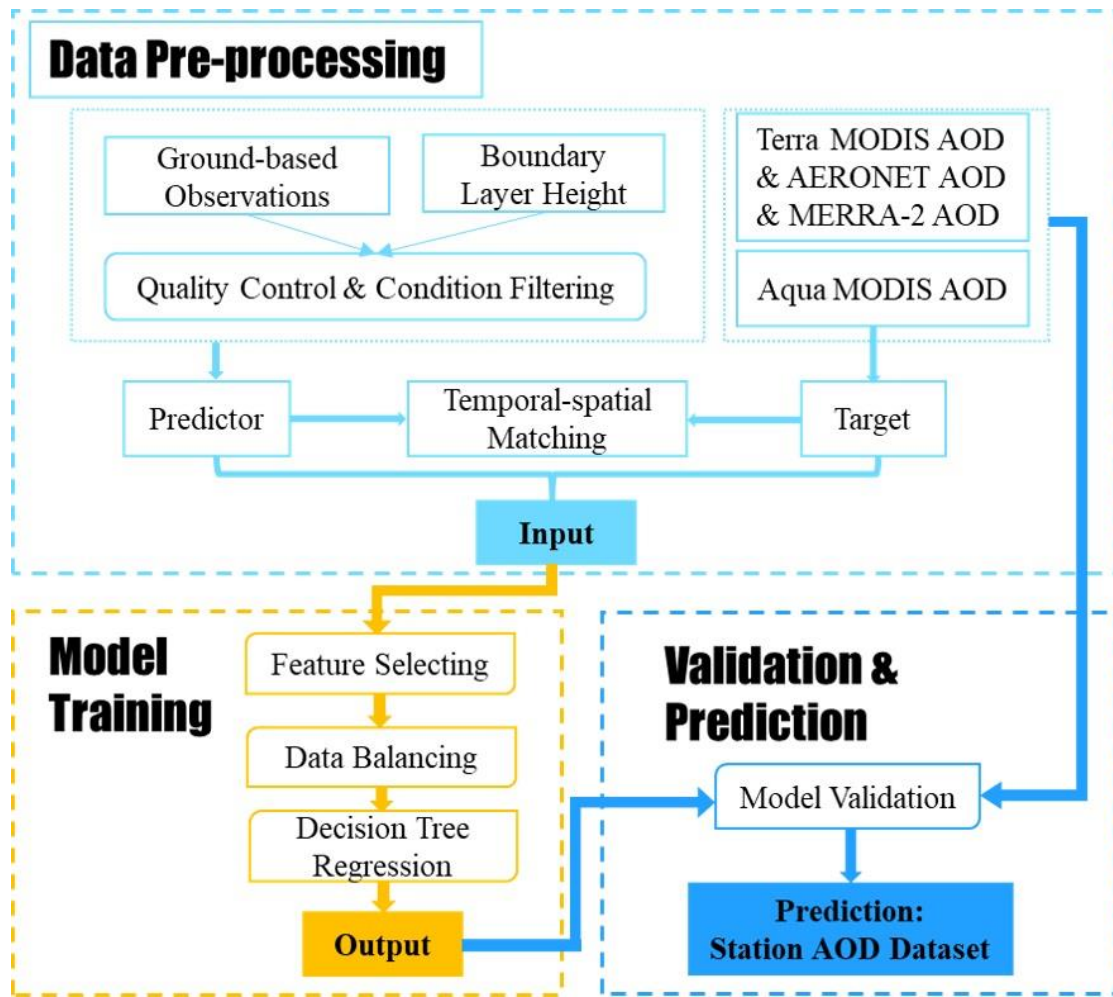
471
$$EE = \pm(0.05 + 0.15 * \tau_{true}), \quad (14)$$

472 where τ_{true} is the AOD at 550 nm from AERONET, satellite and reanalysis datasets.

473 ~~The width of 95% confidence interval (CI) is calculated from the kriging variance (s^2) (Van Der Veer et~~
 474 ~~al., 2009):~~

475 ~~$$95\% \text{ CI} = 1.96 * \sqrt{s^2}, \quad (15)$$~~





477

478 **Figure 2:** Flowchart for deriving aerosol optical depth (AOD).

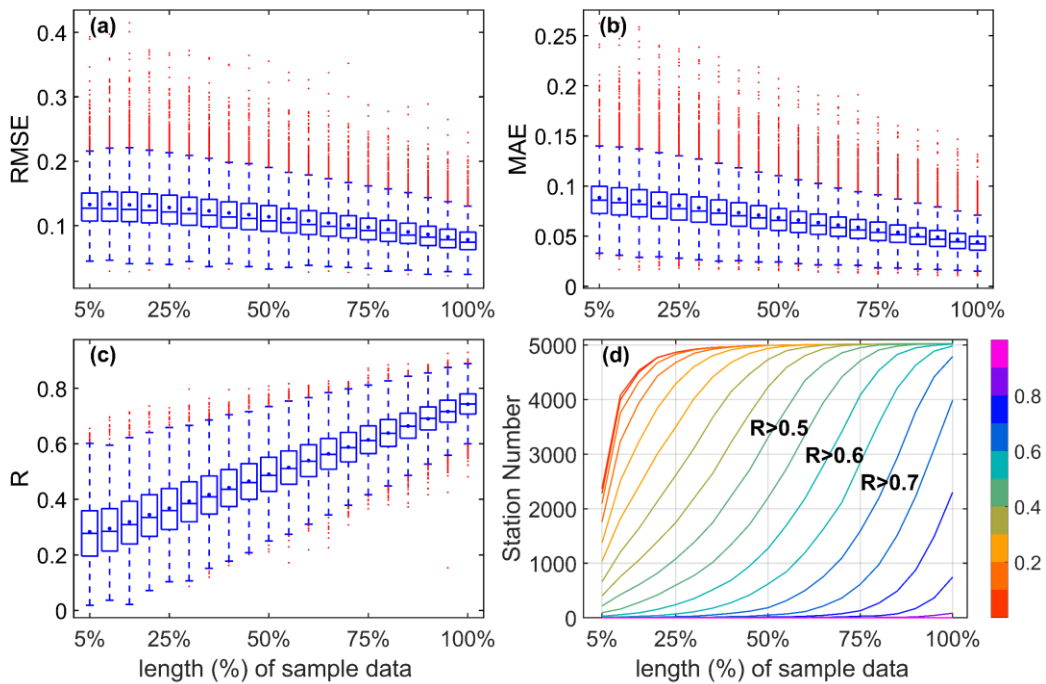
479 **2.910 Workflow**

480 Figure 2 summarizes the flowchart and provides an overview of the structure of this study, which
 481 involves four main parts: (1) data preprocessing, (2) model training, and (3) validation and
 482 prediction, ~~and (4) data gridding.~~

483 **3 Results and discussion**

484 **3.1 Dependence of model performance on training data length**

485



486

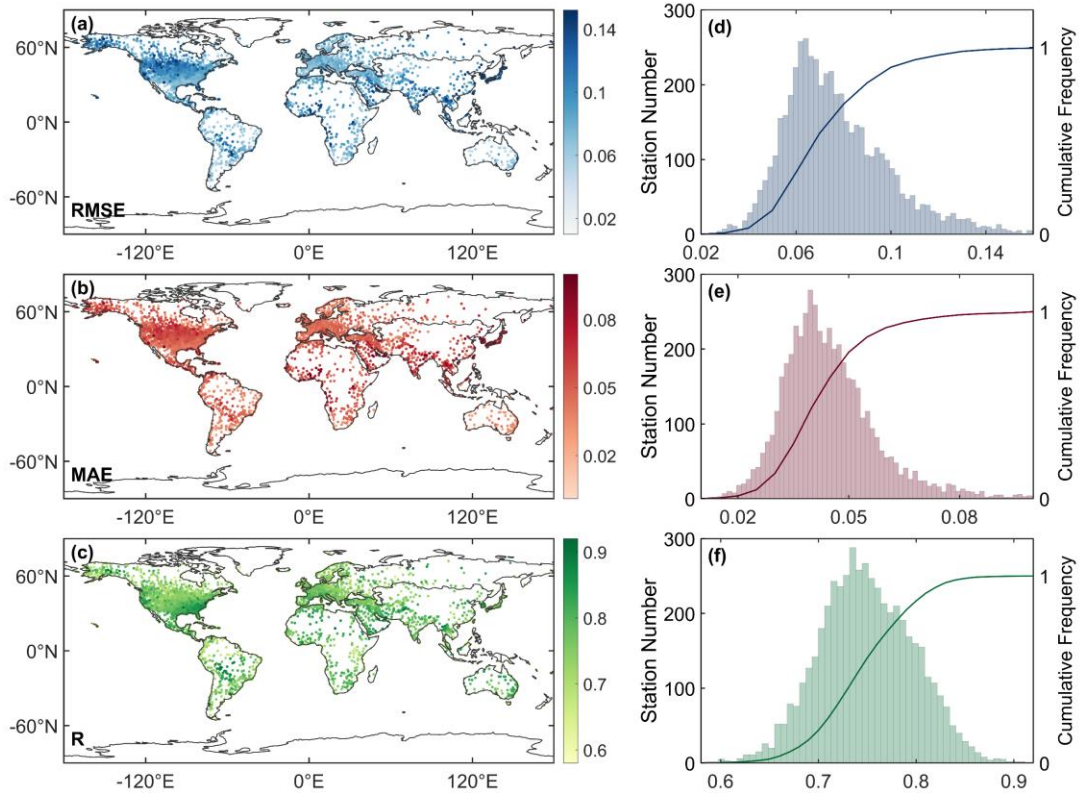
487 **Figure 3:** Boxplots of root mean squared error (RMSE) (a), mean absolute error (MAE) (b), and
 488 correlation coefficient (R) (c) between predicted values and target using different lengths of sample
 489 data (5% interval) as the training dataset, and the correlation coefficient curve (d) of the station
 490 number ~~in the different and~~ lengths of sample data.

491 We build the models using different lengths of sample data (5% to 100%, with a 5% interval) by random
 492 allocation without overlap and evaluate the predictive performance of each model. Figure 3 (a-c) depicts
 493 RMSE(a), MAE(b), and R(c) between the predicted values and target based on the training data of 5%
 494 to 100% sample data at a station. As the volume of the training data increases, the RMSE and MAE
 495 values decrease, and the R values correlation coefficient increases. Compared to 5% of the sample data,
 496 the result of 100% sample data shows a decrease in RMSE by 41.1%, a decrease in MAE by 50.1%, and
 497 an increase in R by 162.3%. The relationship between the length of sample data and the model's
 498 performance is positive for each station. Figure 3 (d) shows that R of approximately 70% stations is
 499 greater than 0.5 at 50% of the sample data, while at 75%, the R of approximately 80% of stations is
 500 greater than 0.6. When 100% of the sample data is used as sample data, the R of approximately 80% of
 501 stations is greater than 0.75, and the R of about 97% is greater than 0.7. This finding indicates that the
 502 predictive capability and robustness of the model increase as the amount of training data increases. It
 503 may be attributed to the model's ability to capture more complex patterns and relationships among the
 504 input by multi-year data.

505 **3.2 Evaluation of model training performance**

506 Figure 4 shows the spatial distribution (a-c) and frequency and cumulative frequency (d-e) of RMSE,
 507 MAE, and R of all stations. The mean values of RMSE, MAE, and R are 0.078, 0.044, and 0.750,
 508 respectively. The RMSE of 93% stations is less than 0.11, the MAE of 91% is less than 0.06, and the R
 509 of 88% is greater than 0.7. The R values in Africa, Asia, Europe, North America, Oceania, and South
 510 America are 0.763, 0.758, 0.736, 0.750, 0.759, and 0.738, respectively. Although the RMSE and MAE

511 of a few stations are high in America and Asia, the R is still high (>0.6). Therefore, the results of the
 512 model's errors demonstrate that the model performs well on almost all stations.



513

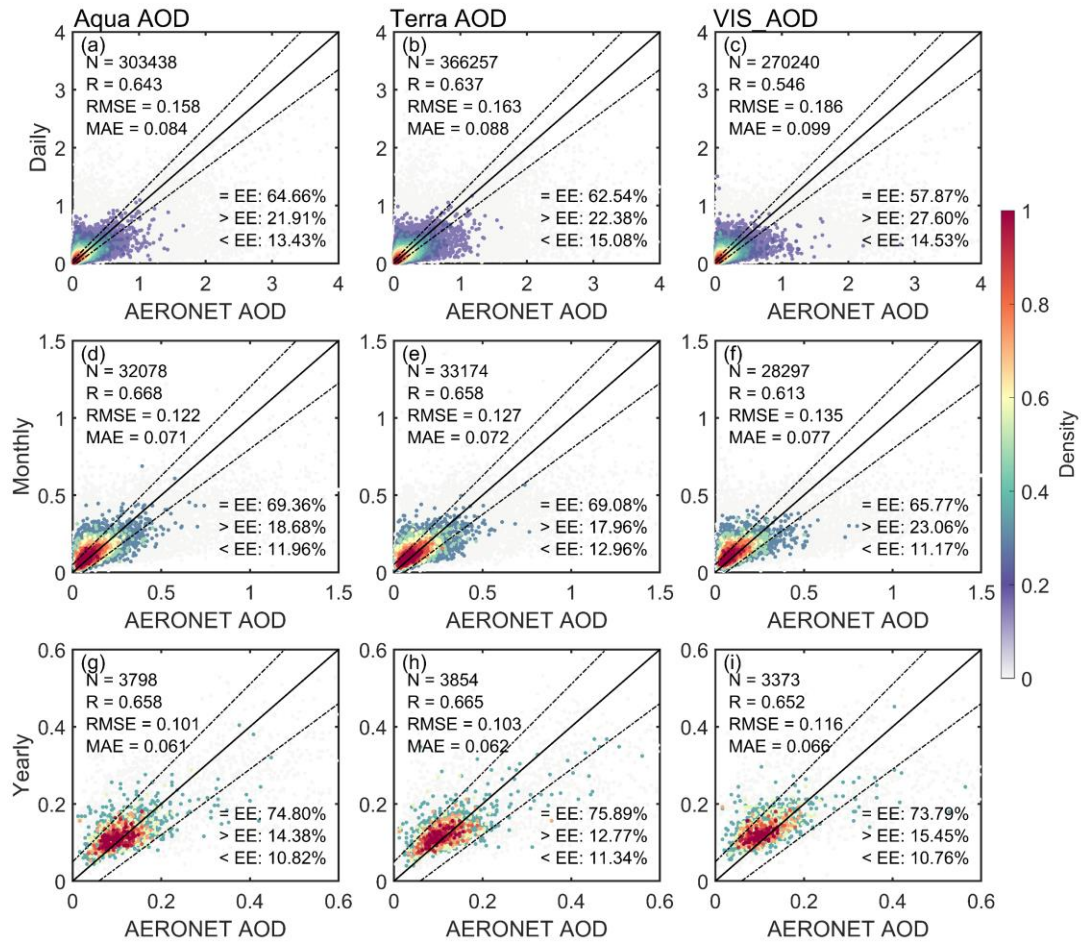
514 **Figure 4:** Spatial distribution (a-c) of root mean squared error (RMSE), mean absolute error (MAE),
 515 and correlation coefficient(R) between the model's result and target with 100% sample data. Station
 516 number (bar) and cumulative frequency (curve) (d-e) of RMSE, MAE, and R.

517 3.3 Validation and comparison with MODIS and AERONET AOD

518 3.3.1 Validation over global land

519 To validate the model's predictive ability, the visibility-derived AOD (for short, VIS_AOD) is compared
 520 with Aqua, Terra, MERRA-2 and AERONET AOD at 550nm for the global scale. Among them, Aqua
 521 AOD has been used as training data, which is not independent. Terra AOD and AERONET AOD have
 522 not been used as training data and can be regarded as independent data.

523 First, the relationship among daily MODIS and AERONET AOD is evaluated, as shown in- Figure 5
 524 ~~shows the scatter density plots between AERONET AOD and Aqua AOD (a-b, d-e, g-h) and Terra AOD~~
 525 ~~(b, e, h)~~. The R values with Aqua AOD and Terra AOD are 0.643 and 0.637 on the daily scale, and 0.668
 526 and 0.658 on the monthly scale, 0.658 and 0.665 on the yearly scale. The RMSE with Aqua AOD and
 527 Terra AOD are 0.158 and 0.163 on the daily scale, and 0.122 and 0.127 on the monthly scale, 0.101 and
 528 0.103 on the yearly scale. The MAE values with Aqua AOD and Terra AOD are 0.084 and 0.088 on the
 529 daily scale, and 0.071 and 0.072 on the monthly scale, 0.061 and 0.062 on the yearly scale. The
 530 percentages of sample point falling within the EE envelopes are 64.66% and 62.54% on the daily scale,
 531 and 69.36% and 69.08% on the monthly scale, 74.80% and 75.89% on the yearly scale.



532

533 **Figure 5:** Scatter density plots between AERONET AOD (550nm) and Aqua MODIS AOD, Terra
534 MODIS AOD and VIS_AOD on the daily (a-c), monthly (d-f) and yearly (g-i) scale. The solid black line
535 represents the 1:1 line and the dashed lines represents expected error (EE) envelopes. The sample size
536 (N), correlation coefficient (R), mean absolute error (MAE), and root mean square error (RMSE) are
537 given. ‘= EE’, ‘> EE’, and ‘< EE’ represent the percentages (%) of retrievals falling within, above, and
538 below the EE, respectively. The matching time for Aqua AOD and VIS_AOD with AERONET AOD is
539 13.30 (\pm 30 minutes) at local time, and the matching time between Terra AOD and AERONET AOD is
540 10.30 (\pm 30 minutes) at local time.

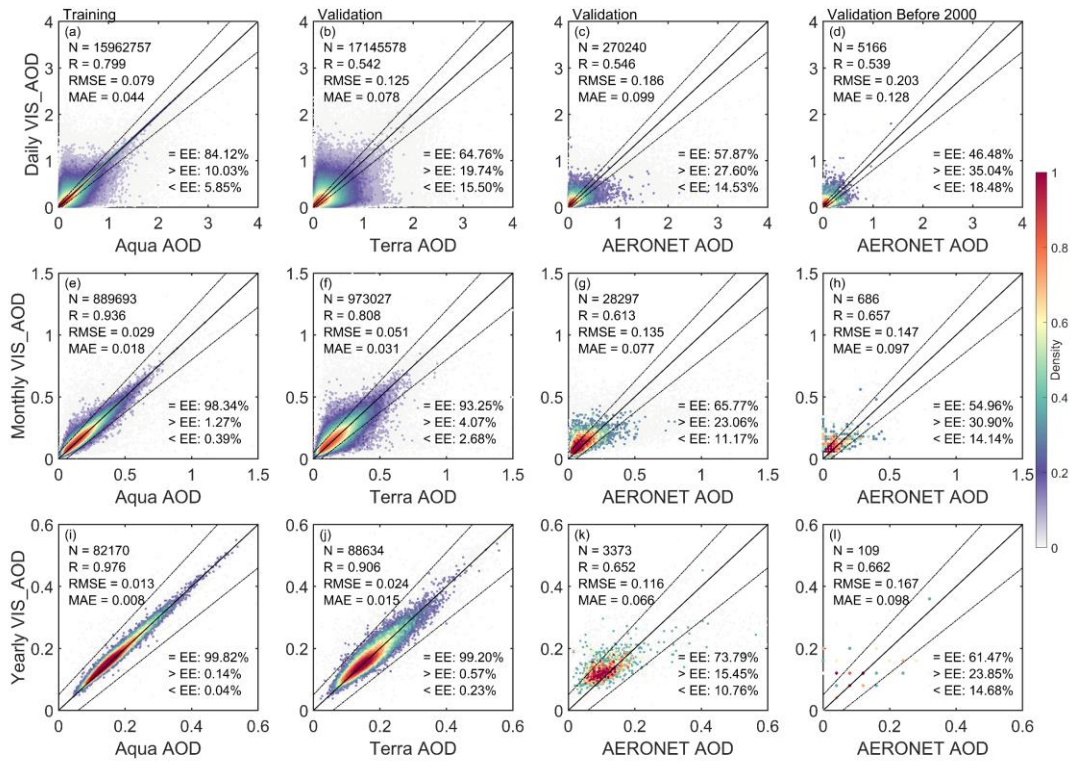
541 Figure 6 shows the scatter density plots and the EEs between VIS_AOD and Aqua AOD, Terra AOD,
542 and AERONET AOD. Aqua AOD is not an independent validation, and Terra and AERONET AOD are
543 independent validation. For the daily scale, the R, RMSE and MAE of between VIS_AOD and Aqua
544 AOD (15,962,757 pairs data) is 0.799, 0.079 and 0.044, respectively. The percentage of sample point
545 falling within the EE envelopes is 84.12% on the global scale (Figure 6 a). The R between VIS_AOD
546 and Terra AOD (17,145,578 pairs data) is 0.542, with a RMSE of 0.125 and MAE of 0.078. The
547 percentage falling within the EE envelopes is 64.76% (Figure 6 b). The R between VIS_AOD and
548 AERONET AOD (270,240 pairs data) at 395 sites is 0.546, with a RMSE of 0.186 and MAE of 0.099.
549 The percentage falling within the EE envelopes is 57.87% (Figure 6 c).

550 For the monthly and annual scales, RMSE and MAE show a significant decrease between VIS_AOD and
551 Aqua, Terra, and AERONET AOD, and R and percentages falling within EE show a significant increase

552 in Figure 6 (e-g, i-k). The monthly RMSEs are 0.029, 0.051, and 0.135, the monthly MAEs are 0.018,
553 0.031, and 0.077, and the monthly R values are 0.936, 0.808, and 0.613, respectively. The percentages
554 falling within the EE envelopes are 98.34%, 93.25%, and 65.77%. The RMSEs at-on the annual-yearly
555 scale are 0.013, 0.024, and 0.116, the MAEs are 0.008, 0.015, and 0.066, and the R values are 0.976,
556 0.906, and 0.652, respectively. The percentages falling within the EE envelopes are 99.82%, 99.20%,
557 and 73.79%. The percentage falling within the EE envelopes against AERONET is smaller than that
558 against Terra, which may be related to the elevation of AERONET sites, the distance between AERONET
559 and meteorological stations, and observed time. The results highlighted above demonstrate a clear
560 improvement in performance on the monthly and annual-yearly scales compared to the daily scale.
561 (~~Schutgens et al., 2017~~), which provided a foundation for the gridded dataset.

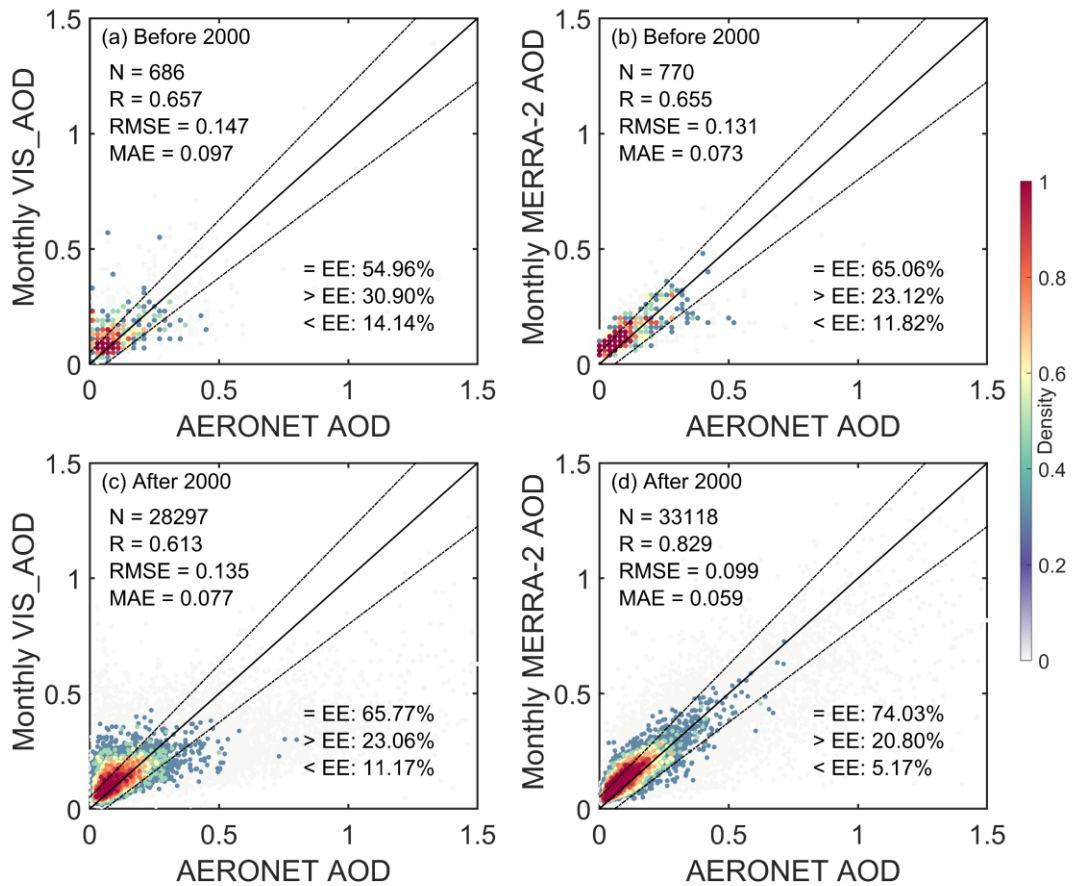
562 To further examine the predictive capability of historical data, we compare the VIS_AOD with
563 AERONET AOD before 2000, as shown in Figure 6 (d, h, l). We match 43 AERONET sites, with a total
564 of 5166 daily records. The result indicates that the daily-scale R is close to that after 2000 (Figure 6 c),
565 with the percentages approaching 50% falling within the EE envelopes. The monthly and annual
566 correlation coefficients are even higher, with a percentage of 55% falling within the EE envelopes.
567 Although the sample size is small, it still demonstrates the excellent predictive ability of the model.
568 Compared with AERONET (an independent validation dataset), the performance of VIS_AOD is almost
569 unchanged before and after 2000.

570 We also compare the VIS_AOD with the MERRA-2 reanalysis AOD on the monthly scales, as shown in
571 Figure 7. The correlation coefficient between MERRA-2 and AERONET is 0.655 before 2000, slightly
572 lower than the correlation coefficient (0.657) between VIS_AOD and AERONET. The correlation
573 coefficient between MERRA-2 and AERONET is 0.829 after 2000, significantly higher than that before
574 2000, while the correlation coefficient between VIS_AOD and AERONET is 0.613. It suggests that
575 VIS_AOD and MERRA-2 AOD have similar accuracy before 2000. The correlation of MERRA-2 after
576 2000 is higher and even performs better than MODIS retrievals (as shown in Figure 5) when evaluated
577 at AERONET sites. However, before 2000, the correlation coefficient of MERRA-2 and AERONET,
578 RMSE, and MAE all show significant changes and differences in consistency. The higher correlation
579 between MERRA-2 and AERONET AOD is partly because MERRA-2 has assimilated AERONET AOD
580 observations (Gelaro et al., 2017). Compared to AERONET, VIS_AOD and Aqua/Terra MODIS have a
581 similar correlation coefficient. The correlation coefficient of VIS_AOD before 2000 is even higher than
582 after 2000, and the changes in RMSE and MAE are not significant. It indicates good consistency of
583 VIS_AOD. In conclusion, the predicted results have good consistency with AERONET AOD and Terra
584 AOD on the daily scale. The monthly and annual results have a significant improvement. The model
585 shows good predictive capabilities before/after 2000, highlighting the stable accuracy of VIS_AOD.



586

587 **Figure 6:** Scatter density plots between predicted AOD (VIS_AOD) and Aqua MODIS AOD, Terra
588 MODIS AOD, AERONET AOD and AERONET AOD before 2000 on the daily (a-d), monthly (e-h) and
589 yearly (g-i) scale. The solid black line represents the 1:1 line and the dashed lines represents expected
590 error (EE) envelopes. The sample size (N), correlation coefficient (R), mean absolute error (MAE), and
591 root mean square error (RMSE) are given. ‘= EE’, ‘> EE’, and ‘< EE’ represent the percentages (%) of
592 retrievals falling within, above, and below the EE, respectively. Note Aqua AOD is not an independent
593 validation dataset for predicted results, while Terra and AERONET AOD are independent validation
594 datasets.



595

596 **Figure 7:** Scatter density plots between AERONET AOD and the predicted AOD (VIS_AOD) and
 597 MERRA-2 AOD before/after 2000 on the monthly scale. The solid black line represents the 1:1 line and
 598 the dashed lines represents expected error (EE) envelopes. The sample size (N), correlation coefficient
 599 (R), mean absolute error (MAE), and root mean square error (RMSE) are given. ‘= EE’, ‘> EE’, and ‘<
 600 EE’ represent the percentages (%) of retrievals falling within, above, and below the EE, respectively.

601 3.3.2 Validation over regions

602 Aerosol loading exhibits spatial variability. Evaluation metrics for the relationships between
 603 visibility-derived AOD and AERONET AOD and Terra AOD for each region are listed in Table 1.

604 Over-In Europe and North America, the results are similar to those of Terra and AERONET, with a
 605 large number of data pairs, greater than 10^5 (AERONET) and greater than 10^7 except for Eastern
 606 Europe (Terra) on the daily scale. Approximately 63% -70% data pairs fall within the EE envelopes.
 607 The RMSE is approximately 0.1100, except for western North America (~0.15), and the MAE is
 608 approximately 0.0700, with and the α -correlation coefficient is between 0.44 and 0.54.

609 Over-In Central South America, South Africa, and Australia, data pairs are about 10^{3-4} (AERONET)
 610 and 10^6 (Terra) on the daily scale. 52-60% fall within the EE envelopes compared to AERONET,
 611 and 58-67% compared to Terra. The RMSE is 0.03-0.05 compared to Terra, and 0.11-0.17 compared
 612 to AERONET. The correlation coefficient ranges from 0.40 to 0.74, with the highest correlation
 613 coefficient in South America at 0.740.

614 In Asia, India, and West Africa, the data pairs are only approximately 10^4 (AERONET). 32% to 50%

615 fall within the EE envelopes compared to AERONET, the RMSE value ranges from 0.20 to 0.50,
616 and the MAE ranges from 0.11 to 0.36. ~~Compared to Terra AOD, 51 to 58% of data pairs, compared~~
617 ~~to Terra,~~ fall within the EE envelopes, the RMSE is around 0.16, and the MAE is around 0.11.
618 Compared to AERONET, in these high aerosol loading regions, RMSE and MAE increase, and the
619 percentages falling within the EE envelopes decrease, but the correlation coefficients do not
620 significantly decrease.

621 Compared to Terra AOD, 55% -67% of data falls within the EE envelopes on the daily scale, 87% -
622 96% on the monthly scale, and over 97% on the yearly scale. Compared to AERONET AOD, 32-
623 68% of data falls within the EE envelopes, 24% -84% on the monthly scale, and 15% -97% on the
624 yearly scale. On both monthly and yearly scales, all metrics have shown a significant increase in
625 performance when compared to Terra. However, compared to AERONET, not all metrics increase
626 in some regions due to limited data pairs, such as West Africa, Northeast Asia, and India, which may
627 be due to the spatial differences between AERONET sites and meteorological stations.

628 3.3.3 Validation at a site scale

629 Sites, especially AERONET, are not completely uniform across the world or in any region, and
630 different stations have different sample sizes, which may lead to a certain uncertainty. Therefore,
631 further analysis ~~was-is~~ conducted on the spatial distribution of different evaluation metrics. Figure 8
632 shows the validation and comparison of daily VIS_AOD against Terra and AERONET AOD at a
633 site scale.

634 Compared to Terra daily AOD, the R of 67% stations is greater than 0.40, the mean bias of 83% is

Table 1: Evaluation metrics for the relationships between visibility-derived AOD and AERONET AOD and Terra AOD for each region.

Region		N			R			RMSE			MAE			Within EE (%)		
		daily	monthly	yearly	daily	monthly	yearly	daily	monthly	yearly	daily	monthly	yearly	daily	monthly	yearly
Eastern Europe	AERONET	21724	2317	271	0.463	0.493	0.653	0.1069	0.0647	0.0326	0.0714	0.0442	0.0263	65.69	83.77	97.42
	TERRA	661630	36435	3278	0.464	0.665	0.790	0.1095	0.0471	0.0214	0.0726	0.0286	0.0122	66.07	94.71	99.18
Western Europe	AERONET	53043	6033	697	0.445	0.487	0.344	0.1089	0.0716	0.0513	0.0711	0.0474	0.0347	64.40	79.21	89.10
	TERRA	1778013	104620	9166	0.467	0.763	0.811	0.1096	0.0391	0.0210	0.0712	0.0268	0.0124	66.99	95.42	99.40
Western North America	AERONET	33859	2948	334	0.503	0.484	0.509	0.1465	0.0949	0.0566	0.0747	0.0597	0.0419	63.58	67.37	81.14
	TERRA	1725226	82734	7201	0.542	0.765	0.906	0.1144	0.0465	0.0180	0.0671	0.0267	0.0125	69.48	94.42	99.61
Eastern North America	AERONET	47407	5359	608	0.527	0.526	0.559	0.1135	0.0824	0.0436	0.0657	0.0472	0.0331	67.52	77.78	87.50
	TERRA	6280277	359520	31343	0.515	0.799	0.847	0.1159	0.0435	0.0165	0.0726	0.0275	0.0111	66.70	94.94	99.80
Central South America	AERONET	10911	1176	149	0.740	0.811	0.866	0.1735	0.1272	0.1060	0.1021	0.0904	0.0688	52.40	47.96	67.79
	TERRA	444780	26362	2410	0.545	0.820	0.776	0.1447	0.0591	0.0369	0.0909	0.0396	0.0219	58.48	89.29	97.39
Southern Africa	AERONET	4255	309	38	0.423	0.480	0.630	0.1553	0.1128	0.0705	0.1033	0.0805	0.0525	52.08	59.55	78.95
	TERRA	216239	11304	1118	0.518	0.821	0.870	0.1258	0.0511	0.0296	0.0836	0.0340	0.0191	60.64	91.70	98.21
Australia	AERONET	6426	516	63	0.488	0.654	0.363	0.1094	0.0827	0.0725	0.0711	0.0620	0.0563	59.96	59.88	71.43
	TERRA	284693	14588	1286	0.398	0.784	0.831	0.1091	0.0363	0.0188	0.0666	0.0261	0.0143	67.01	94.65	99.38
Western Africa	AERONET	2205	205	34	0.553	0.594	0.762	0.3180	0.2873	0.3357	0.2082	0.2029	0.2587	37.96	40.00	23.53
	TERRA	156392	10468	1028	0.501	0.769	0.849	0.1769	0.0706	0.0412	0.1198	0.0482	0.0242	51.83	88.01	97.57
Southeast Asia	AERONET	4134	504	74	0.405	0.542	0.488	0.2037	0.1447	0.1198	0.1274	0.0988	0.0821	50.17	56.15	60.81
	TERRA	402465	27058	2500	0.470	0.753	0.872	0.1730	0.0729	0.0342	0.109	0.0455	0.0198	57.25	87.01	97.96
Eastern China	AERONET	7396	927	118	0.513	0.551	0.356	0.3571	0.2355	0.1933	0.2038	0.1392	0.1382	40.10	49.84	50.00
	TERRA	241185	17324	1518	0.523	0.811	0.895	0.1646	0.0638	0.0302	0.1073	0.0435	0.0225	55.77	88.07	98.88
Northeast Asia	AERONET	9979	1178	142	0.569	0.593	0.367	0.4941	0.3249	0.2604	0.2924	0.2425	0.2202	35.17	29.54	21.13
	TERRA	78823	5485	467	0.553	0.872	0.965	0.1973	0.0636	0.0263	0.1201	0.0440	0.0198	56.48	87.77	98.29

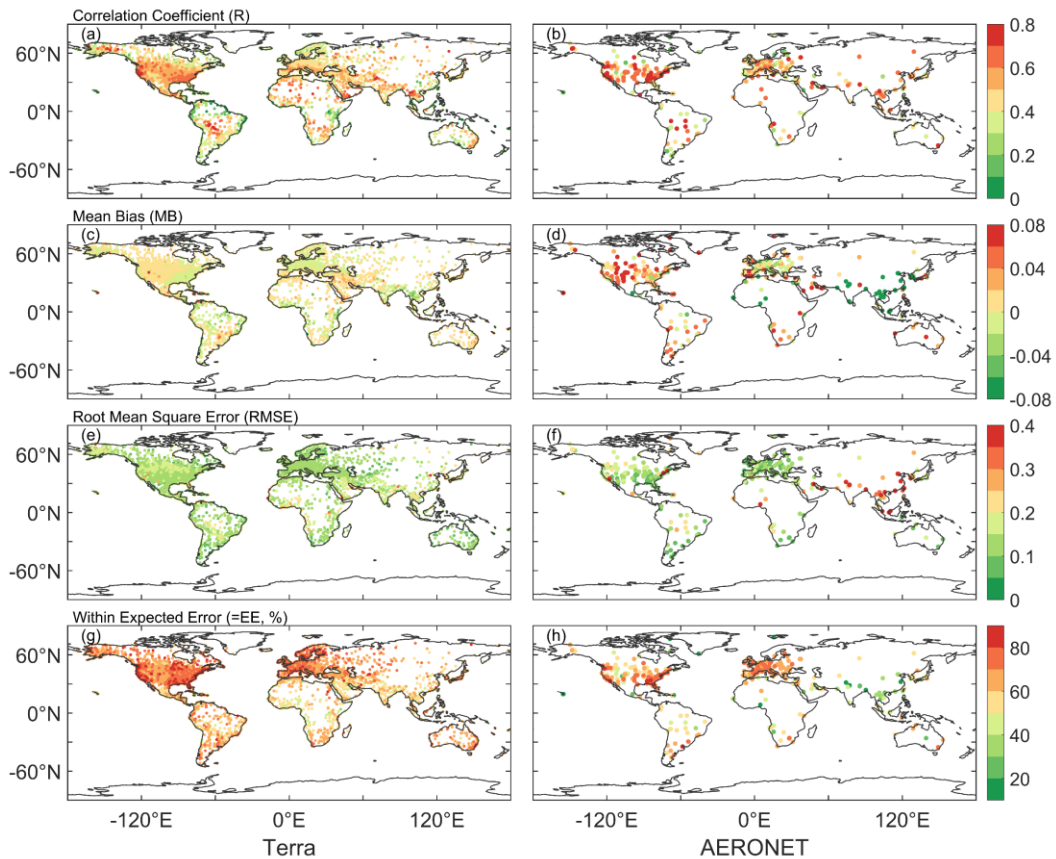
<i>India</i>	<i>AERONET</i>	2208	203	32	0.521	0.462	0.534	0.2957	0.3015	0.3588	0.2049	0.2283	0.2862	32.11	24.63	15.63
	<i>TERRA</i>	179928	9564	862	0.526	0.815	0.915	0.1564	0.0599	0.0352	0.1089	0.042	0.0238	55.16	90.43	98.14

636

637 less than 0.01, the RMSE of 85% is less than 0.15, and the percentage falling within the EE of 67%
638 is greater than 60%. More than 85% of stations fall within the EE is greater than 60% in Europe,
639 North America, and Oceania, while 40-60% in South America, Africa, and Asia. The percentage of
640 expected error is low in South and East Asia, and Central Africa, with some underestimation. Above
641 60% in Africa, Asia, North America, and Europe have a correlation coefficient greater than 0.40.
642 The regions with lower correlation are the coastal regions of South America, eastern Africa, western
643 Australia, northeastern North America, and northern Europe. Above 90% of the RMSE in Europe,
644 North America, and Oceania have a correlation coefficient smaller than 0.15. High RMSE regions
645 are in western North America, Asia, central South America, and central Africa.

646 Compared to AERONET daily AOD, the R of 74% stations is greater than 0.40, and the spatial
647 distribution is similar to Terra's. The mean bias of 44% is less than 0.01, the RMSE of 68% is less
648 than 0.15, and the percentage falling within the EE of 53% is greater than 60%. More than 70% of
649 sites have a correlation coefficient greater than 0.40 in Africa, Asia, Europe, and North America.
650 More than 57% of sites have an expected error percentage of over 60% in Europe, North America,
651 and Oceania, except for Asia. Over 72% of sites have a RMSE less than 0.15. Except for Oceania
652 and South America, over 71% of sites in other regions have MAE less than 0.01. Almost all sites in
653 Asia show a negative bias, significantly underestimating. However, there is a significant
654 overestimation in western North America and western Australia. Most sites in Asia falling within
655 the expected error are less than 50%. High RMSE are in high emission and dust areas, such as Asia,
656 India, and Africa.

657 The validation and comparison on the site scale show a limitation similar to the MODIS DT
658 algorithm. In areas with high vegetation coverage, the AOD from visibility are better than those in
659 bright areas. Although the correlation coefficients are high in high aerosol loading areas (Central
660 South America, West Africa, India, Eastern China, Northeast Asia), there are significant differences
661 in these areas with high RMSE values. As shown in Figure 6, some stations located in dusty and
662 urban areas are overestimated or underestimated. Studies have shown that there is a significant
663 uncertainty in the MODIS retrievals in these regions, and the challenges of inversion algorithms are
664 significant in bright surfaces (desert and snow covered areas) and urban surface of densely
665 populated complex structures (Chu et al., 2002; Remer et al., 2005; Levy et al., 2010; Wei et al.,
666 2019; Wei et al., 2020). In India, the elevation difference between AERONET site and
667 meteorological station reached 0.7km may be a factor affecting the validation effect, as aerosol
668 varies greatly with altitude. In eastern China, the complex urban surface, emission sources, and
669 observations in different locations (AERONET site and meteorological station) may be the reasons
670 for underestimation. At the same time, visibility stations in desert areas are sparse, and the spatial
671 variability of dust aerosols is large, which also increases the difficulty to estimate VIS_AOD.



672
 673 **Figure 8:** Validation of VIS_AOD against Terra and AERONET AODs at each site: (a–b)
 674 correlation (R), (c–d) mean bias (MB), (e–f) root mean square error (RMSE), (g–h) percentage (%)
 675 of VIS_AOD within the expected error envelopes.

676 3.3.4 Discussion and uncertainty analysis

677 The atmospheric visibility is a horizontal physical quantity, while AOD is a column-integrated
 678 physical quantity. We have linked the two variables together using machine a learning method,
 679 which partially compensates for the scarcity of AOD data. However, we have to face some
 680 limitations. Although the boundary layer height is considered, it is not sufficient. Pollutants such as
 681 smoke from biomass burning, dust, volcanic ash, and gas-aerosol conversion of sulfur dioxide to
 682 sulfate aerosols in the upper and lower troposphere can undergo long-range aerosol transport under
 683 the influence of circulation. The pollution transport and aerosol conversion processes above the
 684 boundary layer are still significant and cannot be ignored (Eck et al., 2023). Compared to surface
 685 visibility, bias occurs when the aerosol layer rises and affects AERONET measurements and
 686 MODIS retrievals. Therefore, it should be considered when using this data. If there were sufficient
 687 historical vertical aerosol measurements with high temporal and spatial resolution, the results of this
 688 data would be greatly improved. Although some studies use aerosol profiles from pollution transport
 689 models or assumed profiles as substitutes for observed profiles (Li et al., 2020; Zhang et al., 2020),
 690 the biases introduced by these non-observed profiles are still significant.

691 In machine learning, we use MODIS Aqua AOD as the target value for the model because the
 692 validation results for MODIS C6.1 product have a correlation coefficient of 0.9 or higher with
 693 AERONET AOD on the daily scale (Wei et al., 2019; Wei et al., 2020). Compared to AERONET,
 694 MODIS AOD provides more sample data with a high global coverage. However, apart from

695 modeling errors, the systematic biases and uncertainties of MODIS Aqua AOD cannot be ignored
696 (Levy et al., 2013; Levy et al., 2018; Wei et al., 2019). Averaging over time scale can reduce
697 representation errors effectively, and emission sources and orography can increase representation
698 errors (Schutgens et al., 2017). Therefore, the strong correlation at monthly and annual scales
699 indicates a substantial reduction in errors. This is also one of the reasons why this dataset shows
700 stronger correlation with Terra AOD and weaker correlation with AERONET in validation.

701 The spatial matching between meteorological stations and AERONET sites may cause some biases.
702 AERONET sites are usually not co-located with meteorological stations in terms of elevation and
703 horizontal distance, this is another reason for the weak correlation between VIS_AOD and
704 AERONET AOD. The meteorological stations are located at the airport. Different horizontal
705 distances may result in meteorological stations and AERONET sites being located on different
706 surfaces (such as urban, forest, mountainous). Differences in site elevation significantly impact the
707 relationship between AOD and measured visibility. When the AERONET site is at a higher elevation
708 than the meteorological station, there may be fewer measurements of aerosols over the sea at the
709 AERONET site.

710 Different pollution levels and station elevation affect the AOD derived from visibility. The elevation
711 difference and distance between meteorological stations and AERONET sites also have an impact
712 on the validation results. Therefore, the error and performance of different AERONET AOD values,
713 station elevation, and distance are analyzed.

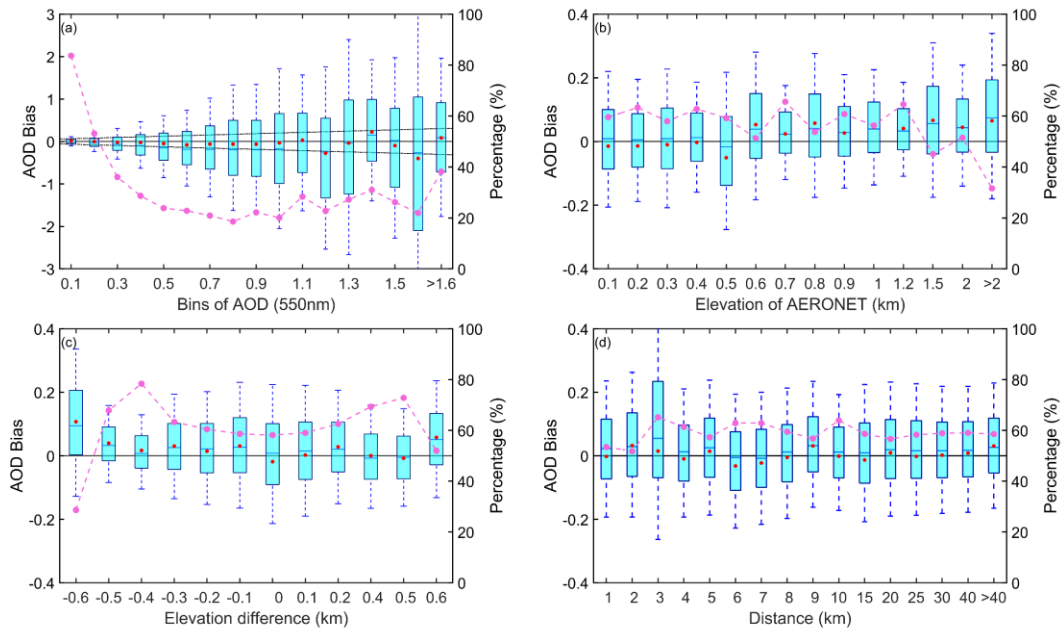
714 As the AOD increases, the variability of bias also increases in Figure 9 (a). Almost all mean bias
715 values are within the envelope of EE, except for 1.1-1.2 and 1.5-1.6. The average bias is 0.015
716 (AOD <0.1), with 83% of data within the EE envelopes. The mean bias is -0.0011 (AOD, 0.1-0.2),
717 with 54% within the EE envelopes. The mean bias is negative (AOD, 0.3-1.0), with 20%-40%
718 falling within the EE envelopes. There is a positive bias (AOD, 1.1, 1.4 and >1.6), and there is a
719 negative bias at 1.2-1.3 and 1.5-1.6. The results indicate that as pollution level increases, the
720 negative mean bias becomes significant and the underestimation increases.

721 The contribution of particulate matter near the ground to the column aerosol loading is significant.
722 The elevation of the site affects the measurement of column aerosol loading in Figure 9 (b). There
723 is a negative bias in the low elevation (≤ 0.5 km) with a percentage of 60%-64% falling within the
724 EE envelopes and a positive bias in high elevation (0.5-1.2km) with a percentage of 50%-65%
725 falling within the EE envelopes. The percentage significantly decreases (> 1.2 km), and the average
726 bias increases. Therefore, the elevation of AERONET's site will cause bias in validation, and the
727 uncertainty greatly increases in high elevation.

728 Due to the elevation difference between the meteorological station and AERONET site in the
729 vertical direction, the uncertainty caused by elevation differences of site was analyzed in Figure 9
730 (c). When the elevation difference is negative (the elevation of the meteorological station is lower
731 than that of the AERONET station), there is a significant positive bias. When the difference is
732 positive, the mean bias approaches 0 or is positive. The percentage is greater than 60% (-0.5 km-
733 0.5km). The positive mean bias is greater than the negative mean bias, and the uncertainty greatly
734 increases when the elevation of meteorological stations is lower than that of AERONET sites. It
735 indicates that the contribution of the near surface aerosol to the column aerosol loading is significant
736 and cannot be ignored.

737 The spatial variability of aerosols is significant. Meteorological stations and AERONET sites are
738 not collocated, resulting in a certain distance in spatial matching. In this study, the upper limit of

739 distance is 0.5 degree. Figure 9 (d) shows the error of the distance between stations, where the
 740 degree is converted to the distance at WGS84 coordinates. The bias does not change significantly
 741 with increasing distance. The average bias is around 0, with the maximum positive mean bias
 742 (0.0322) at a distance of 2km and the maximum negative mean deviation (-0.0323) at 6km. The
 743 median is almost positive, except at 5km and 6km. The percentage falling within the EE envelopes
 744 is over 50%, with the maximum percentage (66%) at 3km and the minimum (62%) at 2km.



745

746 **Figure 9:** Box plots of AOD bias and the percentage falling within the EE envelopes (curves): (a)
 747 AERONET AOD levels, (b) elevation of AERONET sites, (c) elevation difference between
 748 meteorological stations and AERONET sites, (d) distance (km) between meteorological stations and
 749 AERONET sites. The black horizontal line represents the zero bias. For each box, the upper, lower,
 750 and middle horizontal lines, and whiskers represent the AOD bias 75th and 25th percentiles, median,
 751 and 1.5 times the interquartile difference, respectively. The black solid lines represent the EE
 752 envelopes ($\pm(0.05+0.15*AOD_{AERONET})$). No site with a difference of +0.3km (x-axis label without
 753 0.3) in (c).

754 3.4 Gridded visibility-derived AOD

755 3.4.1 Uncertainty of gridded AOD

756 We calculate the width of the 95% CI for gridded AOD. Figure 10 (a-b) shows the spatial distribution
 757 and frequency of the 95% CI from 1980 to 2021. In areas with dense visibility stations, the kriging
 758 variance is low, the width of 95% CI is small, and the uncertainty of the gridded AOD is low. In
 759 areas with sparse visibility stations, the width is large, and the uncertainty is high. The uncertainty
 760 of approximately 43% of the grids is less than 0.03, and nearly 80% has an uncertainty less than
 761 0.06. Approximately 7% of the grids have an uncertainty larger than 0.1. Regions with low
 762 uncertainty are mainly located in North America (<60°N), Europe, Western and Southern Asia,
 763 Eastern China, and South America. Regions with high uncertainty are found in high latitude areas
 764 (e.g., Siberia), high altitude regions (e.g., Tibetan Plateau), and desert areas (such as the Sahara

Desert, Taklamakan Desert, and Australian deserts).

Uncertainty also exhibits seasonal variations, as shown in Figures (e-f). The percentage of grid cells with uncertainty less than 0.06 is 63%, 84%, 77%, and 86% in DJF, MAM, JJA, and SON, respectively. Compared to other seasons, uncertainty increases significantly in high-latitude regions, Africa, northern Asia, Oceania, and eastern South America during DJF. In JJA, the distribution of uncertainty is similar to DJF, but the uncertainty decreases. In MAM and JJA, there is higher confidence, with a small number of grid cells having large uncertainty (>0.1), primarily concentrated in high-latitude regions.

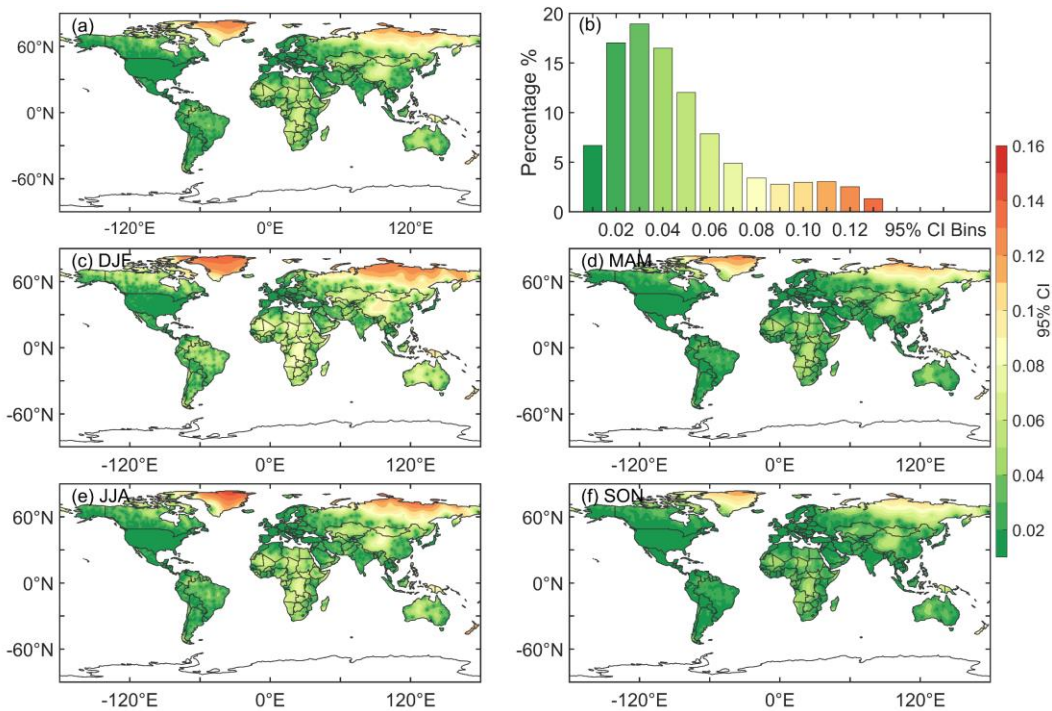
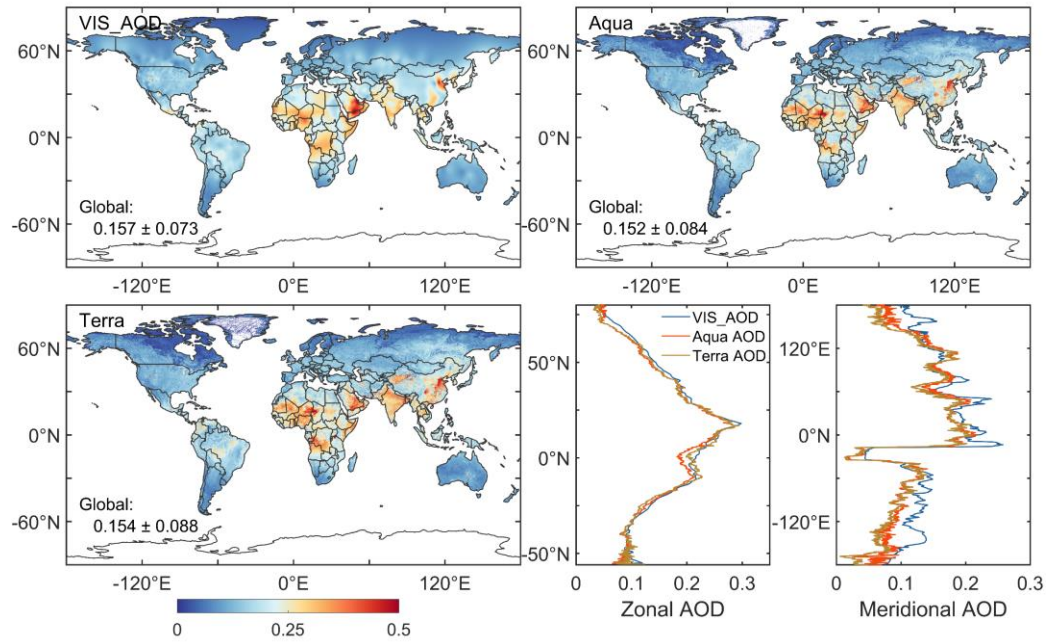


Figure 10: The spatial distribution (a) and frequency (b) of the 95% confidence interval (CI) from 1980 to 2021. The spatial distribution of the width of the 95% CI for each season (c-f). Bins of 95% CI are from 0 to 0.15 with an interval of 0.01. DJF represents December and next January and February. MAM represents March, April, and May. JJA represents June, July, and August. SON represents September, October, and November.

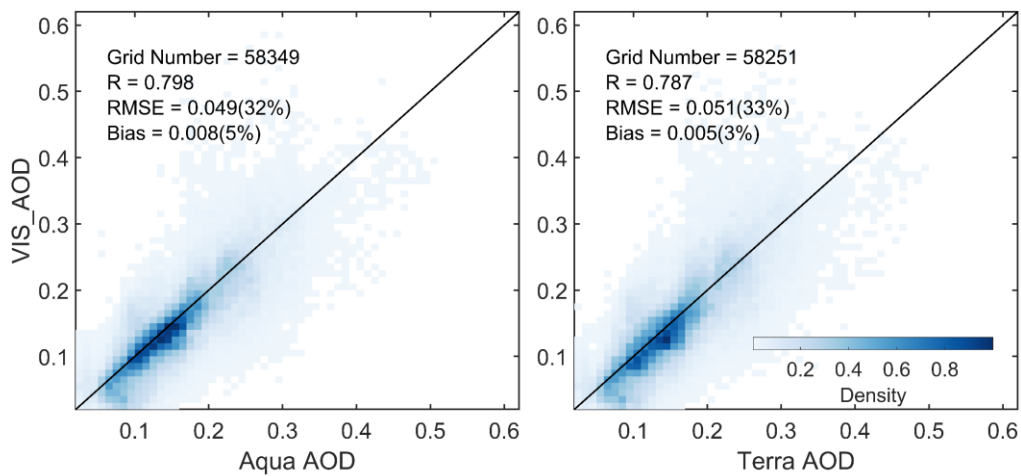
3.4.2 Comparison with Aqua/Terra MODIS AOD

Figure 11 shows the gridded AOD based on ordinary kriging interpolation with the area-weighted method and compares the multi-year spatial, zonal, and meridional distributions of AOD with Aqua and Terra AOD over land from 2003 to 2021. The VIS_AOD is 0.157 ± 0.073 over land, which is almost equal to the Aqua (0.152 ± 0.084) and Terra (0.154 ± 0.088) AOD values with relative biases of 3.3%, and 1.9%, respectively. In order to compare the spatial correlation, Aqua and Terra MODIS AOD are averaged to the 0.5-degree resolution. In the heatmap (Figure 12), the R of VIS_AOD and Aqua AOD is 0.798, the RMSE is 0.049 with a bias of 32% compared to the mean, and the MAE is 0.008, with a bias of 5% compared to the mean. Compared to Terra AOD, the R is 0.787, and the RMSE is 0.051, with a bias of 33% compared to the mean, and the MAE is 0.005, with a bias of 3% compared to the mean. The R between Aqua and Terra AOD is 0.980. The R values between

790 VIS_AOD and Aqua and Terra AOD are 0.995 and 0.990 for the zonal distribution and 0.986 and
 791 0.897 for the meridional distribution, respectively. In the low aerosol loading region, VIS_AOD
 792 exhibits a little overestimation. Whether in meridional or zonal distribution, the peak and valley
 793 regions are basically consistent (Tian et al., 2023). Due to the limitations of satellite inversion
 794 algorithms, a bias appears on the bright surface, especially in northern North America with extensive
 795 snow cover (Levy et al., 2013). All above results suggest that the gridded AOD is consistent with
 796 satellite retrievals in spatial distribution.



798
 799 **Figure 11:** The spatial, zonal and meridional distributions of the multi-year mean VIS_AOD, Aqua
 800 AOD, and Terra AOD over land from 2003 to 2021.



802
 803 **Figure 12:** Heatmap of multi-year mean gridded VIS_AOD and Aqua AOD and Terra AOD during
 804 2003-2021. Terra and Aqua AOD are averaged onto a grid of 0.5°.

3.45 Interannual variability and trend of visibility-derived AOD over global land

The ~~spatial distribution of~~ multi-year average AOD from 1980 to 2021 over land is 0.177, as shown in Figure 103 (a). The ~~mean AOD average is 0.178 in of land (-60-85°N)~~, Northern Hemisphere (NH, ~~0-85°N 4532 stations~~); and 0.174 in the Southern Hemispheres (SH, ~~-60-0°N 500 stations~~), is 0.161 ± 0.074 , 0.158 ± 0.076 , and 0.173 ± 0.059 , respectively. The AOD values of Africa, Asia, Europe, North America, Oceania, and South America are ~~0.241, 0.222, 0.110, 0.111, 0.129 and 0.117, respectively.~~

Due to the influence of geography, atmospheric circulation, population, and emissions, the AOD varies in different latitudes. Figure 114 illustrates the multi-year average AOD in different latitude ranges ~~for land, the NH, and the SH~~ from 1980 to 2021. The AOD value in the NH is higher than that over land, then higher than that in the SH. Within [-20, 20°N], the ~~global~~ average AOD reaches its maximum (~~0.222534~~), and the maximum AOD in the NH is ~~0.23956~~ in [0, 20°N]. The highest AOD ~~in SH in the SH~~ is ~~0.20317~~ in [-15, 0°N]. The average AOD ~~in SH~~ rapidly decreases from -15°N to -35°N in the SH and from 20°N to 50°N in the NH. ~~In NH, AOD is generally greater than in SH from 5°N to 65°N. When, the latitude is greater than 70°N, the NH's AOD is smaller than the SH's.~~

There are many regions of high AOD values occur in the NH, with the distribution of high population density. Approximately 7/8 of the global population resides in the NH, with 50% concentrated at 20°N-40°N (Kummu et al., 2016), indicating a significant impact of human activities on aerosols. The highest AOD values are observed near 17°N, including the Sahara Desert, Arabian Peninsula, and ~~southeastern~~ India, suggesting that in addition to anthropogenic sources, deserts also play a crucial role in aerosol emissions. Lower AOD regions of the SH are from 25°S to 60°S, encompassing Australia, southern Africa, and southern South America, indicating lower aerosol burdens in these areas. Additionally, North America also exhibits low aerosol loading. Chin et al. (2014) analyzed the AOD over land from 1980 to 2009 with the Goddard Chemistry Aerosol Radiation and Transport model, which is similar to the visibility-derived AOD. The spatial distribution is consistent with the satellite results (Remer et al., 2008; Hsu et al., 2012; Hsu et al., 2017; Tian et al., 2023). The AOD and extinction coefficient retrieved from visibility show a similar distribution at global scale, with a correlation coefficient of nearly 0.6 (Mahowald et al., 2007). Similar global (Husar et al., 2000; Wang et al., 2009) and regional (Koelemeijer et al., 2006; Wu et al., 2014; Boers et al., 2015; Zhang et al., 2017; Zhang et al., 2020) spatial distributions have been reported.

AOD loadings exhibit significant seasonal variations worldwide, particularly over land. In this study, a year is divided into four parts: December-January-February (DJF), March-April-May (MAM), June-July-August (JJA), and September-October-November (SON), corresponding to winter (summer), spring (autumn), summer (winter), and autumn (spring) in the NH (SH), respectively. Figure 103 (b-e) also depicts the spatial distribution of seasonal average AOD over land from 1980 to 2021. The global AOD in DJF, MAM, JJA, and SON is ~~0.158±0.06262~~, ~~0.162±0.08175~~, ~~0.175±0.093205~~, and ~~0.153±0.070166~~, respectively. The standard bias of AOD in JJA and ~~MAM DJF~~ are greater than those in DJF and SON. AOD exhibits seasonal changes, with the highest in JJA, followed by MAM, DJF, and SON. ~~From 1980 to 2021, the seasonal AOD in NH is 0.152±0.064 (DJF), 0.161±0.088 (MAM), 0.176±0.090 (JJA), and 0.144±0.060 (SON), and in SH~~

847 is 0.184 ± 0.041 (DJF), 0.166 ± 0.044 (MAM), 0.169 ± 0.072 (JJA), and 0.19 ± 0.060 (SON).–

848 In the NH, the AOD ranking ~~from high to low in season~~ is summer (0.210) > spring (0.176) > autumn
849 (0.163) > winter (0.160) > ~~autumn~~. In ~~SH~~ the SH, the AOD ranking from high to low in season is
850 spring (0.188) > summer (0.184) > autumn (0.164) > winter (0.152) > ~~autumn~~. The highest AOD is
851 observed during JJA in the NH, while ~~in SH~~ in the SH, the peak occurs during SON. The ~~occurrence~~
852 ~~of~~ high AOD values is highly associated with the growth of hygroscopic particle and the
853 photochemical reaction of aerosol precursors under higher relative humidity in Asia (JJA) (Remer
854 et al., 2008) and Europe such as Russia (JJA), and biomass burning in South America (SON),
855 Southern Africa (SON), and Indonesia (SON) (Ivanova et al., 2010; Krylov et al., 2014). On the
856 other hand, the lowest global AOD values are observed during ~~autumn~~ winter, which may be
857 attributed to the atmospheric circulation ~~weakening of monsoon~~ systems (Li et al., 2016; Zhao et al.,
858 2019).

859 ~~In addition to the spatial characteristics of AOD,~~ the temporal variations in AOD have also been
860 of great interest due to the significant relationship between aerosols and climate change. Figure 103
861 (f) shows the ~~temporal~~ trends of annual average AOD (** represents passing the significance test,
862 $p < 0.01$) over the global land, the SH and the NH during 1980-2021. The global land, NH, and SH
863 trends demonstrate decreasing trends of AOD with values of $-0.00296/10a$, $-0.00180030/10a$, and -
864 $0.00590021/10a$, respectively, with all passing the significance test ~~with a confidence level of 95%~~.
865 Notably, the declining trend is much greater in the NSH than in the SNH.

866 ~~It may be related to the decrease in the frequency of sandstorms and wildfires and the increase in~~
867 ~~precipitation, such as in Australia. Two AOD peaks in 1983 and 1994 and two AOD valleys in 1980~~
868 ~~and 1990 are observed before 2000. The two AOD peaks may be attributed to large volcanic~~
869 ~~eruptions, which has been confirmed by previous studies. The volcanic eruptions and their~~
870 ~~associated fires of the El Chichón volcano in Mexico in 1982 (Hirono and Shibata, 1983) and Mount~~
871 ~~Pinatubo in the Philippines in 1991 (Tupper et al., 2005) resulted in elevating global AOD levels in~~
872 ~~the following years. The AOD recovery to the previous low levels after volcanic eruptions takes~~
873 ~~approximately 10 years. This further indicates the efficiency of our data capturing the volcanic~~
874 ~~eruption emission features.~~

875 ~~Due to the influence of geography, atmospheric circulation, population, and emissions, the trend of~~
876 ~~global aerosols varies in different latitude. Figure 14 illustrates the multi year average AOD in~~
877 ~~different latitude ranges for land, the NH, and the SH from 1980 to 2021. Within $[-20, 20^\circ N]$, the~~
878 ~~global average AOD reaches its maximum (0.234), and the maximum AOD NH is 0.256 in $[0, 20^\circ N]$.~~
879 ~~The highest AOD in SH is 0.217 in $[-15, 0^\circ N]$. The average AOD in SH rapidly decreases from~~
880 ~~$15^\circ N$ to $35^\circ N$. In NH, AOD is generally greater than in SH from $5^\circ N$ to $65^\circ N$. When, the latitude~~
881 ~~is greater than $70^\circ N$, the NH's AOD is smaller than the SH's, which may be related to low emission~~
882 ~~intensity and low population density in high latitude areas.~~

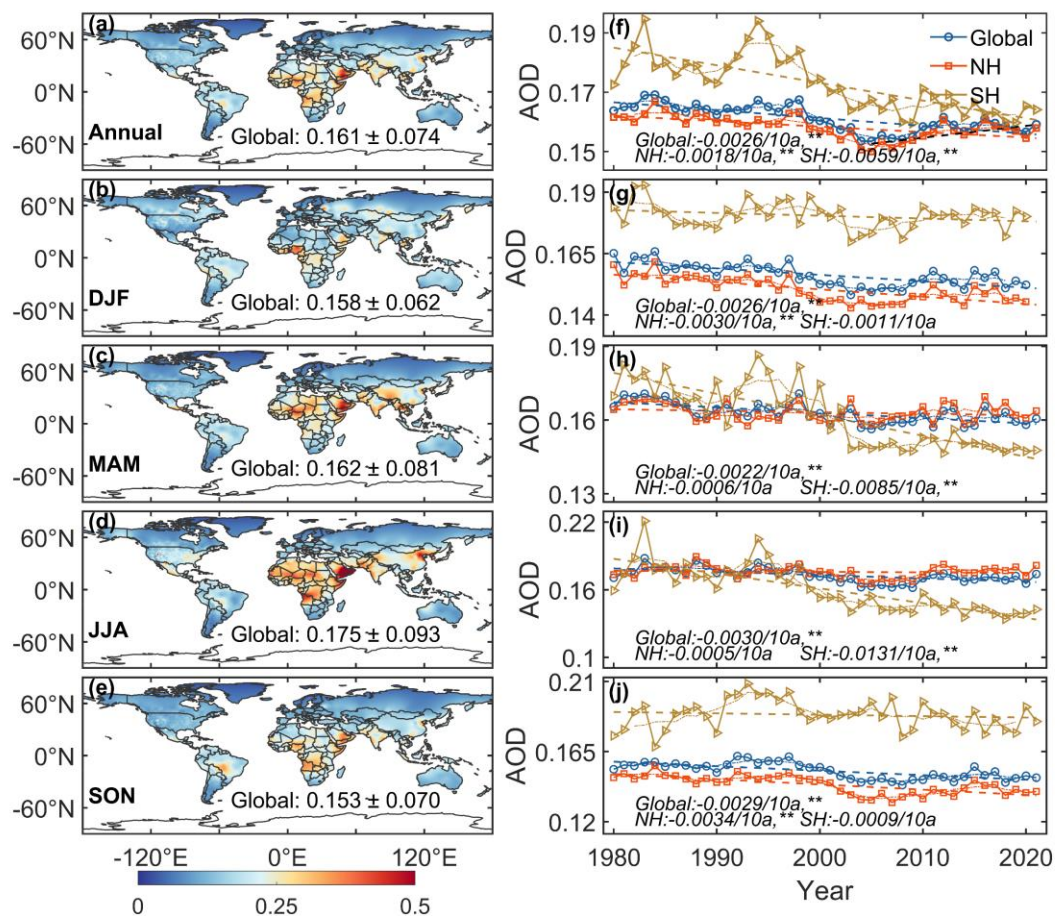
883 The seasonal trends of AOD during 1980-2021 at the global and hemispheric scales are shown in
884 Figure 103 (g-j). The trend over land global AOD shows a is decreasing in DJF, JJA and SON, and
885 increasing in MAM. ~~trend in all seasons (-0.002 – $-0.003/10a$). The largest declining trends are is~~
886 ~~observed in JJA and SON, with decreasing trend values of ($-0.00553/10a$), and $-0.0029/10a$,~~
887 ~~respectively. DJF and MAM follow with decreasing trend values of $-0.0026/10a$ and $-0.0022/10a$,~~
888 ~~respectively, all passing the significance test ($p < 0.01$). For In the NH, the AOD trends in different~~

889 seasons are $-0.004439/10a$ (DJF), $-0.00060016/10a$ (MAM), $-0.002405/10a$ (JJA), and $-0.00634/10a$
 890 (SON). DJF and SON pass the significance test ($p < 0.01$), while MAM and JJA do not. In the SH,
 891 the trends are as follows: $-0.00224/10a$ (DJF), $-0.00850044/10a$ (MAM), $-0.013400064/10a$ (JJA),
 892 and $-0.00090.0033/10a$ (SON). Interestingly, in contrast to the NH, MAM and JJA pass the
 893 significance test, while DJF and SON do not. The largest declining season trend in the NH is
 894 winter/autumn in the NH and JJA in the SH, while in the SH, it is summer. However, the trends are
 895 positive in MAM of the NH and DJF and SON of the SH.

896 The decreasing trend in the SH is more than four times greater than that in the NH, particularly
 897 before the year 2000. While both the global and SH AOD exhibit a decreasing trend since 2005, the
 898 NH has shown a significant increase in winter AOD, leading to an overall increasing trend.
 899 Moreover, the NH shows an increasing trend of $0.004/10a$ from 2005 to 2021.

900 Annual SO_2 emissions increased from 9.4 to 15.3 TgS from 2000 to 2005, which ultimately ended
 901 up as sulfate aerosols, leading to a significant increase in sulfate aerosols (Hofmann et al., 2009).
 902 More relevantly, the frequent volcanic eruptions in tropical regions from 2002 to 2006, combined
 903 with seasonal circulation patterns during winter, led to the transport of aerosol particles to higher
 904 latitudes (Hofmann et al., 2009; Vernier et al., 2011; Sawamura et al., 2012; Andersson et al., 2015).

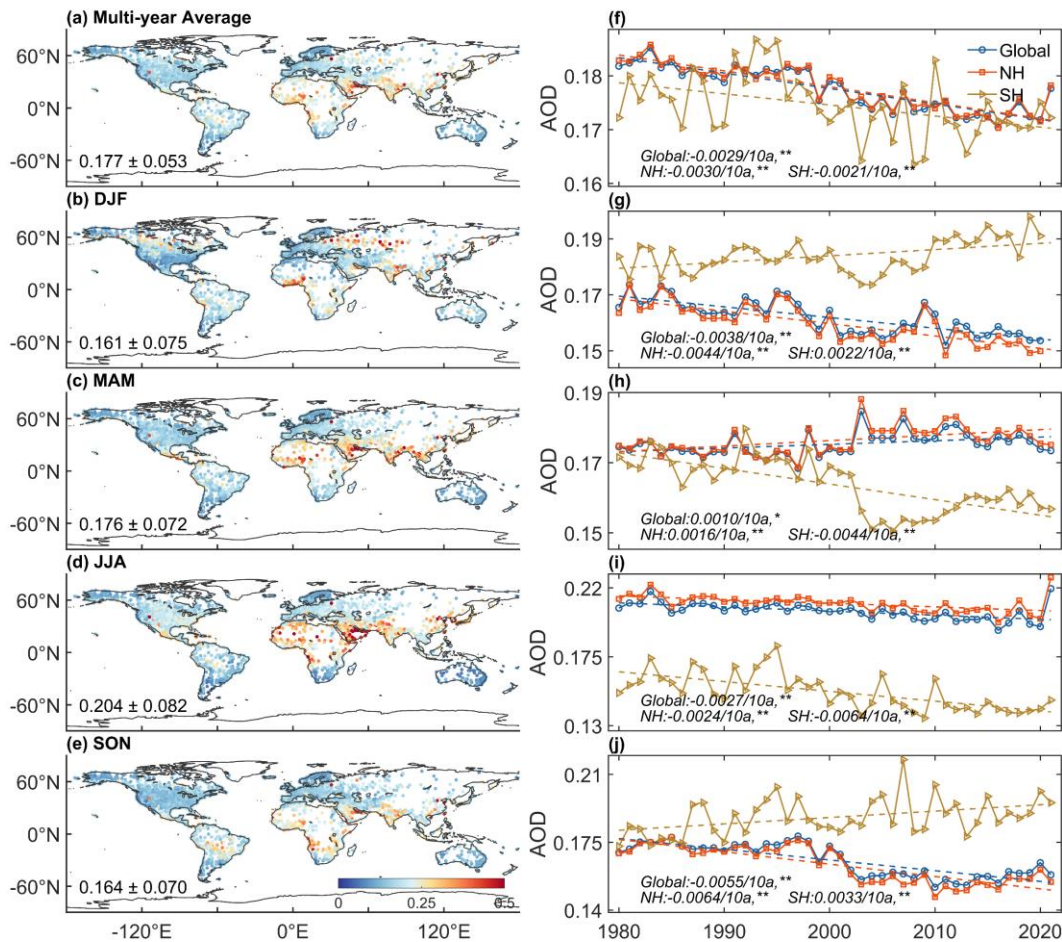
905



906

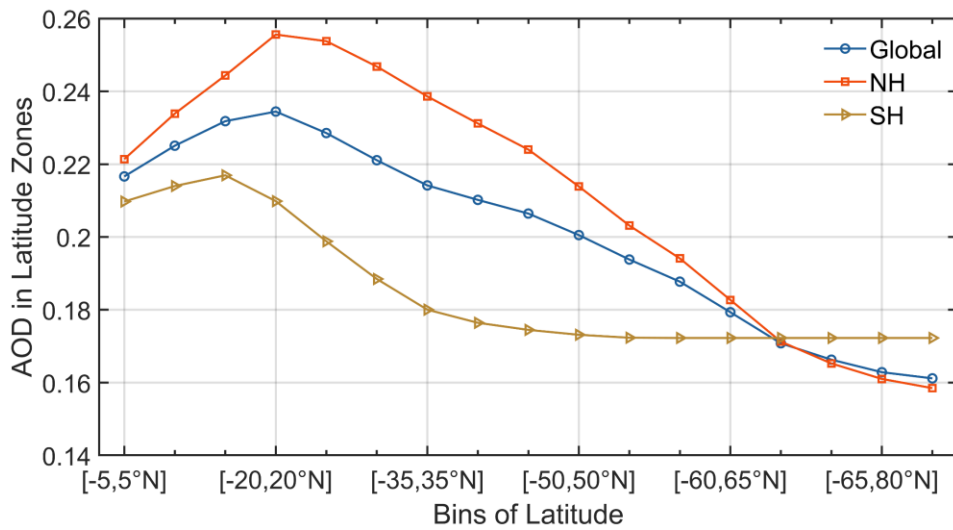
907 Figure 13: The multi-year averages of VIS AOD from 1980 to 2021. Global land (circle),
 908 northern hemisphere (NH, 0-85°N) (triangle) and southern hemisphere (SH, 0-60°S) (square)

909 **annual and seasonal AOD. The symbol, **, represents that the test passed at a significance**
 910 **level of 0.01. DJF represents December and next January and February. MAM represents**
 911 **March, April, and May. JJA represents June, July, and August. SON represents September,**
 912 **October, and November.**

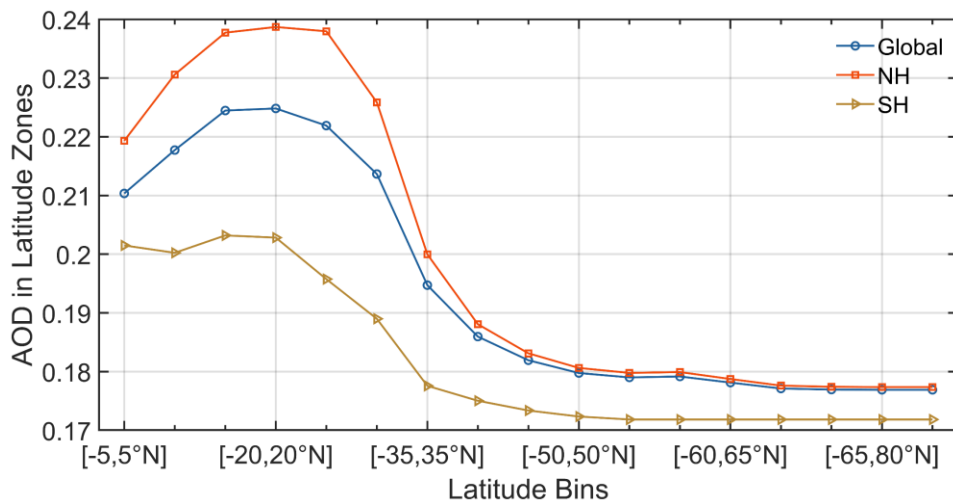


913
 914 **Figure 10: The multi-year and average seasonal AOD and from 1980 to 2021. Global land (circle),**
 915 **northern hemisphere (NH) (triangle) and southern hemisphere (SH) (square) annual and seasonal**
 916 **AOD. The symbol, **, represents that the test passed at a significance level of 0.01. The symbol, *,**
 917 **represents that the test passed at a significance level of 0.05. DJF represents December and next**
 918 **January and February. MAM represents March, April, and May. JJA represents June, July, and**
 919 **August. SON represents September, October, and November.**

920



921



922

923 **Figure 114:** The global land (blue), northern hemisphere's (red) and southern hemisphere's (yellow)
 924 multi-year average VIS_AOD from 1980 to 2021 in different latitude zones. The latitude range is
 925 from -65 to 85°N, with a bin of 5°.

926 **3.56 Interannual variability and trend of visibility-derived AOD over regions**

927 The distribution of AOD over global land exhibits significant spatial heterogeneity. Large variations
 928 in aerosol concentrations exist among different regions, leading to a non-uniform spatial distribution
 929 of AOD globally. Accurately assessing the long-term trends of aerosol loading is a key for
 930 quantifying aerosol climate change, and it is crucial for evaluating the effectiveness of
 931 measurements implemented to improve regional air quality and reduce anthropogenic aerosol
 932 emissions. Therefore,

933 To analyze the spatiotemporal characteristics and trends of AOD in different regions, we selected
 934 12 representative regions to analyze the variability and trend of AOD, which are influenced by
 935 various aerosol sources (Wang et al., 2009; Hsu et al., 2012; Chin et al., 2014), such as desert,
 936 industry, anthropogenic emissions, and biomass burning emissions, which nearly cover the most
 937 land and are densely populated regions (Kummu et al., 2016). These representative regions are

938 Eastern Europe, Western Europe, Western North America, Eastern North America, Central South
939 America, Western Africa, Southern Africa, Australia, Southeast Asia, Northeast Asia, Eastern China,
940 and India, as shown in Figure 1.

941 The multi-year average and seasonal average AOD (Figure 12), the trends of the annual average of
942 monthly anomalies (Figure 13), and the seasonal trends (Figure 14) are analyzed in 12 regions from
943 1980 to 2021.

944 ~~We use multi-year average and seasonal average AOD to evaluate aerosol loadings (Figure 15), the~~
945 ~~annual average of monthly anomalies to analyze interannual trends (Figure 16), and the seasonal~~
946 ~~average to analyze seasonal trends (Figure 17) in 12 regions from 1980 to 2021.~~

947 ~~We can see some differences between VIS_AOD and MODIS AOD. In addition to model errors,~~
948 ~~the spatial matching between meteorological stations and MODIS, terrain, surface coverage, and~~
949 ~~station altitude will also bring errors. When particle transport and photochemical reactions occur~~
950 ~~above the boundary layer, visibility cannot capture the feature, which will also increase the~~
951 ~~uncertainty. However, bias is inevitable and can only be kept as small as possible. From the trend,~~
952 ~~they have similar changing characteristics, especially on monthly and yearly scales.~~

953 ~~Figure 15 shows the regions with~~ The regions with a high AOD aerosol level from 1980 to 2021
954 ~~(multi-year average AOD > 0.2) are in West Africa, Southeast and~~ Southeast and ~~Northeast Asia, Eastern China,~~
955 ~~and India. The AOD values range from 0.15 to 0.2 in Eastern Europe, Western Europe, Eastern~~
956 ~~North America, Central South America, and South Africa, and Southeast Asia range from 0.15 to~~
957 ~~0.2. The AOD values are less than 0.15 in Eastern Europe, Western Europe, Western North America,~~
958 ~~and Australia are less than 0.15.~~

959 Europe is an industrial region with a low aerosol loading region, and the multi-year average AOD
960 in Eastern Europe (0.144 ± 0.00781) is higher than that in Western Europe (0.139 ± 0.003163) during
961 1980-2021. Eastern Europe shows a greater downward trend in AOD ($-0.00410067/10a$) compared
962 to Western Europe ($-0.00210026/10a$). The highest AOD is observed in JJA, the dry period when
963 solar irradiation and boundary layer height increase, with Eastern Europe at 0.161 ± 0.201 and Western
964 Europe at 0.162, which could be due to increases in secondary aerosols, biomass burning, and dust
965 transport from the Sahara (Mehta et al., 2016). However, there are seasonal variations. In Eastern
966 Europe, the seasonal AOD ranking from high to low is JJA (0.161 ± 0.201) > DJF (0.147 ± 0.181) > MAM
967 (0.175 ± 0.38) > SON (0.161 ± 0.34), while in Western Europe, it is JJA (0.193 ± 0.62) > MAM (0.162 ± 0.40) > SON
968 (0.160 ± 0.36) > DJF (0.138 ± 0.47). The differences among seasons are larger in Western Europe. AOD in
969 Eastern Europe shows declining trends ($p < 0.01$) in all seasons, ~~while it does not pass the~~
970 ~~significance test in MAM. Among four seasons, and SON has the largest declining trend is in DJF~~
971 ~~of AOD~~ ($-0.009658/10a$). In Western Europe, ~~the trend in DJF, JJA, and SON exhibit declining~~
972 ~~trends, while the trend in MAM of AOD that pass the significance test, while the MAM shows a~~
973 ~~significant increase trend of AOD~~ ($-0.001922/10a$), ~~which may be due to eruptions of the~~
974 ~~Eyjafjallajökull volcano in Iceland in spring 2010 (Karbowska and Zembrzuski, 2016). The trends~~
975 ~~in both Western and Eastern Europe experienced arc increasing trends in MAM in AOD during~~
976 ~~from 1995 to 2005 the period of 1995-2005, with Western Europe showing a greater increase.~~
977 However, after 2005, the decline rates accelerated in both regions each season. Studies have shown
978 ~~T~~ the downward trend in Europe is attributed to the reduction of biomass burning, anthropogenic

979 aerosols, and aerosol precursors (such as sulfur dioxide)(Wang et al., 2009; Chin et al., 2014;
980 Mortier et al., 2020).

981 North America is also an industrial region with a low aerosol loading. The average AOD values ~~for~~
982 in Eastern and Western North America during 1980-2021 are 0.153 ± 0.00465 and 0.131 ± 0.00546 ,
983 respectively, with the Eastern region being higher than the Western region by 0.01922 . From 1980
984 to 2021, both Eastern ($-0.00274/10a$) and Western North America ($-0.001709/10a$) show a
985 downward trend; ~~however, the decline in the Western region is not statistically significant. And the~~
986 ~~trend is $-0.0172/10a$ from 1995 to 2005 and $0.0096/10a$ from 2005 to 2021.~~ The average AOD values
987 in DJF, MAM, JJA, and SON in Western North America are 0.141367 , 0.1286148 , 0.1457163 , and
988 0.114130 , respectively, compared to 0.1387 , 0.15645 , 0.1913216 , and 0.138149 in Eastern North
989 America. ~~The lowest AOD values of 12 regions during DJF and SON are observed in Western North~~
990 ~~America (Remer et al., 2008).~~ Specifically, ~~the trends in of~~ the Western and Eastern region are ;
991 ~~there is a consistent~~ increasing ~~trend~~ during MAM ($0.004/10a$) ~~from 1980 to 2021~~ and decreasing
992 during other seasons; ~~while JJA and SON also show an increase after 2000, except for DJF ($-$~~
993 ~~$0.0032/10a$).~~ In contrast, the AOD trends in the Eastern region remain unchanged during the period
994 1980-2021, except for MAM, which shows a stable increasing trend ($0.0033/10a$), while DJF, JJA,
995 and SON exhibit decreasing trends ($-0.0023/10a$, $-0.0040/10a$, $-0.0053/10a$, respectively). In the
996 Western region, the annual mean AOD started to trend is increasing after 2005, while in the Eastern
997 region, there is no the increasing trend was not significant. The upward-increasing trend may be
998 due to low rainfall and increased wildfire activities (Yoon et al., 2014). The decrease in AOD in
999 Eastern North America is related to the reduction of sulfate and organic aerosols, as well as the
1000 decrease in anthropogenic emissions caused by environmental regulations (Mehta et al., 2016).

1001 Central South America is a relatively high aerosol loading region, sourced from biomass burning,
1002 especially in SON (Remer et al., 2008; Mehta et al., 2016), with a multi-year average AOD of
1003 0.192 ± 0.0178 . There is a clear downward trend ($-0.01000075/10a$) from 1980 to 2021; which The
1004 trend is slightly greater-lower than the trend ($-0.0090/10a$) from 1998 to 2010 (Hsu et al., 2012) and
1005 AOD-the trend is decreasing ed from 1980 to 2006 (Streets et al., 2009) and from 2001 to 2014
1006 (Mehta et al., 2016). ~~Although The AOD values in~~ DJF (0.199207) and SON (0.2286) have-are
1007 higher values compared to the values in MAM (0.1859) and JJA (0.17163), and the larger declining
1008 trends are observed in MAM ($-0.010026/10a$) and JJA ($-0.015067/10a$). ~~It The result~~ indicates that
1009 although AOD has decreased overall, the aerosol loading is still high, which is caused by seasonal
1010 deforestation and biomass combustion-burning is still large(Mehta et al., 2016).

1011 Africa is ~~also one of the regions with~~ a high aerosol loading region worldwide. In West Africa, the
1012 multi-year average AOD is 0.275 ± 0.01281 during 1980-2021, and the trend is decreasing annual
1013 AOD shows a downward trend ($-0.00080062/10a$, $p > 0.05$). The world's largest desert (Sahara
1014 Desert) is in West Africa, with much dust aerosol discharged. The AOD values in JJA (0.296), MAM
1015 (0.292), DJF (0.276) and SON (0.261) all seasons are above 0.265 , with JJA (0.301) and MAM
1016 (0.300) reaching 0.3, and DJF and SON being 0.252 and 0.250, respectively. The trends AOD in
1017 DJF ($-0.01435/10a$, $p < 0.04$), MAM ($-0.0015/10a$), JJA ($-0.0019/10a$) and SON ($-0.00260078/10$;
1018 $p > 0.05$) exhibit are decreasing. trends, while JJA ($0.0088/10a$, $p < 0.01$) and MAM ($0.0037/10a$,
1019 $p > 0.05$) show an opposite trend. ~~For South Africa, t~~The multi-year average AOD in South Africa is
1020 0.18277 ± 0.020 , lower than that of West Africa. The trend is annual mean AOD in South Africa shows
1021 a significant decreasing ($-0.00960016/10a$). The results of AERONET observations and

1022 ~~simulation results also show a decreasing trend of AOD (Chin et al., 2014). The AOD values range~~
1023 ~~from 0.12 to 0.20 during 2000-2009, dominated by fine particle matter from industrial pollution~~
1024 ~~from biomass and fossil fuel combustion (Hersey et al., 2015). The average AOD values in DJF,~~
1025 ~~MAM, JJA, and SON are 0.189207, 0.162173, 0.147135, and 0.210, with trends of 0.0044/10a, -~~
1026 ~~0.0089/10a, -0.0089/10a and 0.0063/10a, respectively. JJA (-0.0268/10a, p<0.01), MAM (-~~
1027 ~~0.0126/10a, p<0.01) and SON (-0.0001/10a, p>0.05) exhibit a downward AOD trend, while DJF~~
1028 ~~(0.0006/10a, p>0.05) shows an upward trend. AERONET and simulation results also show a~~
1029 ~~decreasing trend of AOD (Chin et al., 2014).~~

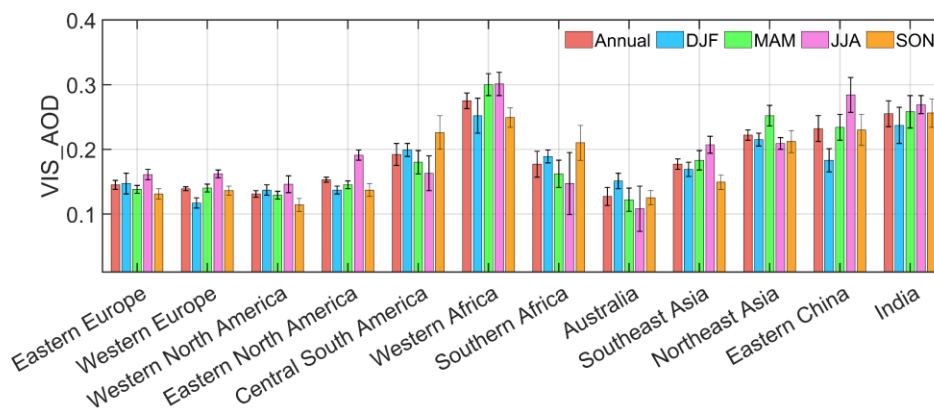
1030 Australia is a region with a low aerosol loading. The multi-year ~~mean-average~~ AOD is
1031 ~~0.127±0.01433~~ during 1980-2021. The AOD ranges from 0.05 to 0.15 from AERONET during
1032 2000-2021, and dust and biomass burning are important contributors to the aerosol loading (Yang
1033 et al., 2021a). There is a downward trend of AOD (~~-0.00810028/10a, p<0.01~~), which may be related
1034 to a decrease in dust and biomass burning (Yoon et al., 2016; Yang et al., 2021a). In addition, ~~a~~
1035 research has shown that the forest area in Australia has increased sharply since 2000 (Giglio et al.,
1036 2013), surpassing the forest fire area of the past 14 years. The seasonal average of AOD in MAM,
1037 JJA, SON, and DJF are ~~0.122130, 0.1078, 0.125132, and 0.151161~~. The AOD in JJA is the lowest
1038 ~~among-in~~ all seasons and ~~in all~~ regions. The ~~trends in DJF and SON are increasing, and the trends~~
1039 ~~in MAM and JJA are decreasing~~ highest AOD is in DJF with an increasing trend (0.0056/10a,
1040 ~~p<0.01~~), while the trends during MAM, JJA and SON are ~~0.0096/10a (p<0.01), 0.0231/10a~~
1041 ~~(p<0.01) and 0.0042/10a (p<0.01), respectively~~. Ground-based observations and satellite retrievals
1042 indicate that wildfires, biomass burning and sandstorms lead to high AOD in DJF and SON. The
1043 low AOD of MAM and JJA is due to a decrease in the frequency of sandstorms and wildfires and
1044 an increase in precipitation (Gras et al., 1999; Yang et al., 2021a; Yang et al., 2021b).

1045 Asia is also a high aerosol loading area with various sources. In Southeast Asia, the multi-year
1046 average AOD is ~~0.177-222~~ during 1980-2021 with a downward trend of AOD (~~-0.00073/10a,~~
1047 ~~p>0.05~~). It is also a biomass-burning area. The seasonal average AOD ranking ~~from high to low~~ is
1048 ~~JJA-MAM (0.251207) > MAM-DJF (0.183216) > DJF-SON (0.169212) > SON-JJA (0.149209)~~. The
1049 trends in DJF (~~-0.001835/10a, p<0.05~~) is decreasing and the trends in ~~MAM (0.033/10a), JJA (-~~
1050 ~~0.00087/10a, p>0.05) and SON (-0.00210006/10a, p>0.05) are opposite-increasing. However, the~~
1051 ~~trends are not significant. to MAM (0.0050/10a, p<0.01)~~. Southeast Asia has no clear long-term
1052 trend in estimated AOD or ~~ground-based observations~~ ~~observed surface solar radiation~~ (Streets et al.,
1053 2009). In Northeast Asia, the multi-year average AOD is ~~0.222-244~~ during 1980-2021, ~~with a trend~~
1054 ~~of -0.0009/10a, with no significant temporal trend. The trend is increasing (0.0018/10a) during~~
1055 ~~1980-2014 and decreasing (-0.0213/10a) during 2014-2021~~. The seasonal AOD values are ~~0.196 in~~
1056 ~~DJF, 0.252-260 in MAM, 0.215 in DJF, 0.212-287 in SON-JJA and 0.209-236 in JJASON. The high~~
1057 ~~aerosol level is AOD in MAM is significantly higher than other seasons, which may be related to~~
1058 ~~sandstorms-dust aerosol and aerosol transportation in East Asia, and the reason for the high AOD in~~
1059 ~~winter may be related to the transportation~~. The trends of AOD in DJF (~~-0.00250.0016/10a, p>0.05~~),
1060 MAM (~~0.00310062/10a, p>0.05~~) are increasing, and the trends in JJA (~~-0.0043/10a~~) and SON (~~-~~
1061 ~~0.007006/10a, p>0.05) are not significant decreasing~~. In Eastern China, the multi-year average AOD
1062 is ~~0.233241~~, with an increasing trend (~~0.00710130/10a, p<0.01~~). The trend is ~~0.01510196/10a~~ from
1063 1980 to ~~2006-2014~~ and ~~-0.04690572/10a~~ from ~~2006-2014~~ to 2021. The seasonal average AOD
1064 ranking from high to low is JJA (0.2874), MAM (0.232494), SON (0.230236) and DJF (0.183216).

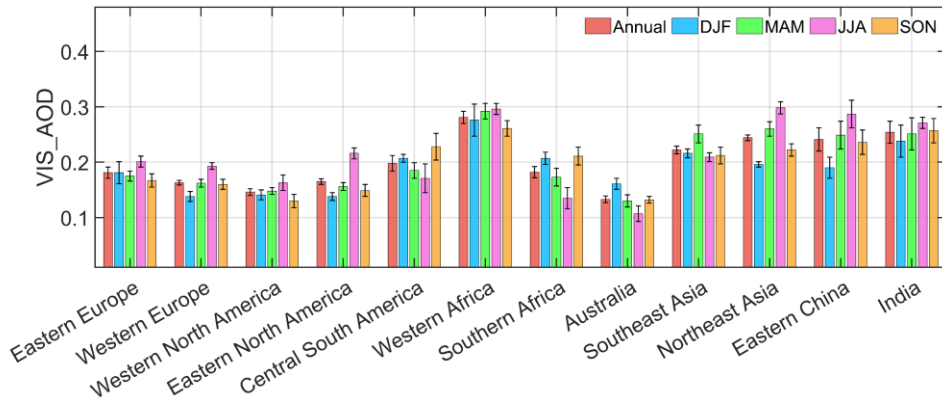
1065 The AOD trends in DJF ($0.00930133/10a$, $p < 0.01$), MAM ($0.00920179/10a$, $p < 0.01$), JJA
 1066 ($0.00380107/10a$, $p > 0.05$) and SON ($0.00650105/10a$, $p < 0.05$) are all positive ~~but the trend in JJA~~
 1067 ~~does not pass the significance test. We can see that there are three stages of changes in AOD~~
 1068 ~~the trend can be divided into three stages:~~ 1980-2005, 2006-2013 and 2014-2021. In the first stage,
 1069 AOD ~~values are increased~~ increasing steadily. In the second stage, AOD ~~values~~ maintained a high
 1070 ~~level~~ larger positive anomaly accompanied by oscillations. In ~~t~~the third stage, the AOD values
 1071 experienced a rapid decline, reaching the level ~~of in the~~ 1980s by 2021. The increasing trend of
 1072 AOD before 2006 may be due to the significant increase in industrial activity, and after 2013, the
 1073 significant decrease is closely related to the implementation of air quality-related laws and
 1074 regulations, along with adjustments in the energy structure (Hu et al., 2018; Cherian and Quaas,
 1075 2020).

1076 India is a high aerosol loading area. The multi-year average AOD is 0.2545, with ~~an a upward~~
 1077 ~~decreasing~~ trend ($0.00960119/10a$, $p < 0.01$) from 1980 to 2021. Dust and biomass burning has an
 1078 influence on AOD level. There are three stages: 1980-1997 ($0.00320050/10a$, $p < 0.01$), 1997-2005
 1079 ($-0.04200393/10a$, $p < 0.01$), 2005-2021 ($0.04810446/10a$, $p < 0.01$). ~~Although the trend is downward~~
 1080 ~~in the second stage, the larger positive trend is in the third stage.~~ The seasonal average AOD values
 1081 are 0.237-238 in DJF, 0.258-251 in MAM, 0.269-271 in JJA, and 0.256-257 in SON. The largest
 1082 AOD is in JJA. In winter and autumn, ~~it the aerosol level is~~ affected by biomass burning, and in
 1083 spring and summer, it is also affected by dust, transported from the Sahara under during the monsoon
 1084 period (Remer et al., 2008). The trends in DJF ($0.01520186/10a$, $p < 0.01$), MAM ($0.00910143/10a$,
 1085 $p < 0.01$), JJA ($0.00250012/10a$, $p > 0.05$), and SON ($0.01070129/10a$, $p < 0.05$) are positive. ~~There~~
 1086 ~~largest trend is in winter.~~

1087 The above results have supplemented the long-term AOD variability and trend over land. To
 1088 ~~summarize,~~ The AOD level at regional scale there are is significant differences in the spatial
 1089 ~~distribution, annual trends, and seasonal trends of AOD across different regions~~ from 1980 to 2021,
 1090 which is significantly related to the aerosol emission source type, transportation and the
 1091 implementation of laws and regulations about pollution control. ~~The high aerosol loadings from~~
 1092 ~~1980 to 2021 are in West Africa, India and Asia, and low aerosol loading regions are in Europe,~~
 1093 ~~Western North America, and Australia. Eastern China and India show an increasing trend, Southeast~~
 1094 ~~Asia and Northeast Asia show no significant trend, and the other regions show downward trends.~~
 1095 ~~However, not all regional seasonal trends are consistent with their annual trends. The results in this~~
 1096 ~~study have supplemented the long-term trend and distribution of AOD over land.~~



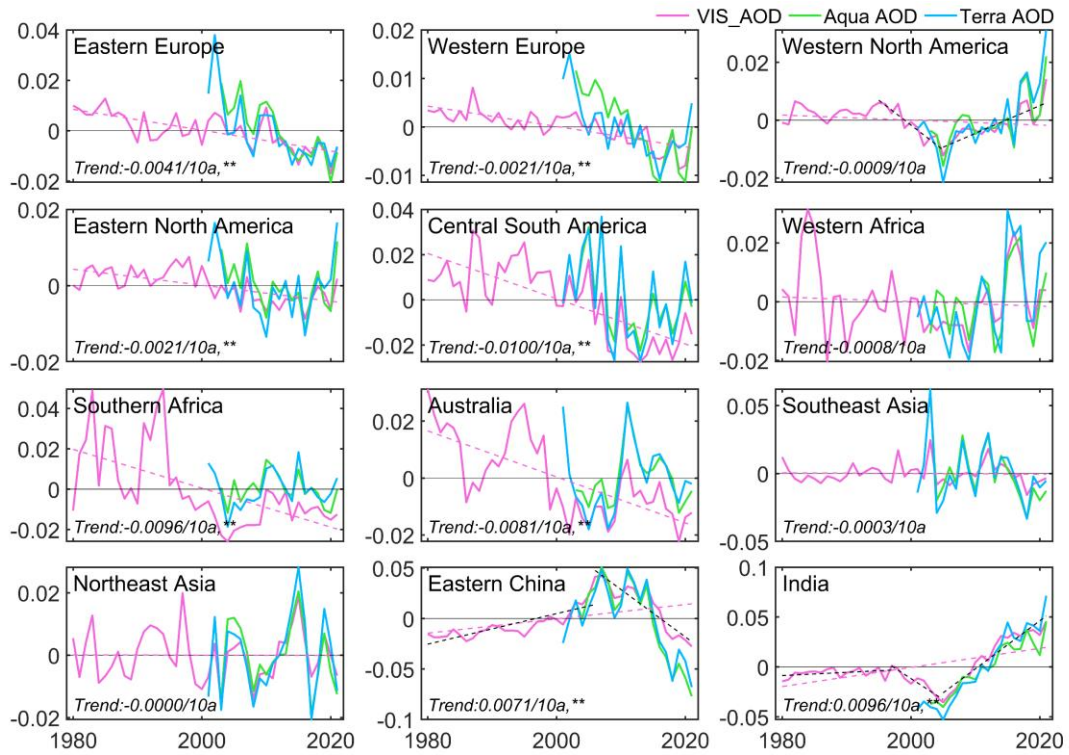
1097



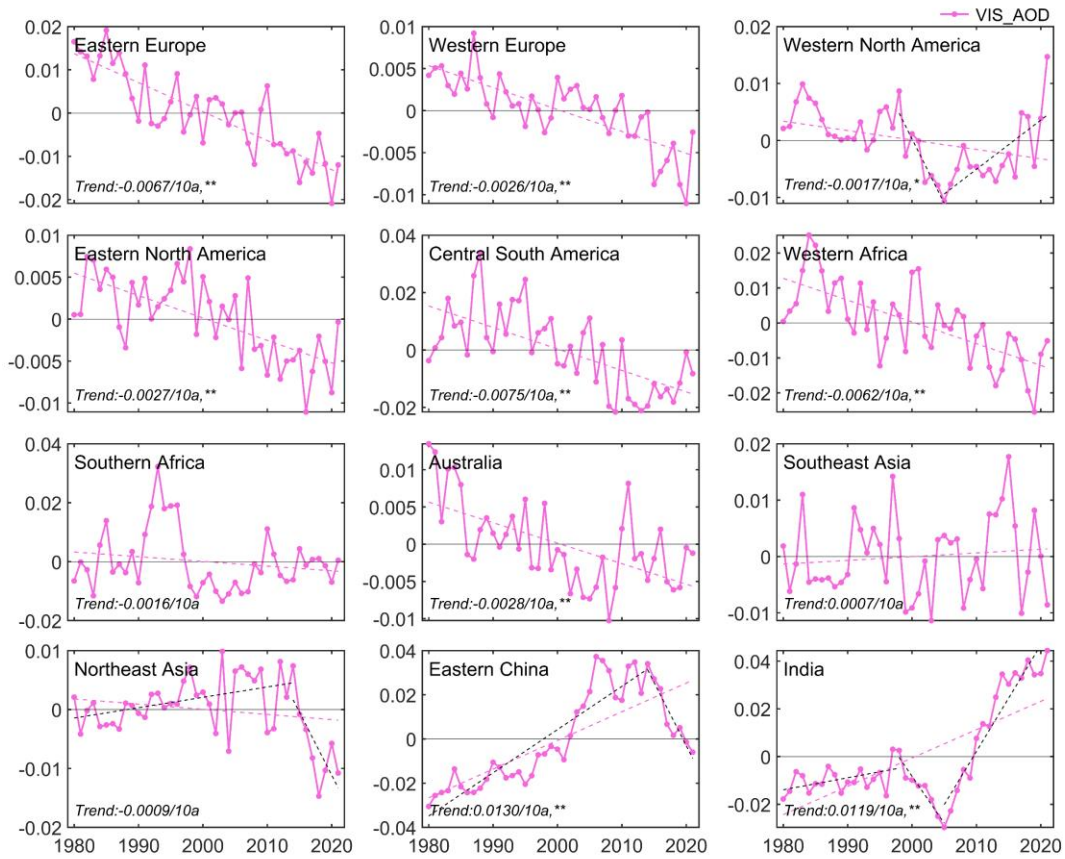
1098

1099 **Figure 125:** Annual and seasonal averages of AOD in 12 regions (Eastern Europe, Western Europe,
 1100 Western North America, Eastern North America, Central South America, Western Africa, Southern
 1101 Africa, Australia, Southeast Asia, Northeast Asia, Eastern China, and India) during 1980-2021.

1102



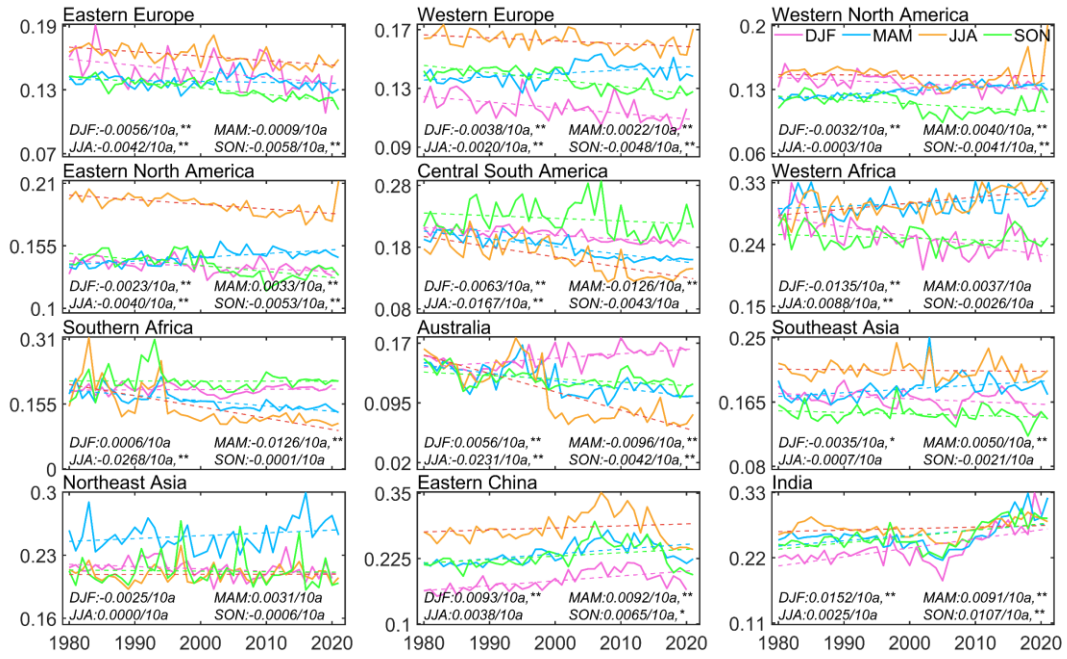
1103



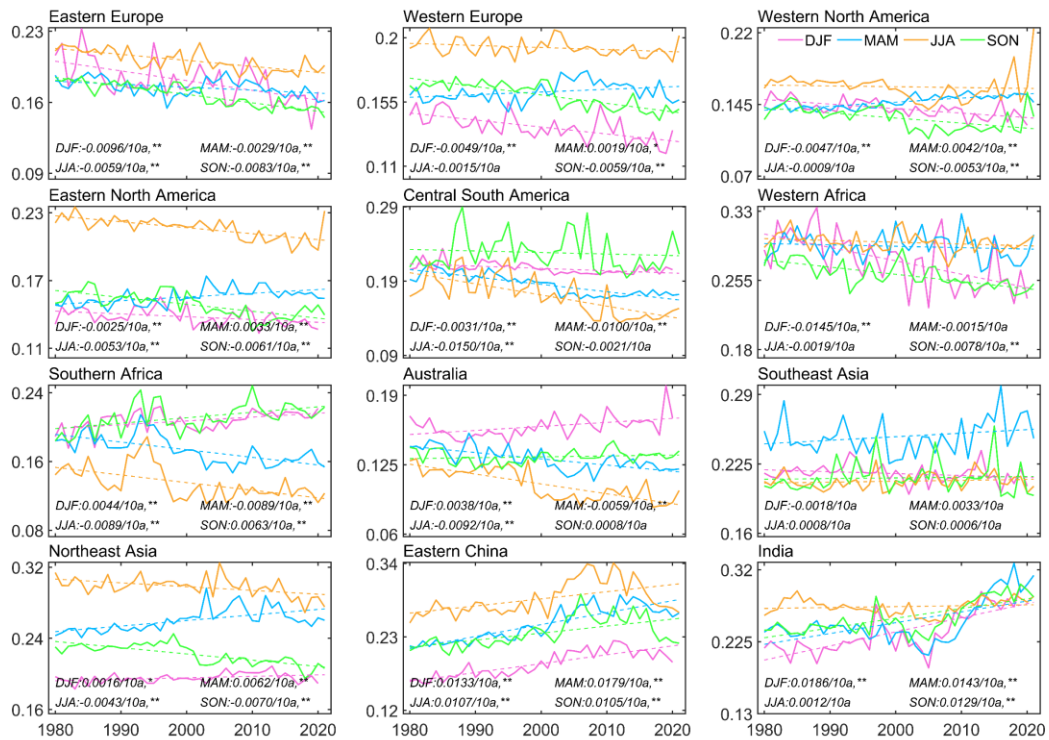
1104

1105 **Figure 136:** Annual averages of monthly VIS_AOD anomaly ~~gridded~~ VIS_AOD from 1980 to 2021
 1106 (pink line), Aqua (green line), and Terra (blue line) MODIS AOD in 12 regions (Eastern Europe,
 1107 Western Europe, Western North America, Eastern North America, Central South America, Western
 1108 Africa, Southern Africa, Australia, Southeast Asia, Northeast Asia, Eastern China, and India). The
 1109 dotted line is the trend line.

1110



1111



1112

1113 **Figure 147:** Seasonal average VIS AOD s of gridded VIS AOD during from 1980 to 2021 in 12
 1114 regions (Eastern Europe, Western Europe, Western North America, Eastern North America, Central
 1115 South America, Western Africa, Southern Africa, Australia, Southeast Asia, Northeast Asia, Eastern
 1116 China, and India). The dotted line is the trend line.

1117 **4 Data availability**

1118 We provide ~~the~~ daily visibility-derived AOD ~~_data~~ at 5032 stations from 1959 to 2021 ~~and grid~~
1119 scales ~~_~~ over global land, which is are available at National Tibetan Plateau / Third Pole
1120 Environment Data Center, ~~–~~<https://doi.org/10.11888/Atmos.tpd.300822> (Hao et al., 2023).

1121 ~~We provide the station-scale AOD from 1959 to 2021.~~ Due to a small number and sparse
1122 ~~meteorological-visibility~~ stations prior to 1980, ~~we only provide the gridded AOD from 1980 to~~
1123 ~~2021. In order to keep consistency in time scale, the global/regional analysis the time range we~~
1124 ~~describe~~ in this study is from 1980 to 2021. The following is a description to the ~~station and gridded~~
1125 ~~VIS_~~AOD dataset.

1126 The station-scale AOD files are in ‘Station_Daily_AOD_1959_2021.zip’. The station-scale AOD
1127 files can be directly opened by a text program (such as Notepad). The details station information is
1128 in the file of ‘0A0A-Station_ In Information.txt’. There are eight columns in each text file, separated
1129 by commas and the column names are Datetime, TEMP (°C), DEW (°C), RH (%), WS (m/s), SLP
1130 (hPa), DRYVIS (km), and VIS_AOD (550nm). The first column name is the date. The column name,
1131 ‘VIS_AOD (550nm)’, is the AOD at 550nm. The 2-7th column names are temperature (unit: °C),
1132 dew temperature (unit: °C), relative humidity (unit: %), wind speed (unit: m/s), sea level pressure
1133 (unit: hPa), and dry visibility (unit: km).

1134 ~~The gridded AOD is in the file of ‘Gridded_Monthly_AOD_1980_2021.ne’ with a NETCDF4~~
1135 ~~format. There are three variables: ‘VIS_AOD’ (AOD derived from visibility), ‘W95CI’ (the width~~
1136 ~~of the 95% confidence interval), and ‘QA_FLAG’ (quality flag for VIS_AOD). We classify the~~
1137 ~~quality of VIS_AOD into three levels based on ‘W95CI’: (1) High quality (QA_FLAG=1);~~
1138 ~~W95CI<=0.03; (2) Medium quality (QA_FLAG=2), 0.03<W95CI<=0.06; and Low quality~~
1139 ~~(QA_FLAG=3), W95CI>0.06.~~ The more details are in ‘0A0B-ReadMe.txt’.

1140 5 Conclusions

1141 In this study, we employ a machine learning ~~technique-method~~ to derive daily AOD at 550nm from
1142 1959 to 2021 for at 5032 over 5000 land stations worldwide, based on ~~satellite data,~~ visibility,
1143 satellite retrieval, ~~–~~ and related meteorological variables. In the model, The target is Aqua MODIS
1144 AOD (550nm) is set as the target and visibility and related meteorological variables are set as the
1145 predictor. Monthly AOD is interpolated into a 0.5° grid using ordinary kriging with area weighting.
1146 The ~~accuracy and performance~~ and predictive ability of the ~~derived AOD model~~ are ~~assessed~~
1147 evaluated and validated against ~~Terra MODIS AOD as well as~~ AERONET ground-based
1148 observations, Terra MODIS AOD and MRRRA-2 AOD. ~~The gridded AOD is evaluated by Aqua~~
1149 ~~and Terra MODIS AOD and a 95% confidence interval is calculated.~~ We ~~obtain~~ provide a daily
1150 long-term daily AOD (550nm) dataset at 5032 global land stations from ~~1980-1959~~ to 2021, as well
1151 as monthly gridded AOD. The two ~~The~~ datasets has ~~complemented~~ the shortcomings of AOD data
1152 in terms of time scale and spatial coverage over land. Finally, the variability and trend
1153 spatiotemporal variation in of AOD is are analyzed ~~for at~~ global land, ~~the Southern Hemisphere, the~~
1154 ~~Northern Hemisphere, and 12 and~~ regional scales in the past 42 years. Several key findings have
1155 been given in this study as follows.

1156 ~~1. Modeling and gridding evaluation.~~ For all stations, the mean RMSE, MAE, and R of ~~all~~
1157 ~~stations~~ the model are 0.078, 0.044, and 0.750, respectively. The RMSE of 93% stations is less than

0.110, the MAE of 91% is less than 0.060, and the R of 88% is greater than 0.70, respectively. Compared to Aqua and Terra, the average biases of gridded AOD are 3.3% and 1.9%, and the spatial correlation coefficients are 0.80 and 0.79, with the zonal correlation coefficients of 0.99 and 0.99 and the meridional correlation coefficients of 0.99 and 0.90.

2-Model validation. For the daily scale, the R, RMSE and MAE of between VIS_AOD and Aqua AOD is 0.799, 0.079 and 0.044, respectively. The percentage of sample point falling within the EE envelopes is 84.12%. The R between VIS_AOD and Terra AOD is 0.542, with a RMSE of 0.125 and MAE of 0.078. The percentage falling within the EE envelopes is 64.76%. The R between VIS_AOD and AERONET AOD is 0.546, with a RMSE of 0.186 and MAE of 0.099. The percentage falling within the EE envelopes is 57.87%. For the monthly and annual scales, RMSE and MAE show a significant decrease between VIS_AOD and Aqua, Terra, and AERONET AOD, and R and percentages falling within EE show a significant increase. Compared to AERONET AOD and MERRA-2 AOD prior to 2000, the model has consistent predictive ability.

3-Error analysis. As the AOD value increases, the average bias increases. When the pollution level is low (AOD <0.1), the average bias is 0.015 (AOD <0.1), with 83% of data within the EE envelopes. As pollution level increases, the negative mean-average bias becomes significant and the underestimation increases. The elevation of AERONET's site also causes a bias. In low elevation (<=0.5km), in high elevation. There is a negative bias in the low elevation (<=0.5km) with a percentage of 60%-64% falling within the EE envelopes, and a positive bias in high elevation (0.5-1.2km), there is a positive bias, with a percentage of 50%-65% falling within the EE envelopes. The elevation of AERONET's site caused a bias in high elevation. When the elevation difference is negative (the elevation of the meteorological station is lower than that of the AERONET site), there is a significant positive bias. When the difference is positive, the mean bias approaches 0 or is positive. The influence of distance between the meteorological station and AERONET site on bias does not change is not significantly with increasing distance between the meteorological station and AERONET site.

4-Global land AOD. The global, NH, and SH AOD values from 1980 to 2021 are 0.161 ± 0.074 over land, 0.178 in the NH and 0.174 in the SH, 0.158 ± 0.076 , and 0.173 ± 0.059 , with a trend of -0.0029/10a, 0.0030/10a and -0.0021/10a, respectively. Trends in AOD for the global, NH, and SH demonstrate a decreasing trend of -0.0026/10a, -0.0018/10a, and -0.0059/10a, respectively ($p < 0.01$). The seasonal AOD rankings from high to low is JJA (0.204) > MAM (0.176) > DJFSON (0.164) > SONDJF (0.161) over global the global-land, and JJA (0.210) > MAM (0.176) > SON (0.163) > DJF (0.160) in the NH, while in the SH, SON (0.188) > DJF (0.184) > MAM (0.14) > JJA (0.152) in the SH. it is DJF > JJA > MAM > SON. The largest declining-decreasing trends are in SON of the NH (-0.0064/10a) and in JJA of the SH (-0.0064/10a), observed in NH summer and SH winter. The increasing trends are in MAM of the NH and in SJF and SON of the SH.

5-Regional AOD. From 1980 to 2021, regions with The high aerosol loadings (AOD > 0.2) regions are were found in West Africa, Southeast and Northeast Asia, Eastern China, and India, with a trend of -0.0062/10a, 0.0007/10a, -0.0009/10a, 0.0133/10a, and 0.0119/10a, respectively. However, the trends are decreasing in Eastern China (-0.0572/10a) and Northeast Asia (-0.0213/10a) after 2014 and the lager increasing trend is found after 2005 in India (0.0446/10a). The -Regions with moderate aerosol loadings (AOD between 0.15 and 0.2) regions are Eastern Europe, Western Europe,

1200 Eastern North America, Central South America, ~~and South Africa, and Southeast Asia,~~ with a trend
1201 of ~~-0.0067/10a, -0.0026/10a, -0.0027/10a, -0.0062/10a, and -0.0016/10a, respectively.~~ The low
1202 aerosol loading (AOD < 0.15) regions are ~~Eastern Europe, Western Europe,~~ Western North America,
1203 and Australia, with a trend of ~~-0.0017/10a and -0.0028/10a.~~ However, the trends in Southern Africa,
1204 Southeast Asia and Northeast Asia are not significant. ~~are regions with low aerosol loadings (AOD~~
1205 ~~< 0.15). The trends are -0.0041/10a, -0.0021/10a, -0.0009/10a, -0.0021/10a, -0.0100/10a,~~
1206 ~~0.0008/10a, -0.0096/10a), -0.0081/10a, -0.0003/10a, -0.0000/10a, 0.0071/10a, and 0.0096/10a in~~
1207 ~~Eastern Europe, Western Europe, Western North America, Eastern North America, Central South~~
1208 ~~America, Western Africa, Southern Africa, Australia, Southeast Asia, Northeast Asia, Eastern China,~~
1209 ~~and India, respectively.~~

1211 Competing interests

1212 The contact author has declared that none of the authors has any competing interests.

1213 Acknowledgments

1214 This work is supported by the National Key Research & Development Program of China
1215 (2022YFF0801302) and the National Natural Science Foundation of China (41930970). The hourly
1216 visibility data are downloaded from <https://mesonet.agron.iastate.edu/ASOS>. The Aerosol Robotic
1217 Network (AERONET) 15-minute ~~aerosol optical depth (AOD_λ)~~-data are downloaded from ~~which~~
1218 ~~can be downloaded from~~ <https://aeronet.gsfc.nasa.gov>. The MODIS AOD data are downloaded from
1219 <https://ladsweb.modaps.eosdis.nasa.gov>.

1221 References

- 1222 Ackerman, A. S., Hobbs, P. V., and Toon, O. B.: A model for particle microphysics, turbulent mixing,
1223 and radiative transfer in the stratocumulus-topped marine boundary layer and comparisons with
1224 measurements, J. Atmos. Sci., 52, 1204-1236, [https://doi.org/10.1175/1520-0469\(1995\)052<1204:AMFPMT>2.0.CO;2](https://doi.org/10.1175/1520-0469(1995)052<1204:AMFPMT>2.0.CO;2), 1995.
- 1226 Albrecht, B. A.: Aerosols, cloud microphysics, and fractional cloudiness, Science, 245, 1227-1230,
1227 <https://doi.org/10.1126/science.245.4923.1227>, 1989.
- 1228 Anderson, T. L., Charlson, R. J., Bellouin, N., Boucher, O., Chin, M., Christopher, S. A., Haywood, J.,
1229 Kaufman, Y. J., Kinne, S., Ogren, J. A., Remer, L. A., Takemura, T., Tanre, D., Torres, O., Trepte, C. R.,
1230 Wielicki, B. A., Winker, D. M., and Yu, H. B.: An "A-Train" strategy for quantifying direct climate
1231 forcing by anthropogenic aerosols, B. Am. Meteorol. Soc., 86, 1795-+, <https://doi.org/10.1175/Bams-86-12-1795>, 2005.
- 1233 Andersson, S. M., Martinsson, B. G., Vernier, J.-P., Friberg, J., Brenninkmeijer, C. A., Hermann, M., Van
1234 Velthoven, P. F., and Zahn, A.: Significant radiative impact of volcanic aerosol in the lowermost
1235 stratosphere, Nat. Commun., 6, 7692, <https://doi.org/10.1038/ncomms8692>, 2015.
- 1236 Andrews, E., Sheridan, P. J., Ogren, J. A., Hageman, D., Jefferson, A., Wendell, J., Alástuey, A., Alados-

1237 Arboledas, L., Bergin, M., and Ealo, M.: Overview of the NOAA/ESRL federated aerosol network, B.
1238 Am. Meteorol. Soc., 100, 123-135, <https://doi.org/10.1175/BAMS-D-17-0175.1>, 2019.

1239 Bergstrom, R. W., Pilewskie, P., Russell, P. B., Redemann, J., Bond, T. C., Quinn, P. K., and Sierau, B.:
1240 Spectral absorption properties of atmospheric aerosols, Atmos. Chem. Phys., 7, 5937-5943,
1241 <https://doi.org/10.5194/acp-7-5937-2007>, 2007.

1242 Berk, R. A.: Classification and Regression Trees (CART), in: Statistical Learning from a Regression
1243 Perspective, Springer New York, New York, NY, 1-65, https://doi.org/10.1007/978-0-387-77501-2_3,
1244 2008.

1245 Bescond, A., Yon, J., Girasole, T., Jouen, C., Rozé, C., and Coppalle, A.: Numerical investigation of the
1246 possibility to determine the primary particle size of fractal aggregates by measuring light depolarization,
1247 J. Quant. Spectrosc. Ra., 126, 130-139, <https://doi.org/10.1016/j.jqsrt.2012.10.011>, 2013.

1248 Boers, R., van Weele, M., van Meijgaard, E., Savenije, M., Siebesma, A. P., Bosveld, F., and Stammes,
1249 P.: Observations and projections of visibility and aerosol optical thickness (1956-2100) in the
1250 Netherlands: impacts of time-varying aerosol composition and hygroscopicity, Environ. Res. Lett., 10,
1251 <https://doi.org/10.1088/1748-9326/10/1/015003>, 2015.

1252 Bokoye, A. I., Royer, A., O'Neil, N., Cliche, P., Fedosejevs, G., Teillet, P., and McArthur, L.:
1253 Characterization of atmospheric aerosols across Canada from a ground-based sunphotometer network:
1254 AEROCAN, Atmos. Ocean, 39, 429-456, <https://doi.org/10.1080/07055900.2001.9649687>, 2001.

1255 Bösenberg, J. and Matthias, V.: EARLINET: A European Aerosol Research Lidar Network to Establish
1256 an Aerosol Climatology, Max Planck Institut Fur Meteorologie, 2003.

1257 Bright, J. M. and Gueymard, C. A.: Climate-specific and global validation of MODIS Aqua and Terra
1258 aerosol optical depth at 452 AERONET stations, Sol. Energy, 183, 594-605,
1259 <https://doi.org/10.1016/j.solener.2019.03.043>, 2019.

1260 Browne, M. W.: Cross-validation methods, J. Math. Psychol., 44, 108-132,
1261 <https://doi.org/10.1006/jmps.1999.1279>, 2000.

1262 Calvo, A. I., Alves, C., Castro, A., Pont, V., Vicente, A. M., and Fraile, R.: Research on aerosol sources
1263 and chemical composition: Past, current and emerging issues, Atmos. Res., 120, 1-28,
1264 <https://doi.org/10.1016/j.atmosres.2012.09.021>, 2013.

1265 Chafe, Z. A., Brauer, M., Klimont, Z., Van Dingenen, R., Mehta, S., Rao, S., Riahi, K., Dentener, F., and
1266 Smith, K. R.: Household Cooking with Solid Fuels Contributes to Ambient PM_{2.5} Air Pollution and the
1267 Burden of Disease, Environ. Health Persp., 122, 1314-1320, <https://doi.org/10.1289/ehp.1206340>, 2014.

1268 Chazette, P., David, C., Lefrère, J., Godin, S., Pelon, J., and Mégie, G.: Comparative lidar study of the
1269 optical, geometrical, and dynamical properties of stratospheric post-volcanic aerosols, following the
1270 eruptions of El Chichon and Mount Pinatubo, J. Geophys. Res-Atmos., 100, 23195-23207,
1271 <https://doi.org/10.1029/95JD02268>, 1995.

1272 Che, H., Zhang, X., Chen, H., Damiri, B., Goloub, P., Li, Z., Zhang, X., Wei, Y., Zhou, H., Dong, F., Li,
1273 D., and Zhou, T.: Instrument calibration and aerosol optical depth validation of the China Aerosol Remote
1274 Sensing Network, J. Geophys. Res-Atmos., 114, <https://doi.org/10.1029/2008jd011030>, 2009.

1275 Che, H., Xia, X., Zhu, J., Li, Z., Dubovik, O., Holben, B., Goloub, P., Chen, H., Estelles, V., Cuevas-
1276 Agullo, E., Blarel, L., Wang, H., Zhao, H., Zhang, X., Wang, Y., Sun, J., Tao, R., Zhang, X., and Shi, G.:
1277 Column aerosol optical properties and aerosol radiative forcing during a serious haze-fog month over
1278 North China Plain in 2013 based on ground-based sunphotometer measurements, Atmos. Chem. Phys.,
1279 14, 2125-2138, <https://doi.org/10.5194/acp-14-2125-2014>, 2014.

1280 Chen, A., Zhao, C., and Fan, T.: Spatio-temporal distribution of aerosol direct radiative forcing over mid-

1281 latitude regions in north hemisphere estimated from satellite observations, *Atmos. Res.*, 266, 105938,
1282 <https://doi.org/10.1016/j.atmosres.2021.105938>, 2022.

1283 Chen, D., Ou, T., Gong, L., Xu, C.-Y., Li, W., Ho, C.-H., and Qian, W.: Spatial Interpolation of Daily
1284 Precipitation in China: 1951-2005, *Adv. Atmos. Sci.*, 27, 1221-1232, [https://doi.org/10.1007/s00376-](https://doi.org/10.1007/s00376-010-9151-y)
1285 [010-9151-y](https://doi.org/10.1007/s00376-010-9151-y), 2010.

1286 Cherian, R. and Quaas, J.: Trends in AOD, clouds, and cloud radiative effects in satellite data and CMIP5
1287 and CMIP6 model simulations over aerosol source regions, *Geophys. Res. Lett.*, 47, e2020GL087132,
1288 <https://doi.org/10.1029/2020GL087132>, 2020.

1289 Chin, M., Diehl, T., Tan, Q., Prospero, J., Kahn, R., Remer, L., Yu, H., Sayer, A., Bian, H., and
1290 Geogdzhayev, I.: Multi-decadal aerosol variations from 1980 to 2009: a perspective from observations
1291 and a global model, *Atmos. Chem. Phys.*, 14, 3657-3690, <https://doi.org/10.5194/acp-14-3657-2014>,
1292 2014.

1293 Chu, D., Kaufman, Y., Ichoku, C., Remer, L., Tanré, D., and Holben, B.: Validation of MODIS aerosol
1294 optical depth retrieval over land, *Geophys. Res. Lett.*, 29, MOD2-1-MOD2-4,
1295 <https://doi.org/10.1029/2001GL013205>, 2002.

1296 Chuang, P.-J. and Huang, P.-Y.: B-VAE: a new dataset balancing approach using batched Variational
1297 AutoEncoders to enhance network intrusion detection, *J. Supercomput.*, [https://doi.org/10.1007/s11227-](https://doi.org/10.1007/s11227-023-05171-w)
1298 [023-05171-w](https://doi.org/10.1007/s11227-023-05171-w), 2023.

1299 Deuzé, J., Goloub, P., Herman, M., Marchand, A., Perry, G., Susana, S., and Tanré, D.: Estimate of the
1300 aerosol properties over the ocean with POLDER, *J. Geophys. Res.-Atmos.*, 105, 15329-15346,
1301 <https://doi.org/10.1029/2000JD900148>, 2000.

1302 Dhanya, R., Paul, I. R., Akula, S. S., Sivakumar, M., and Nair, J. J.: F-test feature selection in Stacking
1303 ensemble model for breast cancer prediction, *Procedia. Comput. Sci.*, 171, 1561-1570,
1304 <https://doi.org/10.1016/j.procs.2020.04.167>, 2020.

1305 Diner, D. J., Beckert, J. C., Reilly, T. H., Bruegge, C. J., Conel, J. E., Kahn, R. A., Martonchik, J. V.,
1306 Ackerman, T. P., Davies, R., and Gerstl, S. A. W.: Multi-angle Imaging SpectroRadiometer (MISR)
1307 instrument description and experiment overview, *Ieee T. Geosci. Remote.*, 98, 1072-1087,
1308 <https://doi.org/10.1109/36.700992>, 1998.

1309 Dong, Y., Li, J., Yan, X., Li, C., Jiang, Z., Xiong, C., Chang, L., Zhang, L., Ying, T., and Zhang, Z.:
1310 Retrieval of aerosol single scattering albedo using joint satellite and surface visibility measurements,
1311 *Remote Sens. Environ.*, 294, 113654, <https://doi.org/10.1016/j.rse.2023.113654>, 2023.

1312 Dubovik, Oleg, Holben, Brent, Eck, Thomas, F., Smirnov, Alexander, and Kaufman: Variability of
1313 Absorption and Optical Properties of Key Aerosol Types Observed in Worldwide Locations, *J. Atmos.*
1314 *Sci.*, 59, 590-590, [https://doi.org/10.1175/1520-0469\(2002\)059<0590:VOAAOP>2.0.CO;2](https://doi.org/10.1175/1520-0469(2002)059<0590:VOAAOP>2.0.CO;2), 2002a.

1315 Dubovik, O., Smirnov, A., Holben, B. N., King, M. D., Kaufman, Y. J., Eck, T. F., and Slutsker, I.:
1316 Accuracy assessments of aerosol optical properties retrieved from Aerosol Robotic Network (AERONET)
1317 Sun and sky radiance measurements, *J. Geophys. Res.-Atmos.*, 105, 9791-9806,
1318 <https://doi.org/10.1029/2000jd900040>, 2000.

1319 Dubovik, O., Holben, B., Eck, T. F., Smirnov, A., Kaufman, Y. J., King, M. D., Tanré, D., and Slutsker,
1320 I.: Variability of absorption and optical properties of key aerosol types observed in worldwide locations,
1321 *J. Atmos. Sci.*, 59, 590-608, [https://doi.org/10.1175/1520-0469\(2002\)059<0590:VOAAOP>2.0.CO;2](https://doi.org/10.1175/1520-0469(2002)059<0590:VOAAOP>2.0.CO;2),
1322 2002b.

1323 Eck, T. F., Holben, B. N., Reid, J. S., Sinyuk, A., Giles, D. M., Arola, A., Slutsker, I., Schafer, J. S.,
1324 Sorokin, M. G., and Smirnov, A.: The extreme forest fires in California/Oregon in 2020: Aerosol optical

1325 and physical properties and comparisons of aged versus fresh smoke, *Atmos. Environ.*, 305, 119798,
1326 <https://doi.org/10.1016/j.atmosenv.2023.119798>, 2023.

1327 Elterman, L.: Relationships between vertical attenuation and surface meteorological range, *Appl. Optics*,
1328 9, 1804-1810, <https://doi.org/10.1364/AO.9.001804>, 1970.

1329 Fan, H., Zhao, C., Yang, Y., and Yang, X.: Spatio-Temporal Variations of the
1330 $PM_{2.5}/PM_{10}$ Ratios and Its Application to Air Pollution Type Classification
1331 in China, *Front. Environ. Sci.*, 9, <https://doi.org/10.3389/fenvs.2021.692440>, 2021.

1332 Fernández, A., Garcia, S., Herrera, F., and Chawla, N. V.: SMOTE for learning from imbalanced data:
1333 progress and challenges, marking the 15-year anniversary, *J. Artif. Intell. Res.*, 61, 863-905,
1334 <https://doi.org/10.1613/jair.1.11192>, 2018.

1335 Forster, P., Ramaswamy, V., Artaxo, P., Berntsen, T., Betts, R., Fahey, D. W., Haywood, J., Lean, J., Lowe,
1336 D. C., and Myhre, G.: Changes in atmospheric constituents and in radiative forcing, *Climate Change*
1337 2007: The Physical Science Basis. Contribution of Working Group I to the 4th Assessment Report of the
1338 Intergovernmental Panel on Climate Change, 2007.

1339 Gelaro, R., McCarty, W., Suárez, M. J., Todling, R., Molod, A., Takacs, L., Randles, C. A., Darmenov,
1340 A., Bosilovich, M. G., Reichle, R., Wargan, K., Coy, L., Cullather, R., Draper, C., Akella, S., Buchard,
1341 V., Conaty, A., da Silva, A. M., Gu, W., Kim, G.-K., Koster, R., Lucchesi, R., Merkova, D., Nielsen, J.
1342 E., Partyka, G., Pawson, S., Putman, W., Rienecker, M., Schubert, S. D., Sienkiewicz, M., and Zhao, B.:
1343 The Modern-Era Retrospective Analysis for Research and Applications, Version 2 (MERRA-2), *J.*
1344 *Climate*, 30, 5419-5454, <https://doi.org/10.1175/JCLI-D-16-0758.1>, 2017.

1345 Giglio, L., Randerson, J. T., and Van Der Werf, G. R.: Analysis of daily, monthly, and annual burned area
1346 using the fourth-generation global fire emissions database (GFED4), *J. Geophys. Res-Biogeophys.*, 118, 317-
1347 328, <https://doi.org/10.1002/jgrg.20042>, 2013.

1348 Giles, D. M., Sinyuk, A., Sorokin, M. G., Schafer, J. S., Smirnov, A., Slutsker, I., Eck, T. F., Holben, B.
1349 N., Lewis, J. R., Campbell, J. R., Welton, E. J., Korkin, S. V., and Lyapustin, A. I.: Advancements in the
1350 Aerosol Robotic Network (AERONET) Version 3 database – automated near-real-time quality control
1351 algorithm with improved cloud screening for Sun photometer aerosol optical depth (AOD) measurements,
1352 *Atmos. Meas. Tech.*, 12, 169-209, <https://doi.org/10.5194/amt-12-169-2019>, 2019.

1353 Goovaerts, P.: Geostatistical approaches for incorporating elevation into the spatial interpolation of
1354 rainfall, *Journal of Hydrology*, 228, 113-129, [https://doi.org/10.1016/S0022-1694\(00\)00144-X](https://doi.org/10.1016/S0022-1694(00)00144-X), 2000.

1355 Gras, J., Jensen, J., Okada, K., Ikegami, M., Zaizen, Y., and Makino, Y.: Some optical properties of smoke
1356 aerosol in Indonesia and tropical Australia, *Geophys. Res. Lett.*, 26, 1393-1396,
1357 <https://doi.org/10.1029/1999GL900275>, 1999.

1358 Guerrero-Rascado, J. L., Landulfo, E., Antuña, J. C., Barbosa, H. d. M. J., Barja, B., Bastidas, Á. E.,
1359 Bedoya, A. E., da Costa, R. F., Estevan, R., and Forno, R.: Latin American Lidar Network (LALINET)
1360 for aerosol research: Diagnosis on network instrumentation, *J. Atmos. Sol-Terr. Phy.*, 138, 112-120,
1361 <https://doi.org/10.1016/j.jastp.2016.01.001>, 2016.

1362 Guo, J., Zhang, J., Yang, K., Liao, H., Zhang, S., Huang, K., Lv, Y., Shao, J., Yu, T., and Tong, B.:
1363 Investigation of near-global daytime boundary layer height using high-resolution radiosondes: first
1364 results and comparison with ERA5, MERRA-2, JRA-55, and NCEP-2 reanalyses, *Atmos. Chem. Phys.*,
1365 21, 17079-17097, <https://doi.org/10.5194/acp-21-17079-2021>, 2021.

1366 Hao, H., Wang, K., and Wu, G.: Visibility-derived aerosol optical depth over global land (1980-2021),
1367 National Tibetan Plateau Data Center [dataset], <https://doi.org/10.11888/Atmos.tpdc.300822>, 2023.

1368 He, H., Bai, Y., Garcia, E. A., and Li, S.: ADASYN: Adaptive synthetic sampling approach for

1369 imbalanced learning, IEEE World Congress on Computational Intelligence, 1322-1328,
1370 <https://doi.org/10.1109/IJCNN.2008.4633969>, 2008.

1371 Hersbach, H., Bell, B., Berrisford, P., Hirahara, S., Horányi, A., Muñoz-Sabater, J., Nicolas, J., Peubey,
1372 C., Radu, R., and Schepers, D.: The ERA5 global reanalysis, Q. J. Roy. Meteor. Soc., 146, 1999-2049,
1373 <https://doi.org/10.1002/qj.3803>, 2020.

1374 Hersey, S. P., Garland, R. M., Crosbie, E., Shingler, T., Sorooshian, A., Piketh, S., and Burger, R.: An
1375 overview of regional and local characteristics of aerosols in South Africa using satellite, ground, and
1376 modeling data, Atmos. Chem. Phys., 15, 4259-4278, <https://doi.org/10.5194/acp-15-4259-2015>, 2015.

1377 Hirono, M. and Shibata, T.: Enormous increase of stratospheric aerosols over Fukuoka due to volcanic
1378 eruption of El Chichon in 1982, Geophys. Res. Lett., 10, 152-154,
1379 <https://doi.org/10.1029/GL010i002p00152>, 1983.

1380 Hofmann, D., Barnes, J., O'Neill, M., Trudeau, M., and Neely, R.: Increase in background stratospheric
1381 aerosol observed with lidar at Mauna Loa Observatory and Boulder, Colorado, Geophys. Res. Lett., 36,
1382 <https://doi.org/10.1029/2009GL039008>, 2009.

1383 Holben, B. N., Eck, T. F., Slutsker, I., Tanre, D., Buis, J. P., Setzer, A., Vermote, E., Reagan, J. A.,
1384 Kaufman, Y. J., Nakajima, T., Lavenu, F., Jankowiak, I., and Smirnov, A.: AERONET - A federated
1385 instrument network and data archive for aerosol characterization, Remote Sens. Environ., 66, 1-16,
1386 [https://doi.org/10.1016/s0034-4257\(98\)00031-5](https://doi.org/10.1016/s0034-4257(98)00031-5), 1998.

1387 Hsu, N., Gautam, R., Sayer, A., Bettenhausen, C., Li, C., Jeong, M., Tsay, S.-C., and Holben, B.: Global
1388 and regional trends of aerosol optical depth over land and ocean using SeaWiFS measurements from
1389 1997 to 2010, Atmos. Chem. Phys., 12, 8037-8053, <https://doi.org/10.5194/acp-12-8037-2012>, 2012.

1390 Hsu, N., Jeong, M. J., Bettenhausen, C., Sayer, A., Hansell, R., Seftor, C., Huang, J., and Tsay, S. C.:
1391 Enhanced Deep Blue aerosol retrieval algorithm: The second generation, J. Geophys. Res.-Atmos., 118,
1392 9296-9315, <https://doi.org/10.1002/jgrd.50712>, 2013.

1393 Hsu, N., Lee, J., Sayer, A., Carletta, N., Chen, S. H., Tucker, C., Holben, B., and Tsay, S. C.: Retrieving
1394 near-global aerosol loading over land and ocean from AVHRR, J. Geophys. Res.-Atmos., 122, 9968-
1395 9989, <https://doi.org/10.1002/2017JD026932>, 2017.

1396 Hsu, N. C., Tsay, S.-C., King, M. D., and Herman, J. R.: Deep blue retrievals of Asian aerosol properties
1397 during ACE-Asia, Ieee T. Geosci. Remote., 44, 3180-3195, <https://doi.org/10.1109/tgrs.2006.879540>,
1398 2006.

1399 Hu, B., Zhang, X., Sun, R., and Zhu, X.: Retrieval of Horizontal Visibility Using MODIS Data: A Deep
1400 Learning Approach, Atmosphere-Basel, 10, <https://doi.org/10.3390/atmos10120740>, 2019.

1401 Hu, K., Kumar, K. R., Kang, N., Boiyo, R., and Wu, J.: Spatiotemporal characteristics of aerosols and
1402 their trends over mainland China with the recent Collection 6 MODIS and OMI satellite datasets, Environ.
1403 Sci. Pollut. R., 25, 6909-6927, <https://doi.org/10.1007/s11356-017-0715-6>, 2018.

1404 Husar, R. B., Husar, J. D., and Martin, L.: Distribution of continental surface aerosol extinction based on
1405 visual range data, Atmos. Environ., 34, 5067-5078, [https://doi.org/10.1016/s1352-2310\(00\)00324-1](https://doi.org/10.1016/s1352-2310(00)00324-1),
1406 2000.

1407 IPCC: Climate Change 2021: The Physical Science Basis, Cambridge University Press, New York, 2021.

1408 Ivanova, G., Ivanov, V., Kukavskaya, E., and Soja, A.: The frequency of forest fires in Scots pine stands
1409 of Tuva, Russia, Environ. Res. Lett., 5, 015002, <https://doi.org/10.1088/1748-9326/5/1/015002>, 2010.

1410 Kang, Y., Kim, M., Kang, E., Cho, D., and Im, J.: Improved retrievals of aerosol optical depth and fine
1411 mode fraction from GOCI geostationary satellite data using machine learning over East Asia, Isprs J.
1412 Photogramm., 183, 253-268, <https://doi.org/10.1016/j.isprsjprs.2021.11.016>, 2022.

1413 Kang, Y., Choi, H., Im, J., Park, S., Shin, M., Song, C.-K., and Kim, S.: Estimation of surface-level NO₂
1414 and O₃ concentrations using TROPOMI data and machine learning over East Asia, *Environ. Pollut.*, 288,
1415 117711, <https://doi.org/10.1016/j.envpol.2021.117711>, 2021.

1416 Karbowska, B. and Zembrzuski, W.: Fractionation and mobility of thallium in volcanic ashes after
1417 eruption of Eyjafjallajökull (2010) in Iceland, *B. Environ. Contam. Tox.*, 97, 37-43,
1418 <https://doi.org/10.1007/s00128-016-1831-6>, 2016.

1419 Kaufman, Y. J. and Boucher, O.: A satellite view of aerosols in the climate system, *Nature*, 419, 215-215,
1420 <https://doi.org/10.1038/nature01091>, 2002.

1421 Kim, D. H., Sohn, B. J., Nakajima, T., Takamura, T., Takemura, T., Choi, B. C., and Yoon, S. C.: Aerosol
1422 optical properties over east Asia determined from ground-based sky radiation measurements, *J. Geophys.*
1423 *Res-Atmos.*, 109, <https://doi.org/10.1029/2003jd003387>, 2004.

1424 Klett, J. D.: Lidar inversion with variable backscatter/extinction ratios, *Appl. Optics*, 24, 1638-1643,
1425 <https://doi.org/10.1364/AO.24.001638>, 1985.

1426 Koelemeijer, R., Homan, C., and Matthijsen, J.: Comparison of spatial and temporal variations of aerosol
1427 optical thickness and particulate matter over Europe, *Atmos. Environ.*, 40, 5304-5315,
1428 <https://doi.org/10.1016/j.atmosenv.2006.04.044>, 2006.

1429 Koschmieder, H.: Theorie der horizontalen Sichtweite, *Beitrage zur Physik der freien Atmosphäre*, 12,
1430 33-55, 1924.

1431 Krylov, A., McCarty, J. L., Potapov, P., Loboda, T., Tyukavina, A., Turubanova, S., and Hansen, M. C.:
1432 Remote sensing estimates of stand-replacement fires in Russia, 2002–2011, *Environ. Res. Lett.*, 9,
1433 105007, <https://doi.org/10.1088/1748-9326/9/10/105007>, 2014.

1434 Kulmala, M., Vehkamäki, H., Petäjä, T., Dal Maso, M., Lauri, A., Kerminen, V. M., Birmili, W., and
1435 McMurry, P. H.: Formation and growth rates of ultrafine atmospheric particles: A review of observations,
1436 *J. Aerosol Sci.*, 35, 143-176, <https://doi.org/10.1016/j.jaerosci.2003.10.003>, 2004.

1437 Kumm, M., De Moel, H., Salvucci, G., Viviroli, D., Ward, P. J., and Varis, O.: Over the hills and further
1438 away from coast: global geospatial patterns of human and environment over the 20th–21st centuries,
1439 *Environ. Res. Lett.*, 11, 034010, <https://doi.org/10.1088/1748-9326/11/3/034010>, 2016.

1440 Lapen, D. R. and Hayhoe, H. N.: Spatial analysis of seasonal and annual temperature and precipitation
1441 normals in southern Ontario, Canada, *J. Great Lakes Res.*, 29, 529-544, [https://doi.org/10.1016/s0380-1330\(03\)70457-2](https://doi.org/10.1016/s0380-1330(03)70457-2), 2003.

1443 Lee, L. A., Reddington, C. L., and Carslaw, K. S.: On the relationship between aerosol model uncertainty
1444 and radiative forcing uncertainty, *P. Natl. A. Sci.*, 113, 5820-5827,
1445 <https://doi.org/10.1073/pnas.1507050113>, 2016.

1446 Levy, R., Remer, L., Kleidman, R., Mattoo, S., Ichoku, C., Kahn, R., and Eck, T.: Global evaluation of
1447 the Collection 5 MODIS dark-target aerosol products over land, *Atmos. Chem. Phys.*, 10, 10399-10420,
1448 <https://doi.org/10.5194/acp-10-10399-2010>, 2010.

1449 Levy, R. C., Remer, L. A., Mattoo, S., Vermote, E. F., and Kaufman, Y. J.: Second-generation operational
1450 algorithm: Retrieval of aerosol properties over land from inversion of Moderate Resolution Imaging
1451 Spectroradiometer spectral reflectance, *J. Geophys. Res-Atmos.*, 112,
1452 <https://doi.org/10.1029/2006JD007811>, 2007.

1453 Levy, R. C., Mattoo, S., Munchak, L. A., Remer, L. A., Sayer, A. M., Patadia, F., and Hsu, N. C.: The
1454 Collection 6 MODIS aerosol products over land and ocean, *Atmos. Meas. Tech.*, 6, 2989-3034,
1455 <https://doi.org/10.5194/amt-6-2989-2013>, 2013.

1456 Levy, R. C., Mattoo, S., Sawyer, V., Shi, Y., Colarco, P. R., Lyapustin, A. I., Wang, Y., and Remer, L. A.:

1457 Exploring systematic offsets between aerosol products from the two MODIS sensors, *Atmos. Meas. Tech.*,
1458 11, 4073-4092, <https://doi.org/10.5194/amt-11-4073-2018>, 2018.

1459 Li, J., Garshick, E., Hart, J. E., Li, L., Shi, L., Al-Hemoud, A., Huang, S., and Koutrakis, P.: Estimation
1460 of ambient PM_{2.5} in Iraq and Kuwait from 2001 to 2018 using machine learning and remote sensing,
1461 *Environ. Int.*, 151, <https://doi.org/10.1016/j.envint.2021.106445>, 2021.

1462 Li, J., Carlson, B. E., Yung, Y. L., Lv, D., Hansen, J., Penner, J. E., Liao, H., Ramaswamy, V., Kahn, R.
1463 A., Zhang, P., Dubovik, O., Ding, A., Lacis, A. A., Zhang, L., and Dong, Y.: Scattering and absorbing
1464 aerosols in the climate system, *Nat. Rev. Earth. Environ.*, 3, 363-379, <https://doi.org/10.1038/s43017-022-00296-7>, 2022.

1466 Li, S., Chen, L., Huang, G., Lin, J., Yan, Y., Ni, R., Huo, Y., Wang, J., Liu, M., and Weng, H.: Retrieval
1467 of surface PM_{2.5} mass concentrations over North China using visibility measurements and GEOS-Chem
1468 simulations, *Atmos. Environ.*, 222, 117121, <https://doi.org/10.1016/j.atmosenv.2019.117121>, 2020.

1469 Li, Z., Lau, W. M., Ramanathan, V., Wu, G., Ding, Y., Manoj, M., Liu, J., Qian, Y., Li, J., and Zhou, T.:
1470 Aerosol and monsoon climate interactions over Asia, *Rev. Geophys.*, 54, 866-929,
1471 <https://doi.org/10.1002/2015RG000500>, 2016.

1472 Liao, H., Chang, W., and Yang, Y.: Climatic Effects of Air Pollutants over China: A Review, *Adv. Atmos.*
1473 *Sci.*, 32, 115-139, <https://doi.org/10.1007/s00376-014-0013-x>, 2015.

1474 Lin, J. T., van Donkelaar, A., Xin, J. Y., Che, H. Z., and Wang, Y. S.: Clear-sky aerosol optical depth over
1475 East China estimated from visibility measurements and chemical transport modeling, *Atmos. Environ.*,
1476 95, 258-267, <https://doi.org/10.1016/j.atmosenv.2014.06.044>, 2014.

1477 Liu, B., Ma, X., Ma, Y., Li, H., Jin, S., Fan, R., and Gong, W.: The relationship between atmospheric
1478 boundary layer and temperature inversion layer and their aerosol capture capabilities, *Atmos. Res.*, 271,
1479 <https://doi.org/10.1016/j.atmosres.2022.106121>, 2022.

1480 Mahowald, N. M., Ballantine, J. A., Feddema, J., and Ramankutty, N.: Global trends in visibility:
1481 implications for dust sources, *Atmos. Chem. Phys.*, 7, 3309-3339, <https://doi.org/10.5194/acp-7-3309-2007>, 2007.

1483 McNeill, V. F.: Atmospheric Aerosols: Clouds, Chemistry, and Climate, in: *Annu. Rev. Chem. Biomol.*,
1484 edited by: Prausnitz, J. M., Annual Review of Chemical and Biomolecular Engineering, 427-444,
1485 <https://doi.org/10.1146/annurev-chembioeng-060816-101538>, 2017.

1486 Mehta, M., Singh, R., Singh, A., and Singh, N.: Recent global aerosol optical depth variations and
1487 trends—A comparative study using MODIS and MISR level 3 datasets, *Remote Sens. Environ.*, 181,
1488 137-150, <https://doi.org/10.1016/j.rse.2016.04.004>, 2016.

1489 Mitra, R., Bajpai, A., and Biswas, K.: ADASYN-assisted machine learning for phase prediction of high
1490 entropy carbides, *Comp. Mater. Sci.*, 223, <https://doi.org/10.1016/j.commatsci.2023.112142>, 2023.

1491 Mortier, A., Gliß, J., Schulz, M., Aas, W., Andrews, E., Bian, H., Chin, M., Ginoux, P., Hand, J., and
1492 Holben, B.: Evaluation of climate model aerosol trends with ground-based observations over the last 2
1493 decades—an AeroCom and CMIP6 analysis, *Atmos. Chem. Phys.*, 20, 13355-13378,
1494 <https://doi.org/10.5194/acp-20-13355-2020>, 2020.

1495 Mukkavilli, S., Prasad, A., Taylor, R., Huang, J., Mitchell, R., Troccoli, A., and Kay, M.: Assessment of
1496 atmospheric aerosols from two reanalysis products over Australia, *Atmos. Res.*, 215, 149-164,
1497 <https://doi.org/10.1016/j.atmosres.2018.08.026>, 2019.

1498 Nagaraja Rao, C., Stowe, L., and McClain, E.: Remote sensing of aerosols over the oceans using AVHRR
1499 data Theory, practice and applications, *Int. J. Remote Sens.*, 10, 743-749,
1500 <https://doi.org/10.1080/01431168908903915>, 1989.

1501 Nakajima, T., Campanelli, M., Che, H., Estellés, V., Irie, H., Kim, S.-W., Kim, J., Liu, D., Nishizawa, T.,
1502 and Pandithurai, G.: An overview of and issues with sky radiometer technology and SKYNET, *Atmos.*
1503 *Meas. Tech.*, 13, 4195-4218, <https://doi.org/10.5194/amt-13-4195-2020>, 2020.

1504 NOAA, DOD, FAA, and USN: Automated Surface Observing System (ASOS) User's Guide, 1998.

1505 O'Reilly, J. E., Maritorena, S., Mitchell, B. G., Siegel, D. A., Carder, K. L., Garver, S. A., Kahru, M., and
1506 McClain, C.: Ocean color chlorophyll algorithms for SeaWiFS, *J. Geophys. Res.*, 103, 24937-24953,
1507 <https://doi.org/10.1029/98jc02160>, 1998.

1508 Pebesma, E. J.: Multivariable geostatistics in S: the gstat package, *Comput. Geosci.*, 30, 683-691,
1509 <https://doi.org/10.1016/j.cageo.2004.03.012>, 2004.

1510 Qiu, J. and Lin, Y.: A parameterization model of aerosol optical depths in China, *Acta. Meteorol. Sin.*,
1511 59, 368-372, <https://doi.org/10.11676/qxxb2001.039>, 2001.

1512 Ramanathan, V., Crutzen, P. J., Kiehl, J., and Rosenfeld, D.: Aerosols, climate, and the hydrological cycle,
1513 *Science*, 294, 2119-2124, <https://doi.org/10.1126/science.1064034>, 2001.

1514 Remer, L. A., Kleidman, R. G., Levy, R. C., Kaufman, Y. J., Tanre, D., Mattoo, S., Martins, J. V., Ichoku,
1515 C., Koren, I., Yu, H., and Holben, B. N.: Global aerosol climatology from the MODIS satellite sensors,
1516 *J. Geophys. Res.-Atmos.*, 113, <https://doi.org/10.1029/2007jd009661>, 2008.

1517 Remer, L. A., Kaufman, Y. J., Tanre, D., Mattoo, S., Chu, D. A., Martins, J. V., Li, R. R., Ichoku, C.,
1518 Levy, R. C., Kleidman, R. G., Eck, T. F., Vermote, E., and Holben, B. N.: The MODIS aerosol algorithm,
1519 products, and validation, *J. Atmos. Sci.*, 62, 947-973, <https://doi.org/10.1175/jas3385.1>, 2005.

1520 Salomonson, V. V., Barnes, W. L., Maymon, P. W., Montgomery, H. E., and Ostrow, H.: MODIS:
1521 advanced facility instrument for studies of the Earth as a system, *Ieee T. Geosci. Remote.*, 27, 145-153,
1522 <https://doi.org/10.1109/36.20292>, 1987.

1523 Sawamura, P., Vernier, J. P., Barnes, J. E., Berkoff, T. A., Welton, E. J., Alados-Arboledas, L., Navas-
1524 Guzmán, F., Pappalardo, G., Mona, L., and Madonna, F.: Stratospheric AOD after the 2011 eruption of
1525 Nabro volcano measured by lidars over the Northern Hemisphere, *Environ. Res. Lett.*, 7, 34013-
1526 34021(34019), <https://doi.org/10.1088/1748-9326/7/3/034013>, 2012.

1527 Schutgens, N., Tsyro, S., Gryspeerdt, E., Goto, D., Weigum, N., Schulz, M., and Stier, P.: On the spatio-
1528 temporal representativeness of observations, *Atmos. Chem. Phys.*, 17, 9761-9780,
1529 <https://doi.org/10.5194/acp-17-9761-2017>, 2017.

1530 Singh, A., Mahata, K. S., Rupakheti, M., Junkermann, W., Panday, A. K., and Lawrence, M. G.: An
1531 overview of airborne measurement in Nepal—Part 1: Vertical profile of aerosol size, number, spectral
1532 absorption, and meteorology, *Atmos. Chem. Phys.*, 19, 245-258, [https://doi.org/10.5194/acp-19-245-](https://doi.org/10.5194/acp-19-245-2019)
1533 [2019](https://doi.org/10.5194/acp-19-245-2019), 2019.

1534 Smirnov, A., Holben, B., Slutsker, I., Giles, D., McClain, C., Eck, T., Sakerin, S., Macke, A., Croot, P.,
1535 and Zibordi, G.: Maritime aerosol network as a component of aerosol robotic network, *J. Geophys. Res.-*
1536 *Atmos.*, 114, <https://doi.org/10.1029/2008JD011257>, 2009.

1537 Streets, D. G., Yan, F., Chin, M., Diehl, T., Mahowald, N., Schultz, M., Wild, M., Wu, Y., and Yu, C.:
1538 Anthropogenic and natural contributions to regional trends in aerosol optical depth, 1980–2006, *J.*
1539 *Geophys. Res.-Atmos.*, 114, <https://doi.org/10.1029/2008JD011624>, 2009.

1540 Sun, E., Xu, X., Che, H., Tang, Z., Gui, K., An, L., Lu, C., and Shi, G.: Variation in MERRA-2 aerosol
1541 optical depth and absorption aerosol optical depth over China from 1980 to 2017, *J. Atmos. Sol-Terr.*
1542 *Phy.*, 186, 8-19, <https://doi.org/10.1016/j.jastp.2019.01.019>, 2019.

1543 Sun, Y. and Zhao, C.: Influence of Saharan dust on the large-scale meteorological environment for
1544 development of tropical cyclone over North Atlantic Ocean Basin, *J. Geophys. Res.-Atmos.*, 125,

1545 e2020JD033454, <https://doi.org/10.1029/2020JD033454>, 2020.

1546 Teixeira, A.: Classification and regression tree, *Rev. Mal. Respir.*, 21, 1174-1176,
1547 [https://doi.org/10.1016/S0761-8425\(04\)71596-X](https://doi.org/10.1016/S0761-8425(04)71596-X), 2004.

1548 Tian, X., Tang, C., Wu, X., Yang, J., Zhao, F., and Liu, D.: The global spatial-temporal distribution and
1549 EOF analysis of AOD based on MODIS data during 2003-2021, *Atmos. Environ.*, 302,
1550 <https://doi.org/10.1016/j.atmosenv.2023.119722>, 2023.

1551 Tupper, A., Oswalt, J. S., and Rosenfeld, D.: Satellite and radar analysis of the volcanic-cumulonimbi at
1552 Mount Pinatubo, Philippines, 1991, *J. Geophys. Res-Atmos.*, 110,
1553 <https://doi.org/10.1029/2004JD005499>, 2005.

1554 van der Veer, G., Voerkelius, S., Lorentz, G., Heiss, G., and Hoogewerff, J. A.: Spatial interpolation of
1555 the deuterium and oxygen-18 composition of global precipitation using temperature as ancillary variable,
1556 *Journal of Geochemical Exploration*, 101, 175-184, <https://doi.org/10.1016/j.gexplo.2008.06.008>, 2009.

1557 Vernier, J. P., Thomason, L. W., Pommereau, J. P., Bourassa, A., Pelon, J., Garnier, A., Hauchecorne, A.,
1558 Blanot, L., Trepte, C., and Degenstein, D.: Major influence of tropical volcanic eruptions on the
1559 stratospheric aerosol layer during the last decade, *Geophys. Res. Lett.*, 38,
1560 <https://doi.org/10.1029/2011GL047563>, 2011.

1561 Wang, K., Dickinson, R. E., and Liang, S.: Clear Sky Visibility Has Decreased over Land Globally from
1562 1973 to 2007, *Science*, 323, 1468-1470, <https://doi.org/10.1126/science.1167549>, 2009.

1563 Wang, K. C., Dickinson, R. E., Su, L., and Trenberth, K. E.: Contrasting trends of mass and optical
1564 properties of aerosols over the Northern Hemisphere from 1992 to 2011, *Atmos. Chem. Phys.*, 12, 9387-
1565 9398, <https://doi.org/10.5194/acp-12-9387-2012>, 2012.

1566 Wei, J., Li, Z., Peng, Y., and Sun, L.: MODIS Collection 6.1 aerosol optical depth products over land and
1567 ocean: validation and comparison, *Atmos. Environ.*, 201, 428-440,
1568 <https://doi.org/10.1016/j.atmosenv.2018.12.004>, 2019.

1569 Wei, J., Li, Z., Sun, L., Peng, Y., Liu, L., He, L., Qin, W., and Cribb, M.: MODIS Collection 6.1 3 km
1570 resolution aerosol optical depth product: Global evaluation and uncertainty analysis, *Atmos. Environ.*,
1571 240, 117768, <https://doi.org/10.1016/j.atmosenv.2020.117768>, 2020.

1572 Welton, E. J., Campbell, J. R., Berkoff, T. A., Spinhirne, J. D., and Starr, D. O.: The micro-pulse lidar
1573 network (MPLNET), *Frontiers in Optics*, <https://doi.org/10.1364/fio.2003.mk2>, 2002.

1574 Winker, D. M., Tackett, J. L., Getzewich, B. J., Liu, Z., Vaughan, M. A., and Rogers, R. R.: The global
1575 3-D distribution of tropospheric aerosols as characterized by CALIOP, *Atmos. Chem. Phys.*, 13, 3345-
1576 3361, <https://doi.org/10.5194/acp-13-3345-2013>, 2013.

1577 Winker, D. M., Vaughan, M. A., Omar, A., Hu, Y., Powell, K. A., Liu, Z., Hunt, W. H., and Young, S. A.:
1578 Overview of the CALIPSO Mission and CALIOP Data Processing Algorithms, *J. Atmos. Ocean. Tech.*,
1579 26, 2310-2323, <https://doi.org/10.1175/2009jtecha1281.1>, 2009.

1580 Wu, J., Luo, J., Zhang, L., Xia, L., Zhao, D., and Tang, J.: Improvement of aerosol optical depth retrieval
1581 using visibility data in China during the past 50years, *J. Geophys. Res-Atmos.*, 119, 13370-13387,
1582 <https://doi.org/10.1002/2014jd021550>, 2014.

1583 Xia, X., Che, H., Zhu, J., Chen, H., Cong, Z., Deng, X., Fan, X., Fu, Y., Goloub, P., and Jiang, H.: Ground-
1584 based remote sensing of aerosol climatology in China: Aerosol optical properties, direct radiative effect
1585 and its parameterization, *Atmos. Environ.*, 124, 243-251,
1586 <https://doi.org/10.1016/j.atmosenv.2015.05.071>, 2016.

1587 Yang, X., Zhao, C., Yang, Y., and Fan, H.: Long-term multi-source data analysis about the characteristics
1588 of aerosol optical properties and types over Australia, *Atmos. Chem. Phys.*, 21, 3803-3825,

1589 <https://doi.org/10.5194/acp-21-3803-2021>, 2021a.

1590 Yang, X., Zhao, C., Yang, Y., Yan, X., and Fan, H.: Statistical aerosol properties associated with fire
1591 events from 2002 to 2019 and a case analysis in 2019 over Australia, *Atmos. Chem. Phys.*, 21, 3833-
1592 3853, <https://doi.org/10.5194/acp-21-3833-2021>, 2021b.

1593 Yang, X., Wang, Y., Zhao, C., Fan, H., Yang, Y., Chi, Y., Shen, L., and Yan, X.: Health risk and disease
1594 burden attributable to long-term global fine-mode particles, *Chemosphere*, 287,
1595 <https://doi.org/10.1016/j.chemosphere.2021.132435>, 2022.

1596 Yang, Y., Ge, B., Chen, X., Yang, W., Wang, Z., Chen, H., Xu, D., Wang, J., Tan, Q., and Wang, Z.:
1597 Impact of water vapor content on visibility: Fog-haze conversion and its implications to pollution control,
1598 *Atmos. Res.*, 256, <https://doi.org/10.1016/j.atmosres.2021.105565>, 2021c.

1599 Yoon, J., Burrows, J., Vountas, M. v., von Hoyningen-Huene, W., Chang, D., Richter, A., and Hilboll, A.:
1600 Changes in atmospheric aerosol loading retrieved from space-based measurements during the past decade,
1601 *Atmos. Chem. Phys.*, 14, 6881-6902, <https://doi.org/10.5194/acp-14-6881-2014>, 2014.

1602 Yoon, J., Pozzer, A., Chang, D. Y., Lelieveld, J., Kim, J., Kim, M., Lee, Y., Koo, J.-H., Lee, J., and Moon,
1603 K.: Trend estimates of AERONET-observed and model-simulated AOTs between 1993 and 2013, *Atmos.*
1604 *Environ.*, 125, 33-47, <https://doi.org/10.1016/j.atmosenv.2015.10.058>, 2016.

1605 Zhang, S., Wu, J., Fan, W., Yang, Q., and Zhao, D.: Review of aerosol optical depth retrieval using
1606 visibility data, *Earth-Sci. Rev.*, 200, 102986, <https://doi.org/10.1016/j.earscirev.2019.102986>, 2020.

1607 Zhang, Z., Wu, W., Wei, J., Song, Y., Yan, X., Zhu, L., and Wang, Q.: Aerosol optical depth retrieval from
1608 visibility in China during 1973-2014, *Atmos. Environ.*, 171, 38-48,
1609 <https://doi.org/10.1016/j.atmosenv.2017.09.004>, 2017.

1610 Zhao, A. D., Stevenson, D. S., and Bollasina, M. A.: The role of anthropogenic aerosols in future
1611 precipitation extremes over the Asian Monsoon Region, *Clim. Dynam.*, 52, 6257-6278,
1612 <https://doi.org/10.1007/s00382-018-4514-7>, 2019.

1613